LA-14353-MS
Approved for public release;
distribution is unlimited.

Nonlinear System Identification for Damage Detection

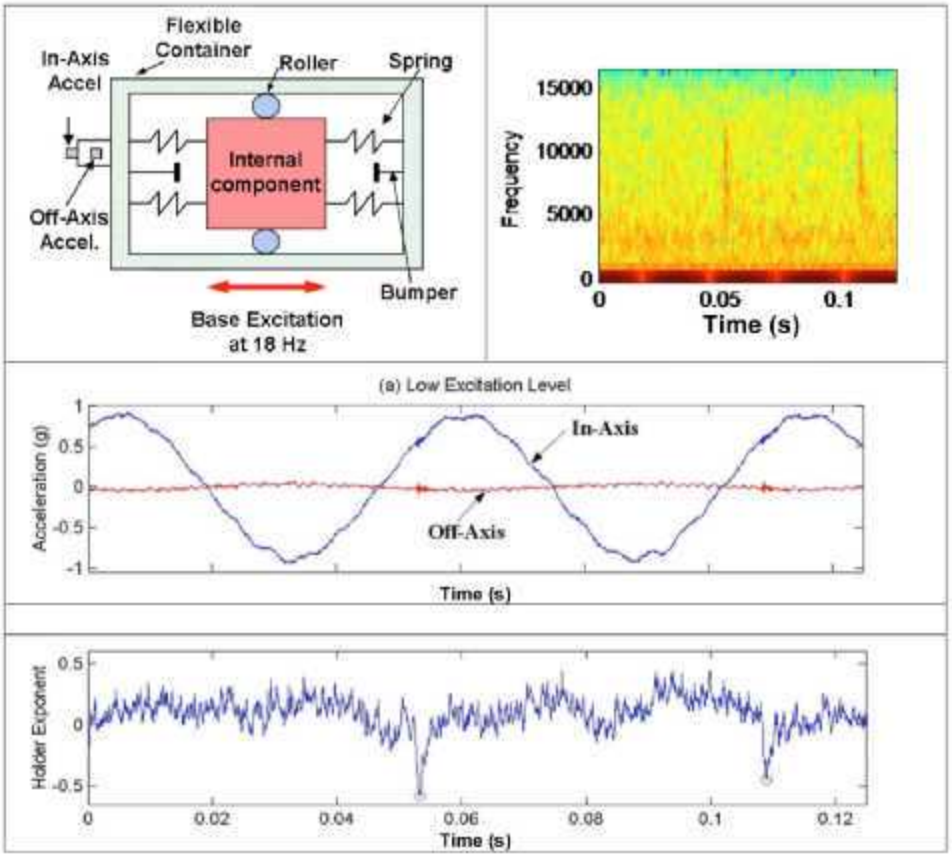

Los Alamos
NATIONAL LABORATORY
EST. 1943

About the cover: The figure in the upper left is an idealization of an actual test structure with loose internal parts that was subjected to an 18 Hz base input on a shake table. The figure in the upper right shows a time-frequency spectrum of the acceleration signal measured with the in-axis accelerometer. Vertical red contours occurring near 0.05 s and just after 0.1 s indicate the impacts associated with the rattling of internal components. The middle figure shows the acceleration-time histories measured with both the in-axis and off-axis accelerometers. Impacting of the internal components is evident in the off-axis accelerometer, but difficult to identify with the in-axis accelerometer. The bottom figure shows the time varying nature of the Holder exponent extracted from the in-axis accelerometer reading, which identifies the discontinuities in a signal associated with the impacting. This feature clearly identifies the impacting with the in-axis signal.

Los Alamos National Laboratory, an affirmative action/ equal opportunity employer, is operated by Los Alamos National Security, LLC, for the National Nuclear Security Administration of the U.S. Department of Energy under contract DE-AC52-06NA25396.

LA-14353-MS
Issued: November 2007

Nonlinear System Identification for Damage Detection

Charles R. Farrar
Keith Worden*
Michael D. Todd**
Gyuhae Park
Jonathon Nichols†
Douglas E. Adams††
Matthew T. Bement
Kevin Farinholt

* Department of Mechanical Engineering, University of Sheffield, Sheffield, UK
** Department of Structural Engineering, University of California, San Diego, La Jolla, CA 92093-0085
† Code 5673, Naval Research Laboratory, Washington, DC 20375
†† School of Mechanical Engineering, Purdue University, West Lafayette, IN 47907-2031

CONTENTS

LIST OF FIGURES

LIST OF TABLES

NONLINEAR SYSTEM IDENTIFICATION FOR DAMAGE DETECTION

Charles R. Farrar,[*] Keith Worden,[†] Michael D. Todd,[‡] Gyuhae Park,[1] Jonathonn Nichols,[§] Douglas Adams,[**] Matthew T. Bement,[1] and Kevin Farinholt[1]

ABSTRACT

This report has been developed based on information exchanges at a two-day workshop on nonlinear system identification for damage detection that was held July 25–26, 2006, at Los Alamos National Laboratory. The workshop is the second in a series that was hosted by the LANL/UCSD Engineering Institute (EI). This Institute is an education- and research-focused collaboration between Los Alamos National Laboratory (LANL) and the University of California, San Diego (UCSD), Jacobs School of Engineering. The Institute's research and education focus is to promote and further develop the multidisciplinary fields of structural health monitoring (SHM), damage prognosis and model validation and uncertainty quantification.

The process of implementing a damage detection strategy for aerospace, civil and mechanical engineering infrastructure is referred to as SHM. A statistical pattern recognition paradigm for SHM is first presented and the concept of nonlinear system identification is addressed with respect to the feature extraction portion of this paradigm. In many cases damage causes a structure that initially behaves in a predominantly linear manner to exhibit nonlinear response when subject to its operating environment. The formation of cracks that subsequently open and close under operating loads is an example of such damage. The damage detection process can be significantly enhanced if one takes advantage of these nonlinear effects when extracting damage-sensitive features from measured data. This report will provide examples from nonlinear dynamical systems theory and from nonlinear system identification techniques that are used for the feature extraction portion of the damage detection process. The report concludes by defining some future research needs and directions that are aimed at transitioning the concept of nonlinear system identification for damage detection from laboratory research to field-deployed engineering systems.

---

[*] The Engineering Institute, Los Alamos National Laboratory, Los Alamos, New Mexico 87545.

[†] Department of Mechanical Engineering, University of Sheffield, Sheffield, UK.

[‡] Department of Structural Engineering, University of California, San Diego, La Jolla, CA 92093-0085.

[§] Code 5673, Naval Research Laboratory, Washington, D. C. 20375.

[**] School of Mechanical Engineering, Purdue University, West Lafayette, IN 47907-2031.

1. INTRODUCTION

This report has been developed based on information exchanges at a two-day workshop on nonlinear system identification for damage detection that was held July 25–26, 2006, at Los Alamos National Laboratory. The workshop is the second in a series hosted by the LANL/UCSD Engineering Institute (EI). This Institute is an education- and research-focused collaboration between Los Alamos National Laboratory (LANL) and the University of California, San Diego (UCSD), Jacobs School of Engineering. The technical focus of this Institute is damage prognosis (DP), a multidisciplinary engineering science concerned with assessing the current condition and predicting the remaining life of aerospace, civil, and mechanical infrastructure. Structural Health Monitoring, which is the process of identifying damage in structures and tracking its evolution, is one of the technologies necessary to perform DP. Because DP relies on predictive models, model validation and uncertainty quantification is also a key technological component to the DP process.

1.1 The Structural Health Monitoring Process

Structural health monitoring (SHM) is the process of detecting damage in structures. The goal of SHM is to improve the safety and reliability of aerospace, civil, and mechanical infrastructure by detecting damage before it reaches a critical state. To achieve this goal, technology is being developed to replace qualitative visual inspection and time-based maintenance procedures with more quantifiable and automated damage assessment processes. These processes are implemented using both hardware and software with the intent of achieving more cost-effective condition-based maintenance. A more detailed general discussion of SHM can be found in [1].

The authors believe that all approaches to SHM, as well as all traditional nondestructive evaluation procedures (e.g., ultrasonic inspection, acoustic emissions, active thermography) can be cast in the context of a statistical pattern recognition problem [2]. Solutions to this problem require four steps: (1) Operational evaluation, (2) Data acquisition, (3) Feature extraction, and (4) Statistical modeling for feature classification.

A necessary first step to developing a SHM capability is Operational Evaluation. This part of the SHM solution process attempts to answer four questions regarding the implementation of a SHM system: (1) What are the life safety and/or economic justifications for monitoring the structure? (2) How is damage defined for the system being monitored? (3) What are the operational and environmental conditions under which the system of interest functions? (4) What are the limitations on acquiring data in the operational environment? Operational evaluation defines, and to the greatest extent possible, quantifies the damage that is to be detected. It also defines the benefits to be gained from deployment of the SHM system. This process also begins to set limitations on what will be monitored and how to perform the monitoring as well as tailoring the monitoring to unique aspects of the system and unique features of the damage that is to be detected.

The data acquisition portion of the SHM process involves selecting the excitation methods; the sensor types, numbers, and locations; and the data acquisition/storage/processing/transmittal hardware. The actual implementation of this portion of the SHM process will be application- specific. A fundamental premise regarding data acquisition and

sensing is that these systems do not measure damage. Rather, they measure the response of a system to its operational and environmental loading or the response to inputs from actuators embedded with the sensing system. Depending on the sensing technology deployed and the type of damage to be identified, the sensor readings may be more or less directly correlated to the presence and location of damage. Data interrogation procedures (feature extraction and statistical modeling for feature classification) are the necessary components of a SHM system that convert the sensor data into information about the structural condition. Furthermore, to achieve successful SHM, the data acquisition system will have to be developed in conjunction with these data interrogation procedures.

A damage-sensitive feature is some quantity extracted from the measured system response data that is correlated with the presence of damage in a structure. Ideally, a damage-sensitive feature will change in some consistent manner with increasing damage level. Identifying features that can accurately distinguish a damaged structure from an undamaged one is the focus of most SHM technical literature [3, 4]. Fundamentally, the feature extraction process is based on fitting some model, either physics-based or data-based, to the measured system response data. The parameters of these models or the predictive errors associated with these models then become the damage-sensitive features. An alternate approach is to identify features that directly compare the sensor waveforms or spectra of these waveforms measured before and after damage. Many of the features identified for impedance-based and wave propagation-based SHM studies fall into this category [5, 6, 7, 8].

The portion of the structural health monitoring process that has received the least attention in the technical literature is the development of statistical models to enhance the damage detection process. Statistical modeling for feature classification is concerned with the implementation of the algorithms that analyze the distributions of the extracted features in an effort to determine the damage state of the structure. The algorithms used in statistical model development usually fall into three general categories: (1) Group Classification, (2) Regression Analysis, and (3) Outlier Detection. The appropriate algorithm to use will depend on the ability to perform supervised or unsupervised learning. Here, supervised learning refers to the case where examples of data from damaged and undamaged structures are available. Unsupervised learning refers to the case where data are only available from the undamaged structure. The statistical models are typically used to answer a series of questions regarding the presence, location, type, and extent of damage.

Inherent in the data acquisition, feature extraction, and statistical modeling portions of the SHM process are data normalization, cleansing, fusion, and compression. As it applies to SHM, data normalization is the process of separating changes in sensor reading caused by damage from those caused by varying operational and environmental conditions [9]. Data cleansing is the process of selectively choosing data to pass on to, or reject from, the feature selection process. Data fusion is the process of combining information from multiple sensors in an effort to enhance the fidelity of the damage detection process. Data compression is the process of reducing the dimensionality of the data, or the feature extracted from the data, in an effort to facilitate efficient storage of information and to enhance the statistical quantification of these parameters. These four activities can be implemented in either hardware or software and usually a combination of the two approaches is used.

1.2 Annual Workshops

To further promote the development of DP, the EI is hosting a series of workshops that rotate their technical focus on an annual basis between (1.) Emerging sensing technologies; (2.) Data interrogation procedures; and (3.) Predictive modeling as these topics relate to DP. The results of the first workshop held in 2005, which focused on power harvesting for embedded structural health monitoring sensing systems, are summarized in a report that can be downloaded from www.lanl.gov/projects/ei [10]. Presentations, an attendee list, and the workshop agenda for this first workshop are also available at this Web address.

The 2006 workshop focus was on nonlinear system identification as it relates to the feature extraction portion for SHM. In many cases damage causes a structure that initially behaves in a predominantly linear manner to exhibit nonlinear response when subject to its operating environment. The formation of cracks that subsequently open and close under operating loads is an example of such damage. The damage detection process can be significantly enhanced if one takes advantage of these nonlinear effects when extracting damage-sensitive features from measured data. This report will summarize four discussion topics that were addressed in the workshop working groups. These topics are

- Sources/Classification of Material/Component/System and Damage Nonlinearities in SHM (See Section 3 Below)
- Nonlinearity versus Nonstationary Issues (See Section 5 below)
- Taxonomy and Usage of Nonlinear Approaches in SHM (Detection, Transition, Interrogation) (See Sections 6–8 below)
- Progress Barriers, Issues, and Outstanding SHM Requirements Demanding Nonlinear Methods (See Section 9 below)

In addition, the workshop attendees thought that terms associated with the theme topic should be defined and Section 4 provides these definitions. By addressing these topics this report is intended to summarize the state-of-the-art in nonlinear system identification as it has been applied to SHM and concludes with a summary of future research needs and challenges to transitioning this technology from research to field-deployed system applications. The summary will begin by first discussing commonly used damage-sensitive features and their limitations.

2. COMMONLY USED DAMAGE FEATURES AND THEIR LIMITATIONS

The most common features that have been reported in the SHM literature, and that represent a significant amount of data condensation from the actual measured quantities, are resonant frequencies, mode shape vectors, and quantities derived from these parameters. These features are identified by fitting a physics-based model, specifically a lumped-parameter modal model, to measured kinematic response time histories, most often absolute acceleration, or spectra of these time histories. Well-developed experimental modal analysis procedures are applied to the measured response time histories or spectra to estimate the system's modal properties [11,12]. The fitting process is done using data from

the structure in some initial and usually assumed undamaged condition, and then is repeated at periodic intervals or after some potentially damaging event that triggers the assessment process. Changes in the modal parameters are then used to indicate the presence and location of damage in either a forward or inverse manner [4].

Another class of damage identification methods is based on features related to changes in mass, stiffness and damping matrix indices associated with physical models that have been correlated so that the model predicts, as closely as possible, experimentally determined modal properties. These methods solve for the updated matrices (or perturbations to the nominal model that produce the updated matrices) by forming a constrained optimization problem based on the structural equations of motion, the nominal model, and the identified modal properties [13,14]. Comparisons of the matrix indices that have been correlated with modal properties identified from the damaged structure to the original correlated matrix indices can provide an indication of the existence, location and extent of damage.

The features described above have several issues associated with them that have prevented their use in most "real-world" applications. First, most of these features involve fitting a linear physics-based model to the measured data from both the healthy and potentially damaged structure. Often these models do not have the fidelity to accurately represent boundary conditions and structural component connectivity, which are prime locations for damage accumulation. Also, this process does not take advantage of changes in the system response that are caused by nonlinear effects. As a result, nonlinear effects tend to be smeared through the linear model-fitting process. From a more practical perspective, real-world structures' modal properties have been shown to be sensitive to changing environmental and operational conditions [15] and such sensitivity can lead to false indications of damage. Modal properties associated with lower-frequency global modes have been shown to be insensitive to local damage. In contrast at higher frequencies the modal properties are associated with local response. However, the practical limitations with the excitation and identification of the modal properties associated with these local modes, caused in part by high modal density and low participation factors, can make them difficult to identify. Finally, the inverse approaches to damage identification do not necessarily produce unique solutions and the degree of freedom mismatch between the numerical model and the measurement locations can severely limit the ability to accurately perform the required matrix updates. A more detailed discussion of these feature-extraction methods and their limitations can be found in [3, 4]. Based on these limitations and the observation that many damage scenarios cause a previously linear structure to exhibit nonlinear behavior, researchers have developed damage-sensitive features that take advantage of the nonlinear response exhibited by a damaged structure.

3. TYPES OF DAMAGE THAT CAN PRODUCE NONLINEAR SYSTEM RESPONSE

There are many types of damage that can cause an initially linear structural system to respond to its operational and environmental loads in a nonlinear manner. One of the most common types of damage is cracks that subsequently open and close under operational loading.

This type of damage may include fatigue cracks that form around rivets in air frames, cracks that occur in brittle materials such as concrete and cracks that result from excessive deformation such as those found in moment resisting steel frame connections after the Northridge earthquake. It is reiterated that nonlinear response to operational and environmental loading will only be observed in these cracked structures if the loading causes the cracks to open and close while data are being acquired. Otherwise the crack simply results in a change in geometry of the structure and the structure will continue to respond as a linear system, but in a different configuration. In some cases it is difficult to produce cracks in a controlled manner that exhibit the same dynamic characteristics as the cracks that occur in the in situ structure. Figure 1 shows a "crack" being introduced into a bridge structure to simulate fatigue cracks that occur at the welds of cross-beam seats to the web of the main load carrying plate girder [16]. However, this crack, which was introduced with a torch, produces a cut in the plate girder web that was approximately 10 mm wide. This crack did not open and close under any subsequent loading and, therefore, did not exhibit the same dynamic characteristics as the type of crack it was intended to simulate.

Figure 1. Torch cut that was used to simulate a fatigue crack in a plate girder.

Many of the common damage types observed in rotating machinery produce nonlinear responses to the harmonic excitation associated with the machine's operational frequency. There are numerous detailed charts of characteristic faults for a variety of machines and machine elements (e.g., see the chart on pp.515–522 in [17]; or the charts on pp. 88–92 in [18, Vol.1]). Damage to bearing races, loose bearing and chipped gear teeth are examples of damage that can produce nonlinear response in rotating machinery. Commercially available software specifically designed for the isolation of faults based on vibration signatures is readily available. For example, an automated, expert diagnostic system is evaluated in [19].

Another common type of damage that results in nonlinear system response is that of loose connections. This damage can include debond of glued connects or other types of chemical debond such as that between concrete and reinforcing steel, loose bolts, and interference fits that loosen because of material deformation. This type of damage overlaps with cracks as cracks in welded connections can result in a loose connection. The associated rattling or impacting that results when these loose connections are subject to sufficient loading causes structures with loose connections to exhibit nonlinear dynamic response characteristics. In some cases, such as the insertion of the femoral component of an artificial hip (shown in Fig. 2), engineers are attempting to utilize the transition from nonlinear response to linear response as an indicator of a successful implant in a cementless procedure that utilizes an interference fit.

Figure 2. The femoral component of an artificial hip being inserted into the femur of a cadaver with accelerometers monitoring the insertion process.

Another type of damage that can result in nonlinear dynamics response when these structures are subjected to dynamic loading, is delamination in bonded, layered materials such as fiber reinforced composite plates and shells. Often such delaminations are introduced by impact loading. Damage from this type of loading is difficult to detect because the delaminations often occur underneath the surface of the plate on the side opposite from the impact location and these locations may not be readily accessible for visual inspection. Delamination can be accompanied by matrix cracking and fiber breakage that add to the nonlinear dynamic response characteristics exhibited by the plate or shell if it is subsequently loaded to levels that cause the delamination to open and close. Figure 3 shows a composite plate that was subject to a projectile impact. Although some surface damage is visible on the side of the plate opposite from the impact, an ultrasonic scan reveals more extensive delaminations that can not be seen by surface inspection.

If one extends the concepts of structural health monitoring to manufacturing processes, then machine tool chatter is a phenomenon that can produce nonlinear dynamic response of the cutting tool. Chatter is the vibration that results during turning and facing operations. If not controlled, chatter can lead to poor surface finish and parts that will not

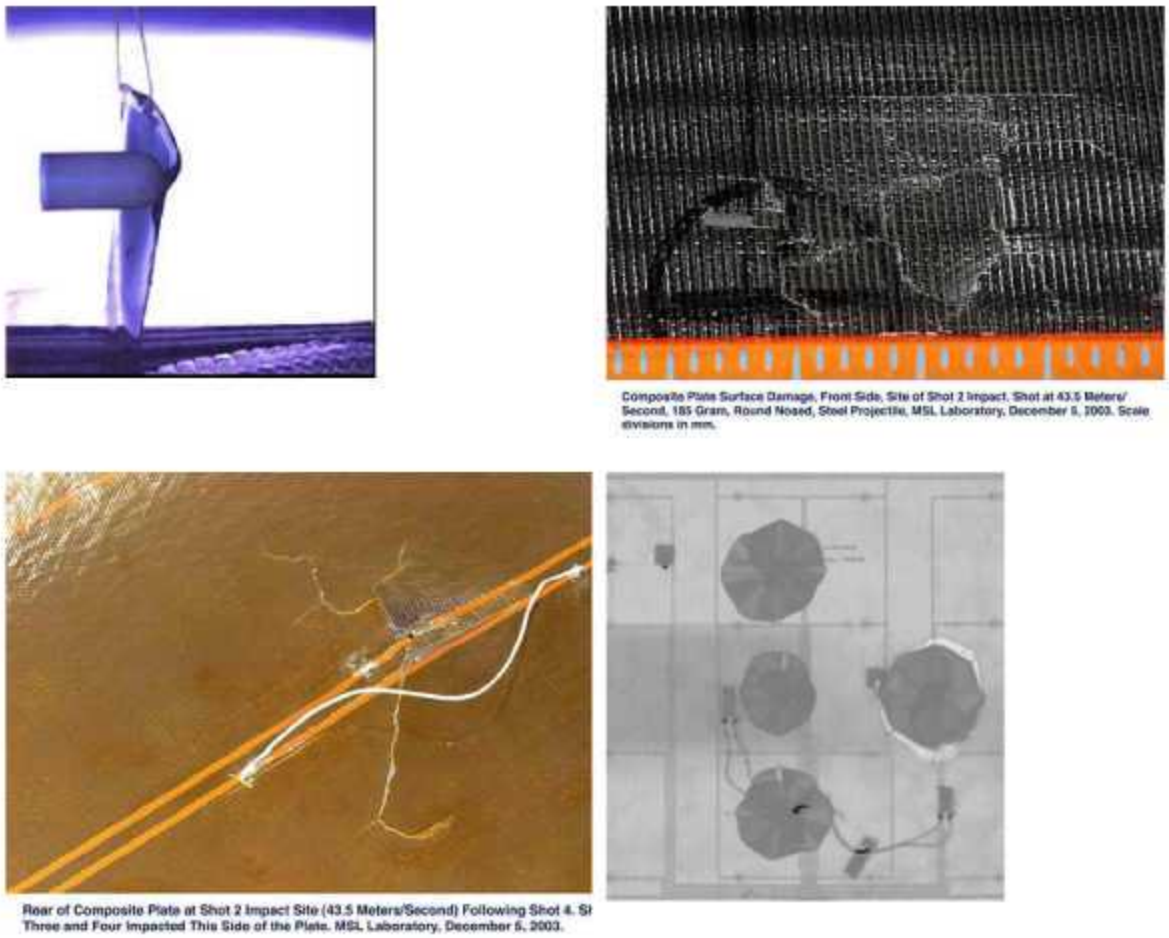

Figure 3. Upper left: high-speed projectile impacting the plate. Upper right: photo showing minimal surface damage where projectile impacted the plate. Lower left: more significant damage on the side opposite the impact. Lower right: ultrasonic scan showing more extensive delamination areas after four different impacts.

meet their design tolerances. Poor surface finish, in turn, can lead to the premature formation of fatigue cracks. The onset of chatter can potentially be detected by the nonlinear dynamic response characteristics measured on the cutting tool. Figure 4 shows a piezoelectric sensor that has been mounted on a cutting tool for the purpose of monitoring chatter during facing and turning operations.

Finally, material nonlinearities associated with excessive deformation such as yielding of steel can cause a structure to respond to dynamic loading in a nonlinear manner. This type of damage is particularly difficult to detect because in most cases yielding does not alter the stiffness or mass distribution of a structure once the loading has been removed. Yielding is accompanied by permanent deformation and in some cases this permanent deformation can lead to nonlinear system response if it results in subsequent impacting with neighboring components when the structure is dynamically loaded.

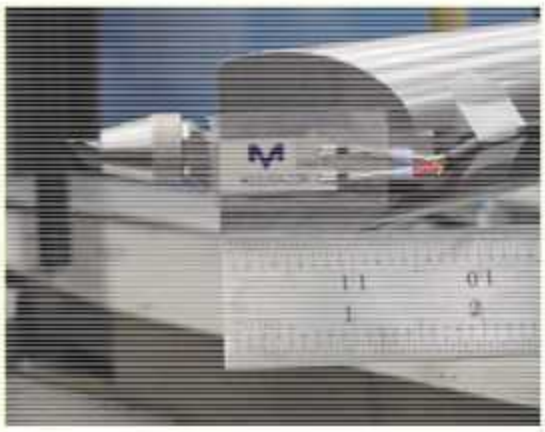

(a) Close-up of Cutting Tool and Sensor

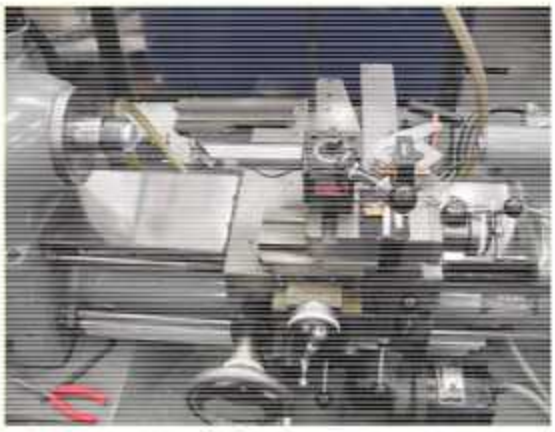

(b) Experimental Setup

Figure 4. Sensor mounted on a cutting tool to monitor chatter during facing and turning operations.

4. MOTIVATION FOR EXPLORING NONLINEAR SYSTEM IDENTIFICATION METHODS FOR SHM AND DEFINITION OF TERMS

Research aimed at defining damage-sensitive features based on the concepts of nonlinear system identification is motivated by an examination of the two simple single-degree-of-freedom (SDOF) systems shown in Figs. 5(a) and 5(b). Also shown in these figures are the force-displacement properties of their stiffness element. The response of the system on the left when subjected to a harmonic forcing function of amplitude F_0 at a frequency of ω can be described by the solution to the second-order linear differential equation

$$m\ddot{x} + c\dot{x} + kx = F_0 \cos \omega t \tag{1}$$

where m is the system mass, c is the viscous damping coefficient and k is the spring stiffness. Note that for this case m, c and k do not vary with either time or position of the mass.

The solution to this system is readily obtained in closed form for the given forcing function and, in principle, can be obtained for an arbitrary forcing function, $f(t)$, with a convolution integral.

$$x(t) = \int_{-\infty}^{+\infty} h(t-\tau) f(t) d\tau, \text{ where} \tag{2}$$

h is the system's impulse response function and for a SDOF system it is defined as

$$h(t) = \frac{1}{m\omega_d} e^{-\zeta\omega_n t} \sin(\omega_n t) \ , \tag{3}$$

$$where\ \omega_n = \sqrt{\frac{k}{m}},\ \zeta = \frac{c}{2\sqrt{mk}}\ and\ \omega_d = \omega_n\sqrt{\left(1-\zeta^2\right)}\ . \tag{4}$$

Solution by means of a convolution integral implies that the principle of superposition applies. Also, there is a unique input/output relationship defined in the frequency domain by the system's frequency response function (FRF), $H(\omega)$

$$X(\omega) = H(\omega)F(\omega)\ , \tag{5}$$

$$where\ H(\omega) = \frac{1}{-m\omega^2 + ic\omega + k}\ . \tag{6}$$

and $X(\omega)$ is the Fourier transform of the response and $F(\omega)$ is the Fourier transform of the input forcing function. The FRF is the Fourier transform of the impulse response function.

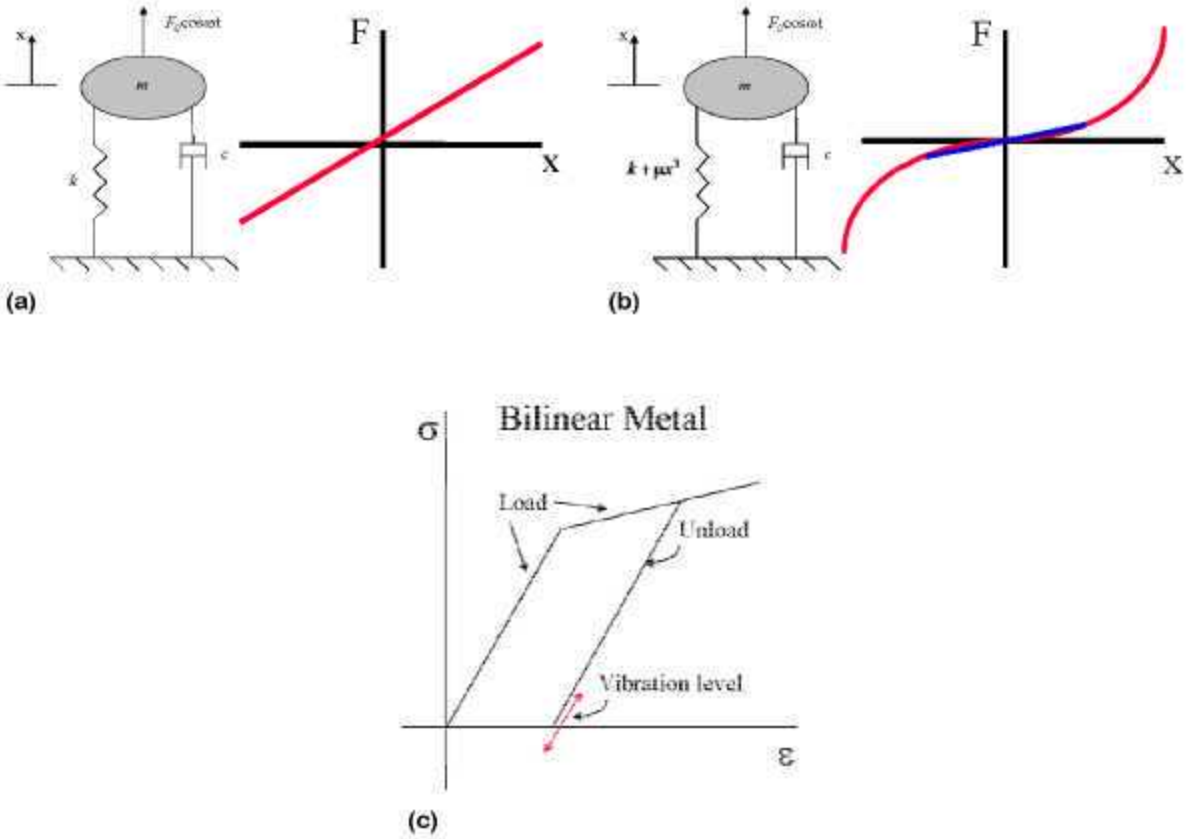

Figure 5. Characteristics of linear and nonlinear systems. (a) shows a spring-mass system with a linear stiffness element, (b) shows a spring-mass system with a cubic stiffness element, and (c) illustrates difficulties posed for low-level, vibration-based damage detection methods when monitoring yielding of metallic structures.

For systems made up of multiple interconnected SDOF systems, normal modes are defined and through proper coordinate transformation the response of the multi-degree of freedom (MDOF) system can be defined as the superposition of responses from a set of SDOF systems [20] The MDOF system will also have a unique frequency-domain system input–output relationship defined by the FRF matrix as

$$\{X(\omega)\} = [H(\omega)]\{F(\omega)\} \tag{7}$$

Also, the system will exhibit reciprocity meaning that if you excite at one location and measure the response at another location, that frequency response function will be the same as the one obtained by reversing that process A structure exhibiting reciprocity is characterized by symmetric stiffness and FRF matrices

The system in Fig 5(b) corresponds to a Duffing oscillator With this system the stiffness is not only a function of the mass's displacement, but also has a stiffness term that is proportional to the cube of this displacement and the equation of motion becomes

$$mx + cx + kx + \mu x^3 = F_0 \cos\omega t \tag{8}$$

This seemingly small perturbation to the system's stiffness element brings about some significant changes to the system dynamics First, a closed form solution is no longer available even for a harmonic input Superposition no longer applies and the frequency response function no longer defines a general unique input/output relation in the frequency domain Instead, the FRF is now a function of the system's input For MDOF systems normal modes are not defined, the system response can not be determined through modal superposition and reciprocity no longer applies

From this example, one can infer that when damage causes an initially linear system to respond in a nonlinear manner, the new dynamic response characteristics exhibited by the now nonlinear system can be used as distinct indicators of damage However, there are confounding factors that make identifying such changes a challenge First, many systems exhibit nonlinear response characteristics in their undamaged state In this case it is even more imperative that these characteristics are accurately quantified if changes in these nonlinear properties are to be used as indicators of damage Second, as shown in the force–displacement curve corresponding to the Duffing oscillator in Fig 5(b), if the excitation is small, the system will exhibit linear characteristics as indicated by the blue stiffness line Therefore, it may be difficult to identify the onset of nonlinear response characteristics without proper excitation A similar situation arises with metallic structures as shown in Fig 5(c) If damage is defined as yielding of the material, this damage can only be detected if measurements are made during the yielding process or if the measurements are sensitive to the permanent deformation in the material that results from the yielding process The strain hardening characteristics of such materials make it difficult to detect damage with low-level vibration-based techniques because such damage does significantly alter the mass, stiffness or energy dissipation properties when load has been removed from the material

A final challenge is the somewhat obvious statement that there is no single general method to model and identify all types of nonlinearities. Different nonlinearities have different characteristics as indicated by the two types of nonlinearities shown in Figs. 5(b) and 5(c), one of which has continuous load-displacement characteristics and the other that has a discontinuous load-deformation relationship. The implication is that one needs some knowledge of the nonlinearity type that the damage will produce in order to effectively identify the onset of that nonlinearity and the associated damage.

With this motivation the methods of the nonlinear system identification and modeling that have been applied to SHM are next reviewed. To facilitate this review, several terms related to these methods will first be defined followed by a more detailed discussion that compares and contrasts the topics of nonlinear system response versus nonstationary system response.

Deterministic dynamic system- A system that has no randomness. A deterministic system is one for which a mathematical expression can be defined that will describe its response at all times.

Linear dynamics system - A system that obeys the principle of superposition

Stochastic (random) dynamic system - A system where the future response can not be predicted from an explicit mathematical expression.

Ergodic process - A process where the statistics of the sample realizations of that process are equal to the statistics of the realization of the entire process implying a stationary process (defined below)

Casual system - A system where the current systems response and the system state is only a function of the current and past inputs to the system.

5. A DISCUSSION OF NONLINEAR SYSTEM RESPONSE VERSUS NON-STATIONARY SYSTEM RESPONSE

Most of the techniques that have been developed for the analysis of both linear and nonlinear systems pre-suppose that the acquired data are observations of a stationary random process. This assumption is useful to invoke because it can greatly simplify the estimation of quantities relevant to system identification. The difficulty, of course, is identifying when it is appropriate to treat the data as stationary. Additionally, the practitioner must also discern whether the data were produced by a linear or nonlinear system. Distinguishing among these categories (linear/nonlinear, stationary/nonstationary) is a challenging problem that does not admit a simple nonparametric (data driven) solution.

Before discussing some possible approaches, it is useful to define what is meant by a stationary random process. The definitions of linear and nonlinear processes have already been presented in an earlier section.

A strictly stationary random process is one in which the joint probability distribution of the measured data does not change in time. Let $x_k(n)$ be the k^{th} sample record (time series) of a random process X , measured at discrete times $t_n = 1,2,\ldots N$. Strict stationarity implies

$$p_x(x_k(t_1), x_k(t_2), \ldots, x_k(t_N)) = p_x(x_k(t_1 + \tau), x_k(t_2 + \tau), \ldots, x_k(t_N + \tau)) \quad (9)$$

where the function $p_x(\ )$ is the joint probability density function (pdf) associated with the N observations of the process. Equation 9 simply states that this function does not depend on time so long as the time differences between observations remain constant. The concept of ***weak stationarity*** is less demanding and requires that only the mean value and first joint moment of the data (as opposed to the entire pdf) remain unchanged by time shifting, i.e.

$$\begin{aligned} E\left[x_k(t_1)\right] &= E\left[x_k(t_1+\tau)\right] = \mu_x \\ E\left[x_k(t_1)x_k(t_2)\right] &= E\left[x_k(t_1+\tau)x_k(t_2+\tau)\right] = R_{xx}(t_2-t_1) \end{aligned} \tag{10}$$

Equation (10) states that the mean value does not depend on time while the autocovariance function for any two random variables, denoted R_{xx}, depends only on the relative time difference between the two observations. Continuing with higher and higher joint moments simply leads back to Eq. 9. The expected values associated with Eq. (10) are assumed to apply over the entire ensemble of k = 1…K records. However, in many cases the statistical properties may be estimated by averaging over time instead. The mean of the k^{th} record can be estimated as

$$\hat{\mu}_x(k) = \frac{1}{N}\sum_{n=1}^{N} x_k(t_n) \ . \tag{11}$$

If this quantity (as well as all other time-averaged properties) is expected to be the same for all sample functions k, the process is ergodic. From a practical standpoint the advantage to dealing with stationary, ergodic processes is that relevant statistics can be estimated with a single time record.

The above discussion concerns random processes only. For example, consider an ensemble of sine waves, $x_k(t)=A\sin(\omega t+\theta_k)$ where θ_k is a random phase associated with a particular realization of $x_k(t)$, and θ_k is uniformly distributed between 0 and 2π. At any time, t, the distribution, p(x(t)), of these sine waves is given by

$$p(x(t)) = \frac{1}{\pi\sqrt{A^2-x^2}} \ \ |x| < A,\ 0 \ \ otherwise \ . \tag{12}$$

Note, at each time, t, this distribution is not a function of time and, hence, the statistical moments will not be a function of time implying a stationary process. This time invariance of the distribution is shown in the left-hand side of Fig. 6.

However an ensemble of sine waves with no random phase will produce replicates of the same sine wave. The ensemble produced by this process is completely deterministic and is therefore non-stationary because at any time, t, the expected value is a function of t

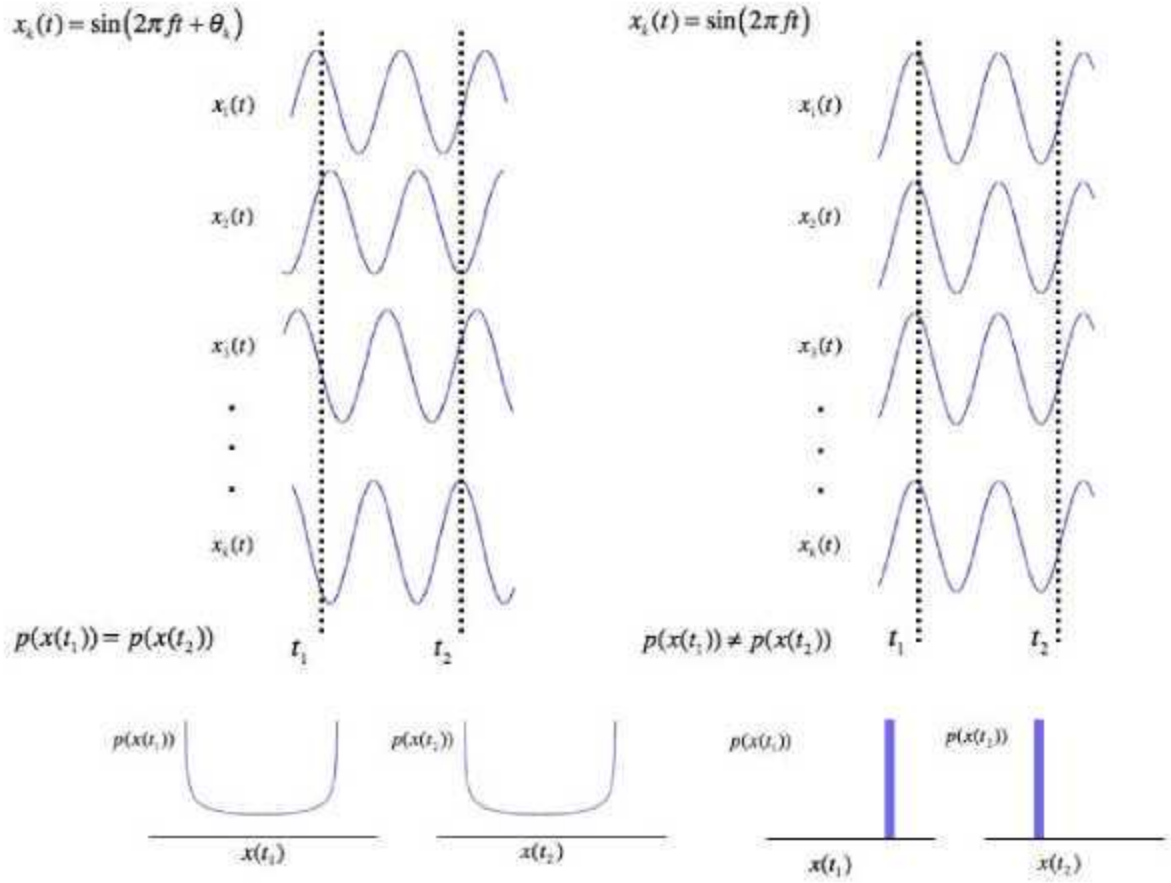

Figure 6. The left side shows realizations of a sine function with a random phase and the associated pdfs corresponding to times t_1 and t_2 illustrating that the pdfs are time invariant and implying the signal is stationary. The right side shows realizations of a sine wave without the random phase where the pdfs vary with time indicating the signal is nonstationary.

as shown in the right-hand side of Fig. 6. Stated another way, setting θ_k=0, the mean value of the ensemble at any time, t, is simply $E[x(t)] = A\sin(\omega t)$ and is therefore time dependent. The same fixed phase sine-wave with additive, zero-mean, Gaussian noise, $\eta(t)$, is also nonstationary as

$$E[x(t)] = A\sin(\omega t) + E[\eta(t)] = A\sin(\omega t) \ . \tag{13}$$

Some recently developed SHM techniques make use of a deterministic excitation however. For example, the theory underlying several attractor-based approaches to SHM suggest computing statistical "measures" from the data despite the fact that the data are non-stationary with respect to probability (there is no random component). How does one apply the definition of stationarity to deterministic systems?

In the study of deterministic dynamical systems the language changes but the concept of stationarity still remains. Assume we have a dynamical system governed by

$$x(t) = f_{\mu}^{t}(x(0))x \in \Re^{m} \tag{14}$$

where f is a deterministic function depending on time and parameters μ. If E is a subset of points in $\Re^{m}$, define the invariant measure $\rho(E)$ to satisfy [21].

$$\rho[f_{\mu}^{-t}(E)] = \rho[E] \tag{15}$$

That is to say, application of the dynamics forward or backward in time does not change the measure. This property is similar to our previous discussion of stationarity where time shifting did not alter the probability measure. It turns out that probability is just one subset of measure theory, describing the behavior of collections of points in space [22]. Both deterministic and random processes may be treated under this framework. As a working definition, we may therefore term a stationary process to be one in which the measure of interest (probability or other) associated with collections of observations is not changing in time.

The difficulty in distinguishing nonlinearity from nonstationarity can now be described. Many of the tests for nonlinearity are based on the null hypothesis that the underlying system is a linear, causal, time invariant system i.e. that the dynamics are described by

$$y(t) = \int_{-\infty}^{\infty} h(\tau)x(t-\tau)d\tau \ . \tag{16}$$

The alternative hypothesis is usually taken to be that the data were produced by a nonlinear, time invariant system. However, these tests will also reject the null hypothesis for non-stationary, linear processes. The nonstationarity may come as a result of the properties of the input changing in time (x(t) is non-stationary) or because the system parameters are changing in time i.e. $h(\tau) \rightarrow h(t,\tau)$. The latter situation is referred to as a linear time-varying system. In short, any test that is based on Eq. 16 as a null hypothesis may decide in favor of the alternative if the alternative is (1) a nonlinear process, (2) a linear process with non-stationary inputs, or (3) a time-varying linear process.

The method of surrogate data, for example, is one popular test for nonlinearity [23]. The practitioner creates randomized versions of the measured signal that preserve the autocorrelation function and probability distribution of the data. Under the null hypothesis of a linear, stationary response certain metrics computed from these randomized surrogates should be statistically indistinguishable from those computed from the original data.

Figure 7 shows the results of applying the method of surrogate data to several different types of system output. The discriminating feature used in this case was the mean nonlinear prediction error (NPE) obtained by using a nonlinear, data-driven model to forecast future values. The equations of motion for the system are given by

$$m\ddot{x} + c\dot{x} + (k + \varepsilon t^{2})x + k_{N}x^{2} = F(t) \tag{17}$$

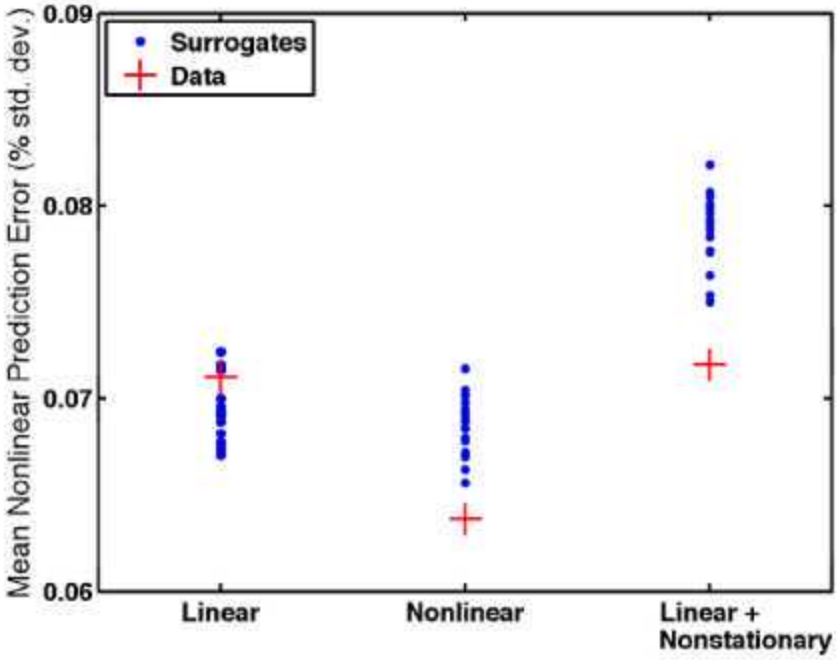

Figure 7. A surrogate test applied to the response of a single degree of freedom system driven with stationary Gaussian excitation. The discriminating feature used was the mean nonlinear prediction error (NPE). Blue dots represent the surrogate NPE values, red crosses represent the NPE values obtained from the original data.

where m = 1.0 kg, c = 3.0 N·s/m and k = 1000 N/m were fixed parameters and ε and k_N were the nonstationarity and nonlinearity parameters respectively. The excitation was taken as a stationary Gaussian random process with constant power spectral density $P_f = 0.01 N^2/Hz$. This system was numerically integrated, giving time series of N = 32768 observations sampled at intervals of 0.01s. For $\varepsilon = k_N = 0$, the system is linear and the data and surrogates produce mean NPE values in the same range. As expected, when $k_N = 10000\ N/m^2$, $\varepsilon = 0$ the system is nonlinear, stationary and the data fall outside the linear surrogate bound. However, when k = 100N/m, $\varepsilon = 0.025\ N/m \cdot s^2$, $k_N = 0\ N/m^2$, the system is linear with a time-varying stiffness and, hence, is non-stationary. Based on the surrogate analysis the response still appears nonlinear despite the fact that it was produced by a linear system.

Other tests for nonlinearity will similarly have difficulty in making the distinction. Tests based on the coherence function [24] require the estimation of the coherence between input and output data. This estimation, as is usually performed, involves the assumption of ergodicity (hence stationarity). This assumption is also why the surrogate algorithm has difficulty. The algorithm requires estimates of the power spectral density function, which depend on stationary data. Other tests for nonlinearity involve adjusting the input amplitude and observing the scaling in the response amplitude. For a linear system, the

response should scale with the input because of superposition (Eq. 16 again) while for a nonlinear system this will not be the case. However, any nonstationarity will also cause this test to fail unless the same nonstationarity is observed for each input amplitude (an unlikely event).

In short, it is difficult to make the distinction (nonlinear/nonstationary) using approaches based on Eq. 16. However, if the practitioner is willing to invoke a more detailed understanding of the system under test the two phenomena can possibly be separated. For example, if one has the three models of Eq. 17 (obtained by setting various combinations of parameters equal to zero) the question of which model is best supported by the data can be answered via a number of approaches. Even if only the time-scales of the underlying system are known *a priori*, a simple test for some types of nonstationarity is available. A reverse-arrangement "trend" test can be performed for both mean and variance (or any other moment). Divide the time history into "M" blocks and compute the sample mean, variance, etc. of each block giving D_i, i = 1…M. Summing up the total number of times $D_i > D_j$ (i = 1…N-1, j = i+1…N) gives a random variable A. If the M observations are independent, and of the same random variable, both the mean and variance of A are known and can be used to construct confidence intervals for this null hypothesis.

As an example, consider again the system of Eq. 17 with k = 100, $k_N = 0$, and varying levels of ε. The rate of increase is varied from $\varepsilon = 0 \ldots 0.0007$ N/m s^2 giving seven different "levels" of nonstationarity. The simulated time series were divided into M = 25 nonoverlapping blocks, each consisting of 1310 points (total time series length was 32768 observations). The expected value of the random variable A (obtained by averaging over 10 simulated responses), along with the associated 95% confidence intervals, is shown in Fig. 8 for both mean and variance of the data blocks. As expected, the parametric variation in stiffness does not influence the mean value, but does eventually result in a detectable trend (nonstationarity) in sample variance. The advantage to this test is that it is straightforward and non-parametric. The difficulty is in choosing the number of segments "M". This choice can only be made with some knowledge of the underlying time-scales of the process being observed. Additionally, this test will not capture an arbitrary type of nonstationarity.

In summary, nonlinearity and nonstationarity can be difficult to distinguish as both mechanisms will often cause rejections of the null hypothesis of a linear, time invariant system. While nonparametric tests for "trend" exist, they still require some knowledge of the system being observed. Nonlinearity and nonstationarity can only be definitively separated if well-defined models of both phenomena are available.

6. NONLINEAR INDICATOR FUNCTIONS

Nonlinear indicator functions are functions used to identify changes in the measured system response that are indicative of the onset of nonlinear system response. In some cases these indictors are based on the assumption that the undamaged system will exhibit linear response. Also, as previously mentioned changes in system response resulting from other system changes as well as operational and environmental variability may cause changes in these indicators.

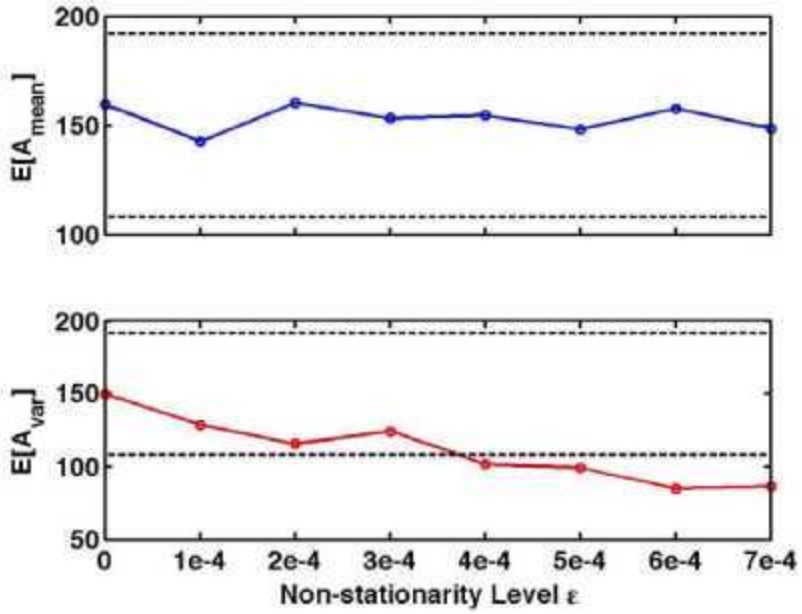

Figure 8. Trend tests applied to the system described by Eq. 17.

6.1 Basic Signal Statistics

Many basic signal statistics can be used as damaged-sensitive features. Examples of such statistics for an n-point discrete time series obtained from a sensor reading, x_i, are summarized in Table 1. Note that all of the features in Table 1 reduce the n-dimensional time series into a feature of unit dimension. For illustration purposes these statistics have been applied to acceleration-time histories recorded with Sensor 1 on a concrete column that was subjected to dynamic excitations with an electrodynamic shaker after various levels of damage had been introduced by quasi-static cyclic load tests as summarized in Appendix A. In the subsequent plots Damage Level 0 corresponds to the undamaged column. Damage Level 1 corresponds to a lateral displacement applied to the top of the column that caused incipient yield of the reinforcement and occurs after the concrete cracks. Damage Level 2 corresponds to a lateral displacement of the top of the column that is 2.5 times the lateral displacement that caused incipient yield. Damage Level 3 corresponds to a lateral displacement of the top of the column that is 7.0 times the lateral displacement that caused incipient yield.

The crest factor and K-factor listed in Table 1 are used to diagnose deviations from sinusoidal response. Data acquired from a 4 degree of freedom (DOF) model building subjected to sinusoidal base excitations are used to illustrate this feature. This structure and the testing procedures are summarized in Appendix B. All acceleration time histories from the concrete column and the 4 DOF system used to generate the plots below as well as detailed test summaries can be downloaded from www.lanl.gov/projects/ei.

Table 1. Signal Statistics that are Used as Damage Sensitive Features

Peak Amplitude (x_{peak})	$x_{peak} = \max\|x_i\|$
Mean (μ_x)	$\mu_x = \frac{1}{n}\sum_{i=1}^{n} x_i$
Mean Square (μsq)	$\mu_{sq} = \frac{1}{n}\sum_{i=1}^{n} (x_i)^2$
Root-Mean-Square (rms)	$rms = \sqrt{\frac{1}{n}\sum_{i=1}^{n} x_i^2}$
Standard Deviation (σ)	$\sigma = \sqrt{\frac{1}{n}\sum_{i=1}^{n} (x_i - \mu_x)^2}$
Skewness (dimensionless) (S_k)	$S_k = \frac{\frac{1}{n}\sum_{i=1}^{n} (X_i - \mu_x)^3}{\sigma^3}$
Kurtosis (dimensionless) (κ)	$\kappa = \frac{\frac{1}{n}\sum_{i=1}^{n} (X_i - \mu_x)^4}{\sigma^4}$
Crest Factor (X_{cf})	$X_{cf} = x_{peak}/rms$
K-Factor (X_k)	$X_k = x_{peak} * rms$

The first statistic discussed is the peak amplitude of the measured response. In cases where damage causes a reduction in stiffness and the input to the system is stationary, the peak amplitude of response will typically increase. This feature is plotted as a function of damage level for the concrete column tests in Fig. 9. The drop in peak amplitude associated with the final damage case is attributed to not maintaining the same input amplitude as the input was applied in an open-loop manner without feedback control.

There are many other basic statistics that can also be used to identify when changes in the system response that are indicative of damage have occurred as discussed below.

The mean and root-mean-square measure the central tendency of the data because these values typically fall in the central range of the time series amplitudes. To illustrate the shift in the mean value caused by damage, consider the cantilever beam shown in Fig. 10 (a). A through hole is drilled in the free end of the beam, and that end is connected to the Labworks ET-132 shaker with a 10-32 thread stinger. A strain gage was mounted 6 mm (1/4 in) from the aluminum clamp at the fixed end of the beam as shown in Fig. 10 (b). The beam was tested before and after it was plastically deformed. The plastic bending deformation was introduced

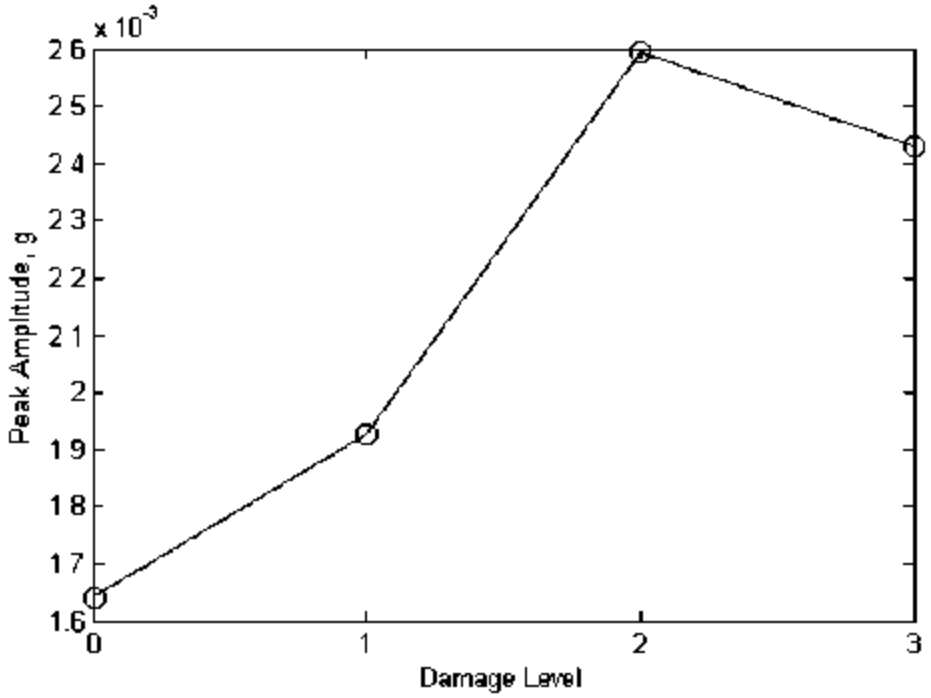

Figure 9. Peak amplitude of acceleration response measures at Sensor 1 (see Appendix A) on the concrete column tests plotted as a function of damage level.

near the strain gage, which resulted in 1253 με of static strain. Band-limited random noise with frequency content between 0.2 to 200 Hz was used as the dynamic excitation. Time and frequency domain data were captured for these random excitations. Figure 10 (c) shows the FRF that relates the conditioned strain-gage signal to the excitation voltage supplied to the shaker's amplifier. Each FRF is averaged from 10 separate measurements using a Hanning window. Figure 10 (c) illustrates that the deformation causes a shift in the resonant frequencies of the beam, increasing the first mode from 28 Hz to 30.5 Hz, and the second mode from 81 Hz to 84 Hz. The strain time histories from the random excitations are shown in Fig. 10 (d) where the DC offset in the strain readings is very clear as is evident in the distinct shift in the mean value of the signal, and this shift corresponds to the static plastic strain. This shift in the mean value will not be evident in an accelerometer reading because piezoelectric sensors do not measure DC response.

Note the mean value is sensitive to outliers, so a few extreme data points can significantly influence this feature. As illustrated in Fig. 10, a shift in the mean value is a feature that can detect the permanent offset caused by yielding as depicted in Fig. 6 so long as the sensor can respond to static loads (e.g., an electric resistance strain gage).

The mean-squared values and root-mean-square values are shown for the various concrete column damage levels in Fig. 11. Here one can see that these values increase with increased damage level. There is a significant increase between the incipient damage case and the subsequent damage case.

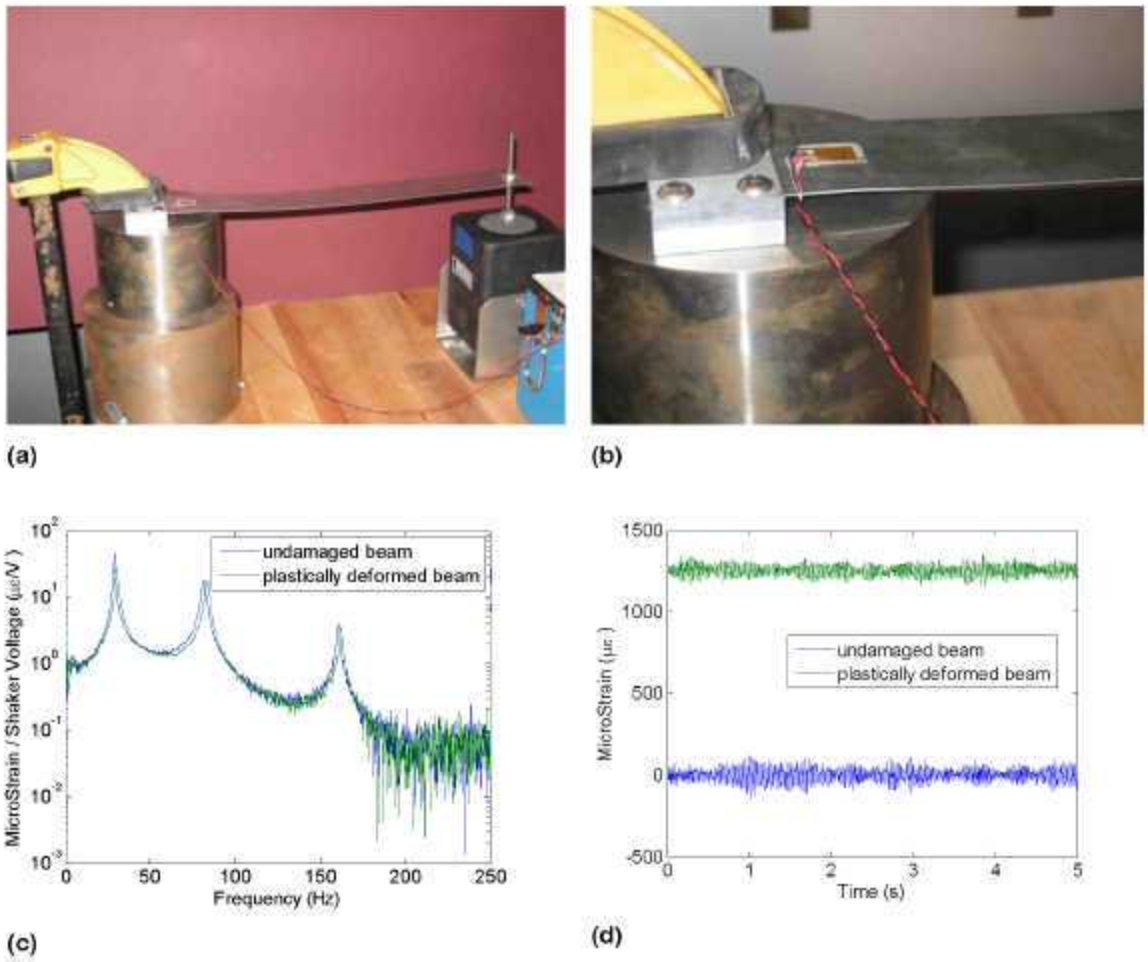

Figure 10. (a) Cantilever beam with shaker attached to the free end, (b) strain gage used to measure the beam's dynamic response, (c) frequency response functions from the undamaged and plastically deformed beam, and (d) strain-time histories from the undamaged and plastically deformed beam showing the offset in the mean values caused by the plastic deformation.

The standard deviation measures the dispersion about the mean of the time-series amplitudes. For a fixed level of excitation, damage that reduces the stiffness of the system will, in general, cause an increase in the standard deviation of the measured kinematic response quantities such as acceleration or strain. Figure 12 shows the change in the standard deviation of the acceleration response obtained from the concrete column tests as a function of increasing damage levels where the standard deviation is seen to increase with increasing damage levels. As with the other statistics, this series of tests shows that there is a significant increase in the standard deviation when the structure goes from the incipient damage level to the next higher damage level.

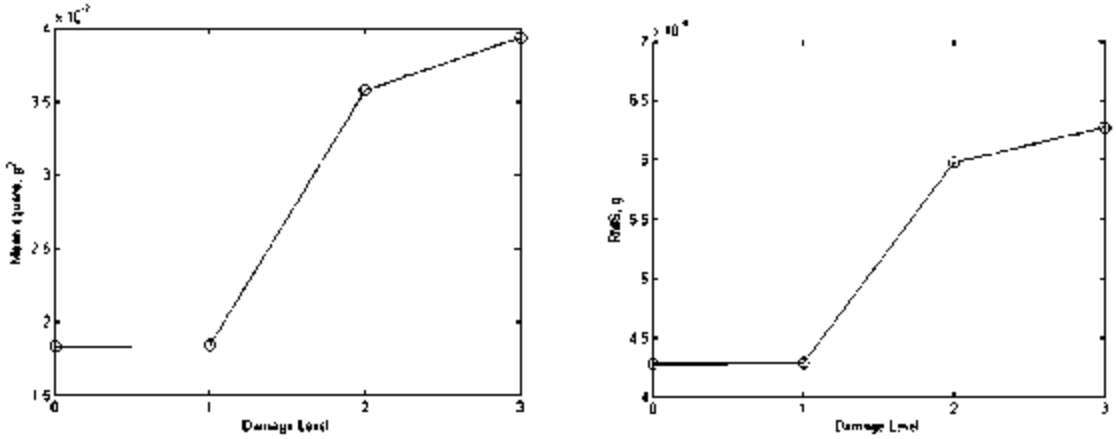

Figure 11. The mean squared values (left) and the root mean square values (right) for acceleration response measures at Sensor 1 (see Appendix A) on the concrete column tests plotted as a function of damage level.

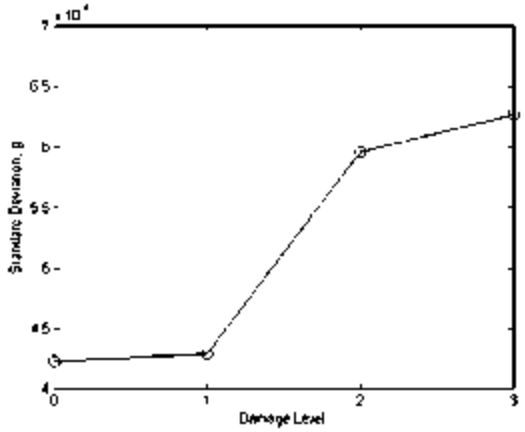

Figure 12. Standard deviation for acceleration response measured at Sensor 1 (see Appendix A) on the concrete column tests plotted as a function of damage level.

The skewness is another measure of the central tendency of a random variable. Any symmetric distribution such as normal distribution will have a skewness value equal to zero. The skewness is sensitive to an asymmetry being introduced into an initially symmetric system such as the interference that produces the nonlinear response in the 4 DOF system. Figure 13 shows the change in skewness for the 4 DOF system summarized in Appendix B when an impact nonlinearity is designed such that impacts occur when

relative deformations between the top two floors exceed a threshold value in one direction only. Therefore, this nonlinearity introduces an asymmetry into an originally symmetric structure. In Figure 13 the red lines correspond to a normal distribution fit to the measured acceleration amplitudes of the third floor (mass 4). The blue line corresponds to an approximation of the density function obtained with a kernel density estimator. When the system is linear, the kernel density estimate of the distribution function is nearly identical to the normal distribution that was fit to the data. In these cases the skewness value is close to zero as would be expected for a symmetric distribution. At the low excitation applied to the system with the nonlinearity, the estimated distribution function appears to overlay the normal distribution that was fit to the data, but the skewness value has increased by more than an order of magnitude. When the high the higher level excitation is applied to the nonlinear system the estimated density function shows significant difference from the normal distribution and the skewness value increased by more than two orders of magnitude compared to the comparable value obtained from the linear system.

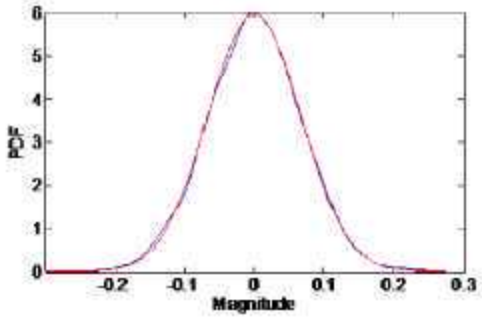

Linear System, Amplitude 0.5 v RMS

Skewness = -0.0020

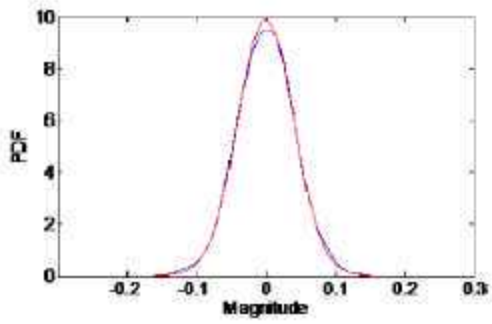

Impact Nonlinearity, Amplitude 0.5 v RMS

Skewness = - 0.0449

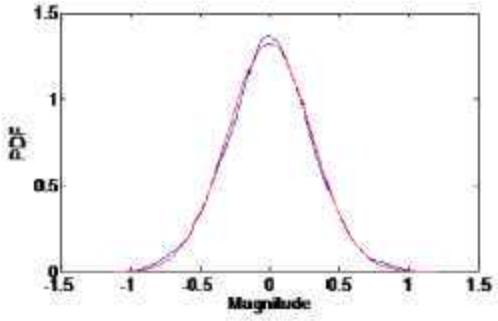

Linear System, Amplitude 2.0 v rms

Skewness = 0.0055

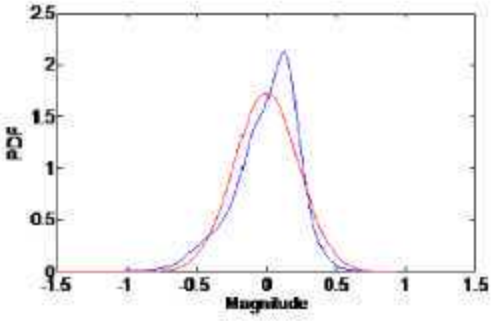

Impact Nonlinearity, Amplitude 2.0 v rms

Skewness = - 0.8850

Figure 13. The change in skewness between the linear and symmetric 4 DOF system (see Appendix B) and the same system when an asymmetric impact nonlinearity is present for two different levels of excitation.

The kurtosis measures the peaked nature of the measured-response distribution. This value is plotted for the various concrete column damage levels in Fig. 14. For a normally distributed response the kurtosis will have a value of 3.

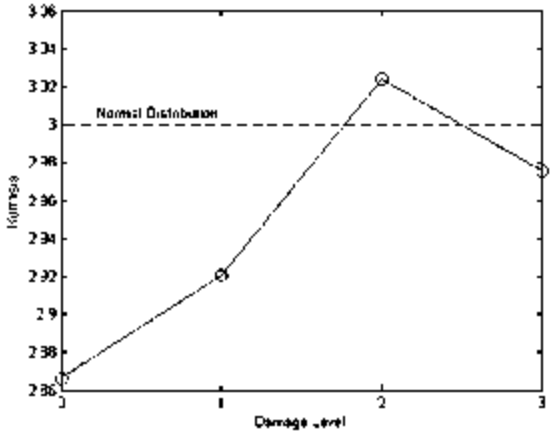

Figure 14. The kurtosis calculated for acceleration response measures at Sensor 1 (see Appendix A) on the concrete column tests plotted as a function of damage level.

The crest factor and K-factor are often used to assess the deviation from sinusoidal response in rotating machinery. For linear systems responding to a harmonic input this feature has a theoretical value of 1.414. Table 2 summarizes the crest and K-factors obtained from a force transducer at the base (mass 1) and accelerometers at each floor (masses 1–4) of the 4 DOF system summarized in Appendix B when the structure was subjected to 53 Hz and 70 Hz sinusoidal inputs at different amplitude levels. In Table 2 it can be seen that both the K-factor and the crest factor show a deviation from the expected values at the locations most influenced by the impacting. The crest factors obtained from sensor readings at the other locations show little change. The K-factor shows a significant change at all locations, but the changes are most pronounced at the locations closest to the impact location.

6.2 Coherence Function

The coherence function is a spectrum and is usually used with random or impulse excitation. It can provide a quick visual inspection of the quality of an FRF and, in many cases, is a rapid indicator of the presence of nonlinearity in specific frequency bands or resonance regions. It is arguably the most often-used test of nonlinearity, by virtue of the fact that almost all commercial spectrum analyzers come with software that calculates this quantity.

Table 2. Crest Factor and K-Factor for the 4 DOF System Subjected to Harmonic Inputs

	Crest Factor							
Sensor	**53 Hz Excitation**				70 Hz Excitation			
	No Bumper		**With Bumper**		**No Bumper**		**With Bumper**	
	Test 1	**Test 2**	**Test 1**	**Test 2**	**Test 1**	**Test 2**	**Test 1**	**Test 2**
Ch1	1.45	1.44	1.47	1.48	1.43	1.43	1.43	1.43
Ch2	1.42	1.42	1.42	1.42	1.44	1.44	1.41	1.41
Ch3	1.43	1.43	1.87	1.82	1.44	1.43	1.39	1.38
Ch4	1.42	1.42	1.03	1.02	1.43	1.42	1.32	1.32
Input	1.43	1.44	1.43	1.43	1.43	1.44	1.43	1.42
	K Factor							
Sensor	**53 Hz Excitation**				**70 Hz Excitation**			
	No Bumper		**With Bumper**		**No Bumper**		**With Bumper**	
	Test 1	Test 2	Test 1	Test 2	Test 1	Test 2	Test 1	Test 2
Ch1	2.68	2.82	0.00367	0.00369	0.824	0.737	0.270	0.267
Ch2	2.32	2.43	0.352	0.349	3.80	3.31	0.206	0.206
Ch3	2.12	2.23	0.0379	0.0354	2.96	2.55	0.0365	0.0373
Ch4	2.28	2.38	0.0627	0.0603	0.518	0.446	0.00729	0.00714
Input	821	792	2280	2270	1170	1210	1730	1720

Ch 1-4 are accelerometers mounted on each mass, Input is the force transducer mounted between the bottom mass and shaker.

Test 1 corresponds to a 0.5 v rms input amplitude. Test 2 corresponds to a 2.0 v rms input amplitude.

Bumper is located between mass 4 and mass 3 (Ch 4 and Ch 3)

Before discussing nonlinearity, the coherence function will be derived for linear systems subject to measurement noise on the output. Such systems have time-domain equations of motion,

$$x(t) = S[f(t)] + m(t) \tag{18}$$

where S is an operator that is a function of elastic, inertial and energy dissipation characteristics of the structure and m(t) is the measurement noise. In the frequency domain a little algebra produces the coherence function $\gamma^2(\omega)$ [24],

$$\gamma^2(\omega) = \frac{|H(\omega)|^2 S_{ff}(\omega)}{S_{xx}(\omega)} = 1 - \frac{S_{mm}(\omega)}{S_{xx}(\omega)} \tag{19}$$

where $H(\omega)$ is the frequency response function, $S_{ff}(\omega)$ is the power spectrum of the input, $S_{xx}(\omega)$ is the power spectrum of the response and $S_{nn}(\omega)$ is the power spectrum of the noise.

This quantity is the fraction of the output power, which can be linearly correlated with the input. Now, as $\gamma^2(\omega)$ and $S_{nn}(\omega)/S_{xx}(\omega)$ are both positive quantities, it follows that $0 \le \gamma^2 \le 1$ with $\gamma^2 = 1$ only if $S_{nn}(\omega)/S_{xx}(\omega) = 0$, implying that there is no measurement noise. The coherence function therefore detects if there is noise in the output measurement. In fact, it can be shown that $\gamma^2 < 1$ if there is noise anywhere in the measurement process [24]. If the coherence is plotted as a function of ω, any departures from unity will be readily identifiable. Note that all these quantities in the second term in Eq. 19 are readily computed by commercial spectrum analyzers designed to estimate $H(\omega)$, which is why coherence functions are so readily available in standard instrumentation.

Because the coherence function determines the extent of the output power linearly correlated with the input, it also detects nonlinearity. Consider the data from a SDOF system with a cubic stiffness; if the level of excitation is low, the response x will be small and x^3 will be negligible in comparison. In this regime, the system will effectively behave as a linear system and the coherence function for input and output will be near unity as shown in Figure 15 As the excitation is increased, the nonlinear terms will begin to play a part, and the coherence will drop as shown in Figure 16. This type of situation will occur for all polynomial nonlinearities and systems exhibiting piecewise-linear stiffness like those induced by a breathing crack [25]. However, if one considers Coulomb friction, the opposite occurs. At high excitation, the friction breaks out (that is, stick response gives way to slip response) and a nominally linear response will be obtained and hence coherence values closer to unity will result.

It is important to stress again that in order to use the coherence function for detecting nonlinearity and hence damage, it is necessary to realize that a reduction in the level of coherence can be caused by a range of problems, such as noise on the output and/or input signals that may in turn be caused by incorrect gain settings on amplifiers, leakage, and extraneous sources of unmeasured input to the system. Such obvious causes should be checked before structural nonlinearity and hence damage is suspected as the cause of loss of coherence.

6.3 Linearity and Reciprocity Checks

One method to demonstrate that a structure is responding in a nonlinear manner is to excite the structure at two different levels and show that that the response does not scale linearly by the ratio of the excitations levels. A common approach to visualize this property is to overlay the frequency response functions (FRFs) from the excitations at the two different levels. For linear systems the two FRFs obtained with the different excitation levels should overlay because the response spectrum is normalized by the input spectrum.

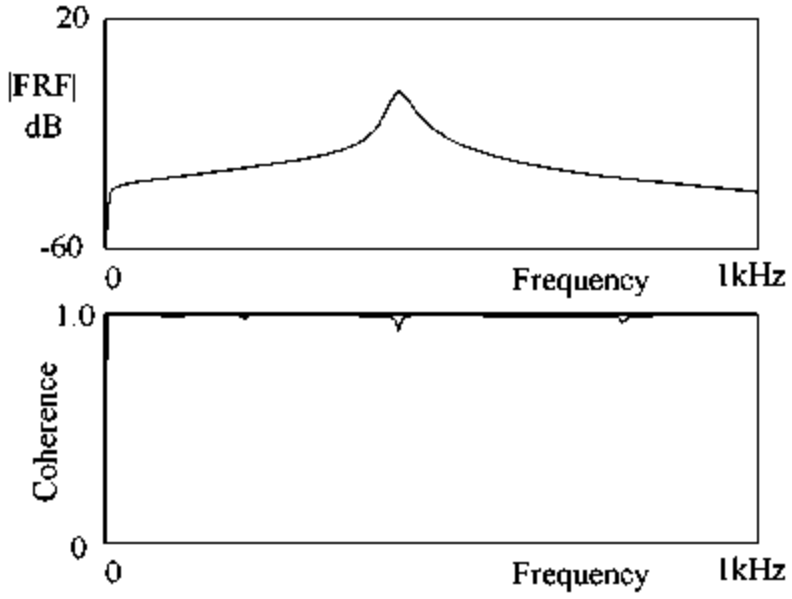

Figure 15. The coherence function for a cubic nonlinear oscillator under a low level of excitation.

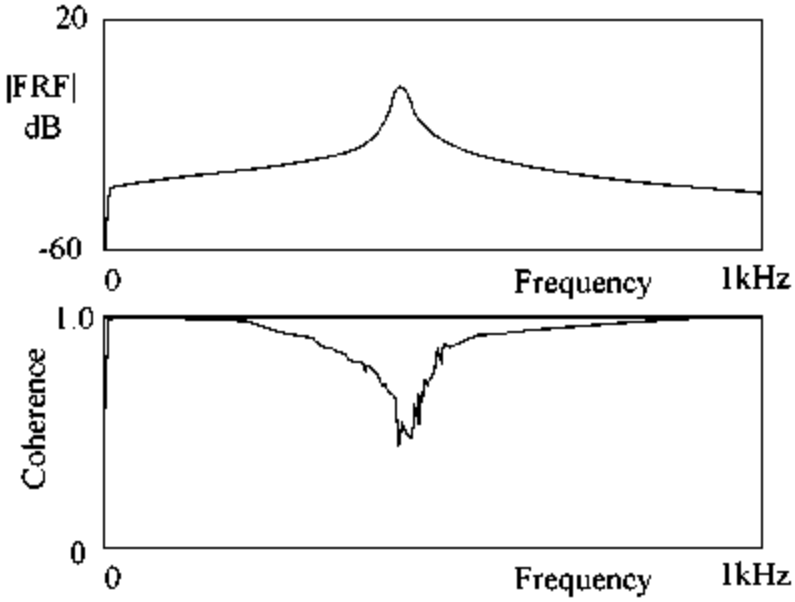

Figure 16. The coherence function for a cubic nonlinear oscillator under a high level of excitation.

Figure 17 shows an overlay of the input impulse power spectral density functions from a linearity check performed on a bridge structure summarized in [15] and the corresponding driving point FRFs. In this case the two impact tests where the power spectral density amplitudes were different by a factor of about five were performed within 2 hrs of each other and no changes were introduced to the structure's condition within this time period. Ideally, a linearity check should be performed over the expected range of operating loads, but this linearity test was limited to what could be obtained using the instrumented hammer. These plots highlight a difficulty with interpreting data from a linearity check. Between 7 and 25 Hz the structure exhibits linear characteristics when excited at the levels shown in this figure. However, above 30 Hz there is a noticeable difference in the two measurements suggesting the possibility that nonlinearities were excited in this frequency range or that signal-to-noise ratios were poor, thus providing the appearance of nonlinear response. This frequency range also corresponds to lower coherence in the lower-excitation level measurement as shown in Fig. 18. The coherence was observed to improve for the higher magnitude input suggesting that possibly the lower signal-to-noise ratio in the low-amplitude measurements might be causing the linearity test discrepancies shown in Fig. 17. Therefore, in addition to the FRF overlaying one would also like to see the corresponding coherence functions overlay as well to have confidence that the structure's response scales linearly with increasing amplitude.

Figures 19–22 show similar results for measurements made at each mass in the 4 DOF system (see Appendix B) when excited with different amplitude band-limited (20–200 Hz) random base inputs. These figures show the cases when the system is linear and when an impact nonlinearity is present between floors two and three (masses 3 and 4). These figures also show the corresponding coherence functions. For the linear case the FRF magnitudes overlay across the entire spectrum. With an exception for the drop in coherence associated with 60 Hz electric noise in the low amplitude tests, the coherence functions for the two linear systems also overlay.

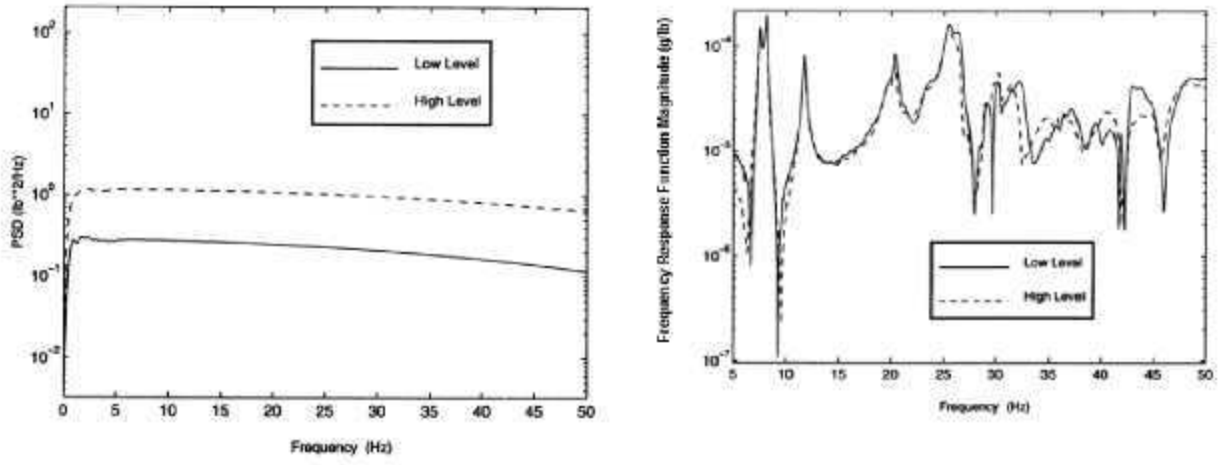

Figure 17. Results of a linearity check performed on bridge structure that shows different portions of the FRF are more sensitive to the nonlinear system response.

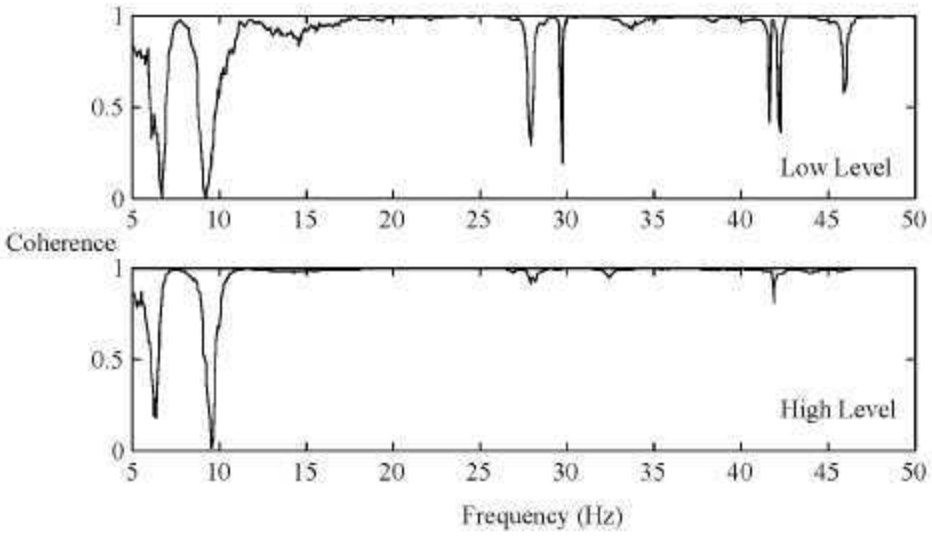

Figure 18. The coherence functions corresponding to the linearity tests shown in Fig. 17.

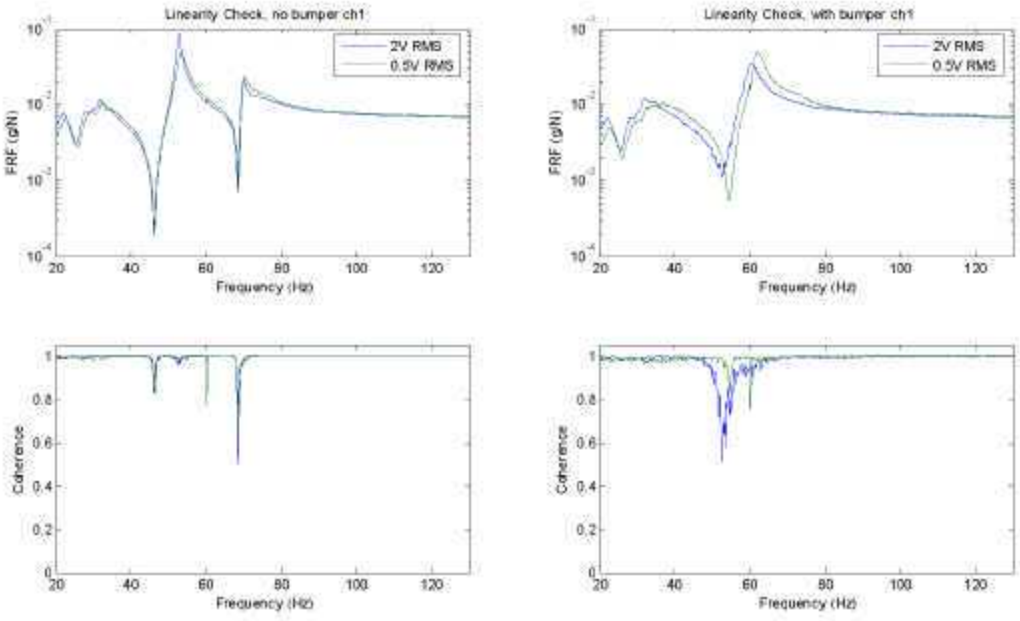

Figure 19. The linearity test FRF magnitudes and corresponding coherence functions for the base (mass 1) of the 4 DOF structure in a linear condition (left) and when an impact nonlinearity is present (right) between floors 2 and 3 (masses 3 and 4).

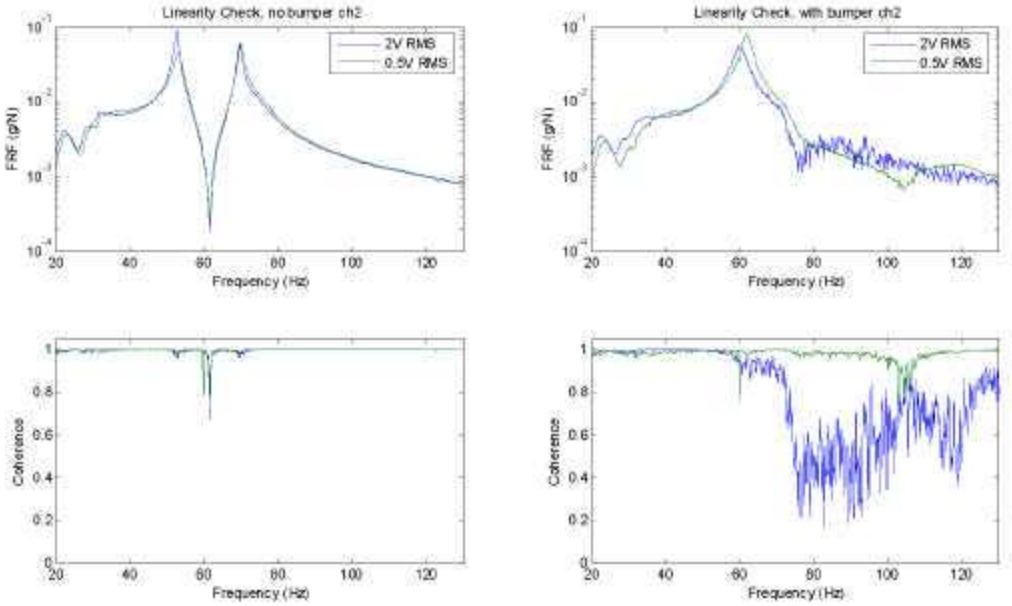

Figure 20. The linearity test FRF magnitudes and corresponding coherence functions for the first floor (mass 2) of the 4 DOF structure in a linear condition (left) and when an impact nonlinearity is present (right) between floors 2 and 3 (masses 3 and 4).

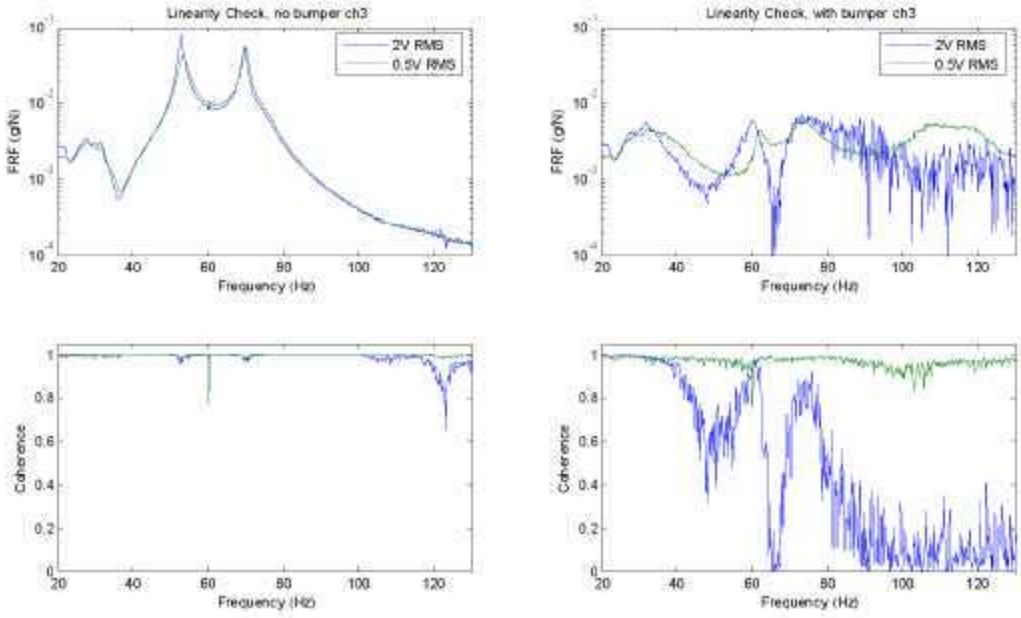

Figure 21. The linearity test FRF magnitudes and corresponding coherence functions for the second floor (mass 3) of the 4 DOF structure in a linear condition (left) and when an impact nonlinearity is present (right) between floors 2 and 3 (masses 3 and 4).

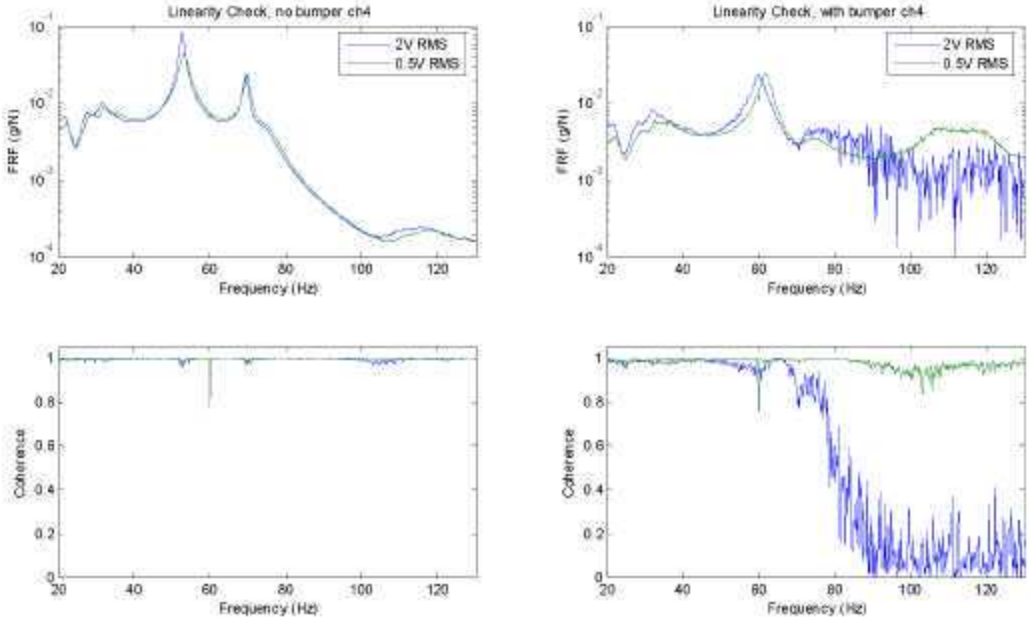

Figure 22. The linearity test FRF magnitudes and corresponding coherence functions for the third floor (mass 4) of the 4 DOF structure in a linear condition (left) and when an impact nonlinearity is present (right) between floors 2 and 3 (masses 3 and 4).

When the impact nonlinearity is present, there are significant distortions in the FRFs when compared to the corresponding linear cases. Also, there is considerable change in these FRFs and corresponding coherence functions associated with the impacting system as a function of excitation level, particularly in the higher frequency portions of the spectra.

Reciprocity checks are also performed to assess the linearity of a system's response. A structure is said to exhibit reciprocity when the measured FRF formed from an input at location j and a response at location i corresponds directly with the measured FRF formed from an input at location i and response at location j. Figure 23 shows the FRF magnitudes for an impact applied at one point on a bridge deck (see [15]) and a response measured at one of the most distant measurement points on that same deck. Also shown in this figure is the FRF magnitude for an impact applied at pt. B and a response measured at Point A. Coherence plots corresponding to the reciprocity results are also shown in Figure 23. Because the data acquisition system channels were moved from one point to another (i.e., the input measurement channel is the same for inputs at both locations as shown in Fig. 24), these figures show the reciprocity of the entire measurement system, including the structure and the data acquisition system.

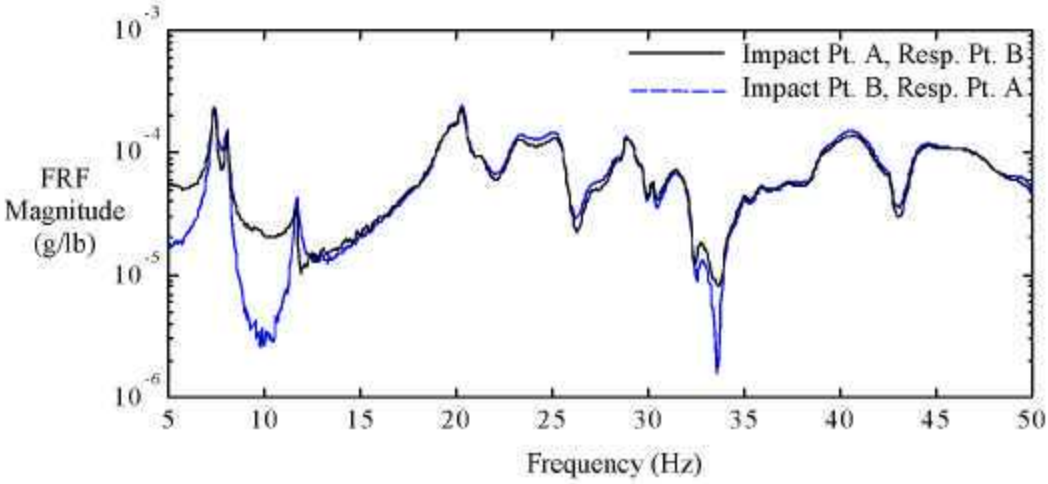

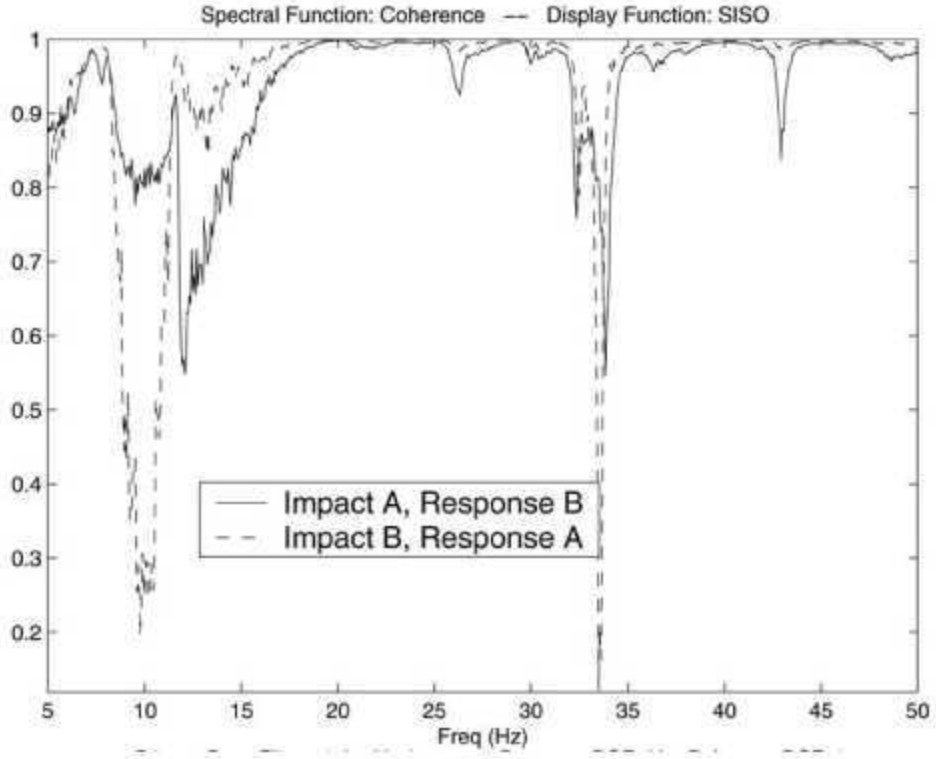

Figure 23. The FRFs and corresponding coherence functions measured during a reciprocity test on the Alamosa Canyon Bridge (see [15]). Measurements were conducted using the procedure depicted in Fig. 24.

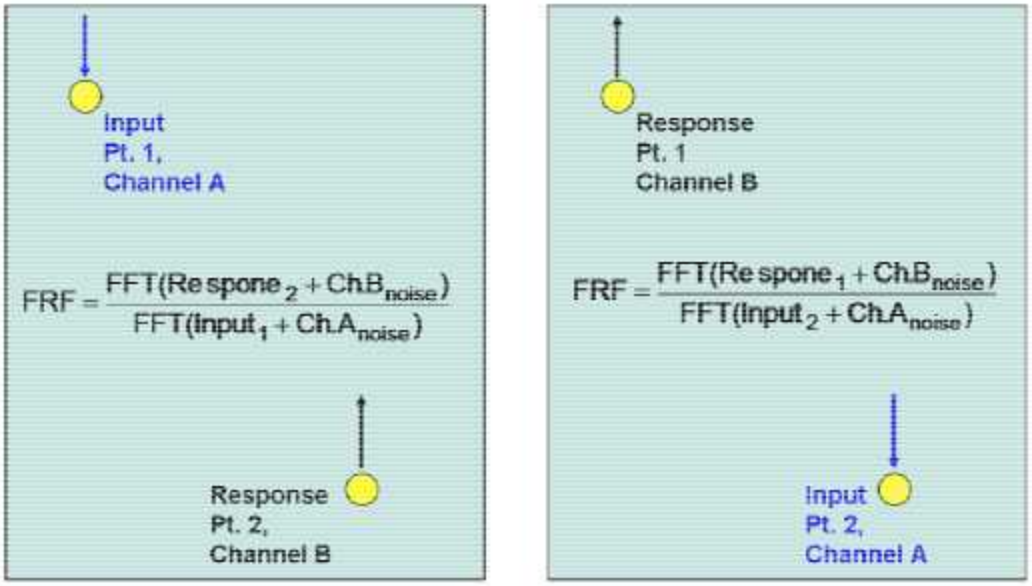

Figure 24. In this case, which corresponds to the measurement procedure used to obtain the reciprocity data in Fig. 23, one simply reverses the input and response measurement points. The input and response sensors remain connected to their original data acquisition channel. This approach measures the reciprocity of the structure and the data acquisition system.

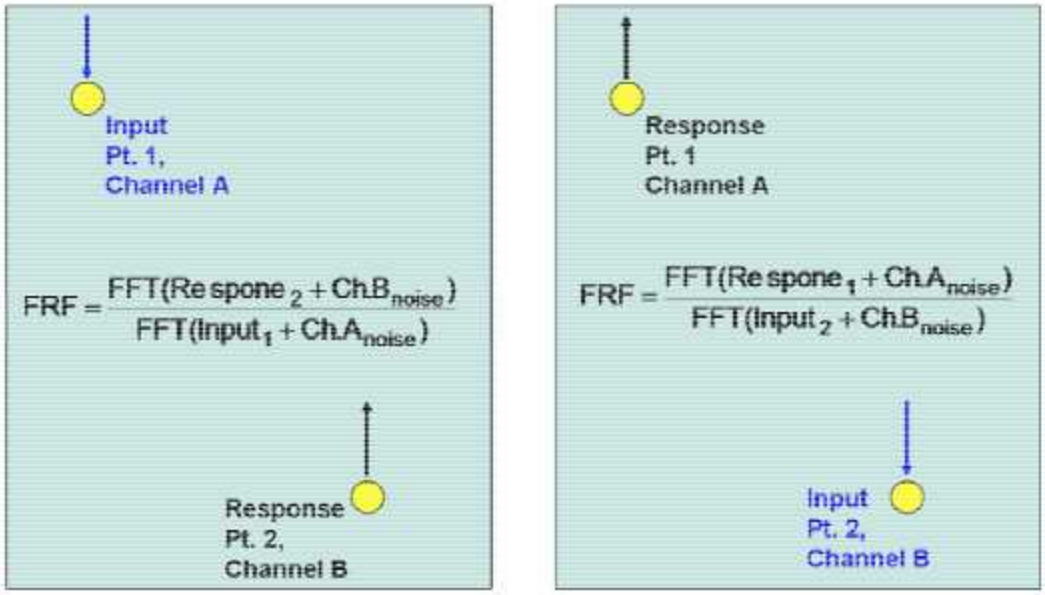

Figure 25. Alternatively, one can reverse the input and response measurement points while keeping the input and response sensors connected to data acquisition channels associated with the measurement point. This measurement procedure gives a measure of the reciprocity of the only structure.

Alternatively, one can keep the data acquisition channel associated with a particular location as depicted in Fig. 25. A plot of the FRF magnitudes when the accelerometers at points. A and B have been switched is shown in Fig. 26 along with the corresponding coherence functions. By switching the accelerometers the reciprocity being measured is that of the structure alone. From Figs. 23 and 26 it is evident that the structure itself is exhibiting reciprocity in the all portions of the spectrum where there is good coherence. Also, when Fig. 23 is compared to Fig. 26, it is evident that the noise in the measurement electronics of the data acquisition system is contributing to the loss of reciprocity, particularly near the third natural frequency at 11.5 Hz.

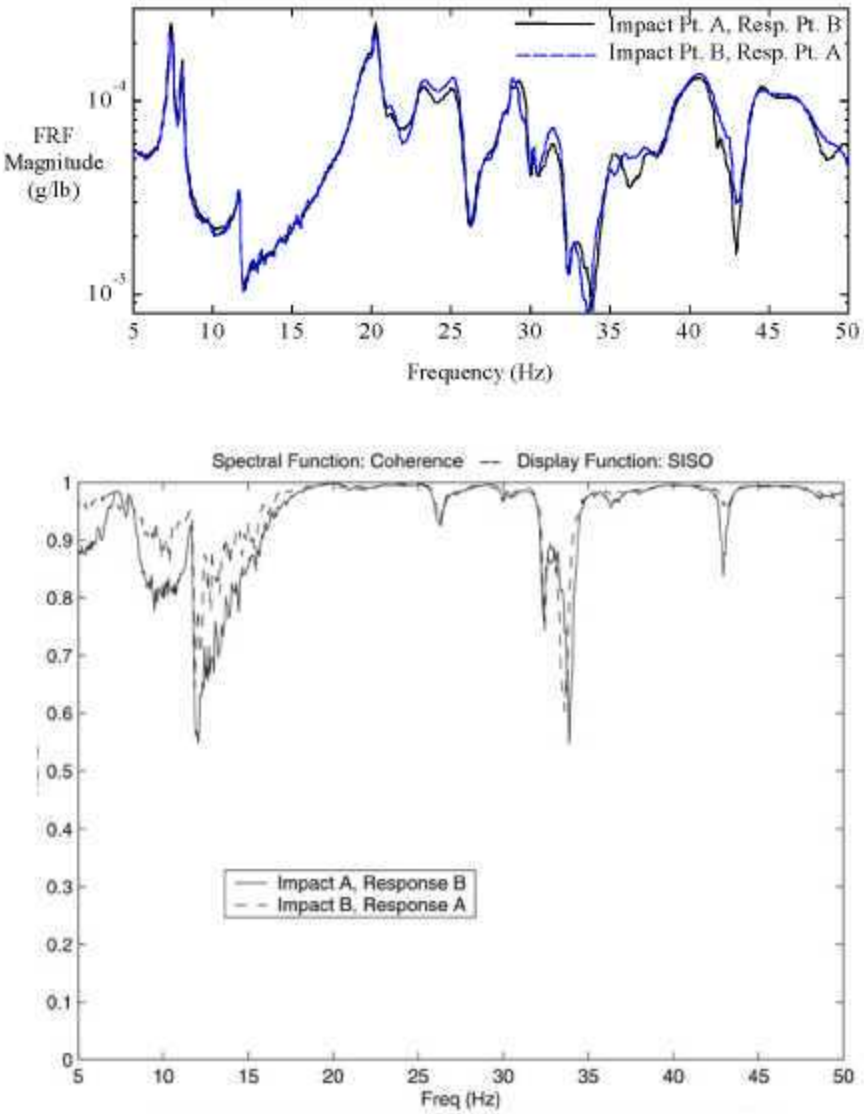

Figure 26. The FRFs and corresponding coherence functions measured during a reciprocity test on the Alamosa Canyon Bridge (see [15]). Measurements were conducted using the procedure depicted in Fig. 25.

Figures 27–30 show reciprocity check from the 4 DOF system when an impact excitation was applied at the first floor (mass 2) and acceleration response measurements were made at the base (mass 1) each of the floors (masses 2-4) (see Appendix B). The testing procedure used corresponds to that shown in Fig. 24. In these figures the FRF magnitude and corresponding coherence functions are shown for the cases when the structure is in a linear configuration and for the case where the excitation excites the impact nonlinearity. In these cases the linear structure exhibits reciprocity over all portions of the spectrum where consistent coherence between the two measurements was obtained. When the nonlinearity is excited, there are again considerable distortions of the FRFs as compared to those obtained from the linear system and the structure no longer exhibits reciprocity as indicated by the FRFs that do not overlay.

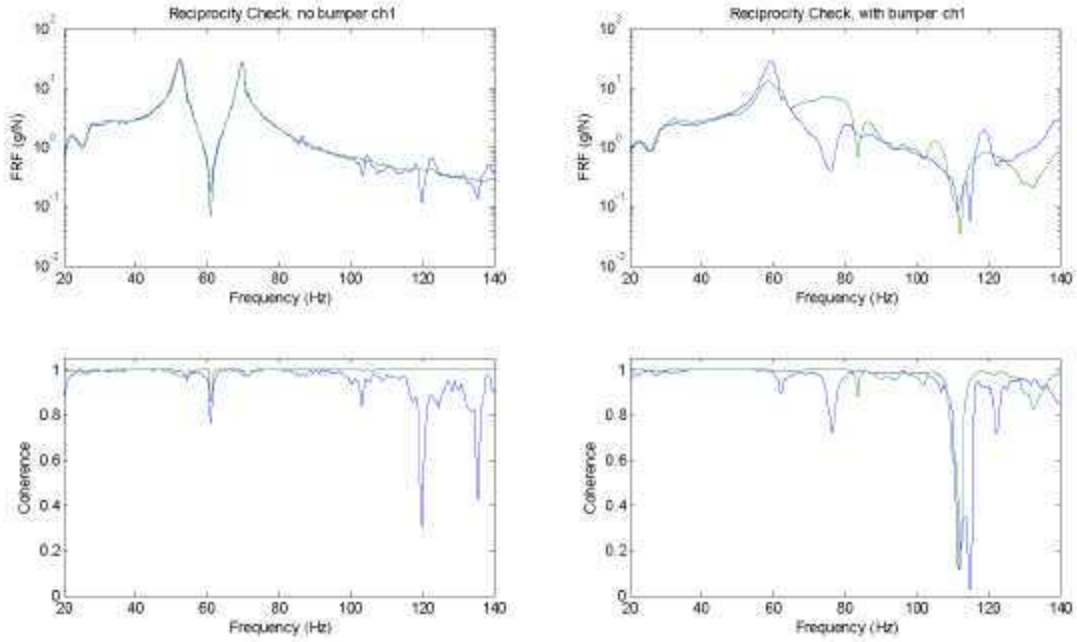

Figure 27. The FRFs and corresponding coherence functions measured during a reciprocity tests on the 4 DOF system without nonlinearity (left) and with an impact nonlinearity (right) (see Appendix B). Measurements were conducted using the procedure depicted in Fig. 24. Measurement locations were on the base (mass 1) and first floor (mass 2).

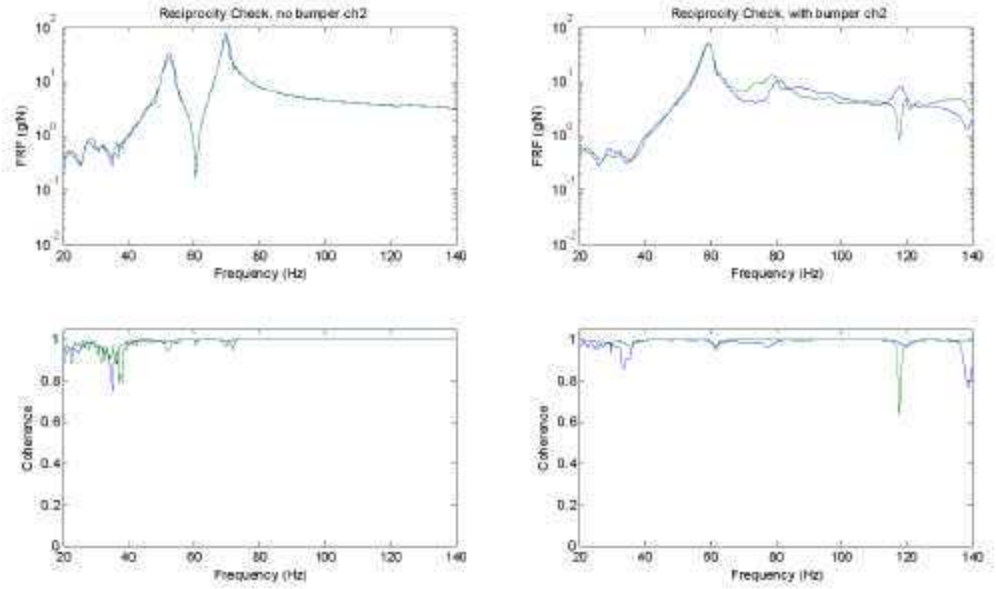

Figure 28. The FRFs and corresponding coherence functions measured during reciprocity tests on the 4 DOF system without nonlinearity (left) and with an impact nonlinearity (right) (see Appendix B). Measurements were conducted using the procedure depicted in Fig. 24. Measurement locations were on either end of the first floor (mass 2).

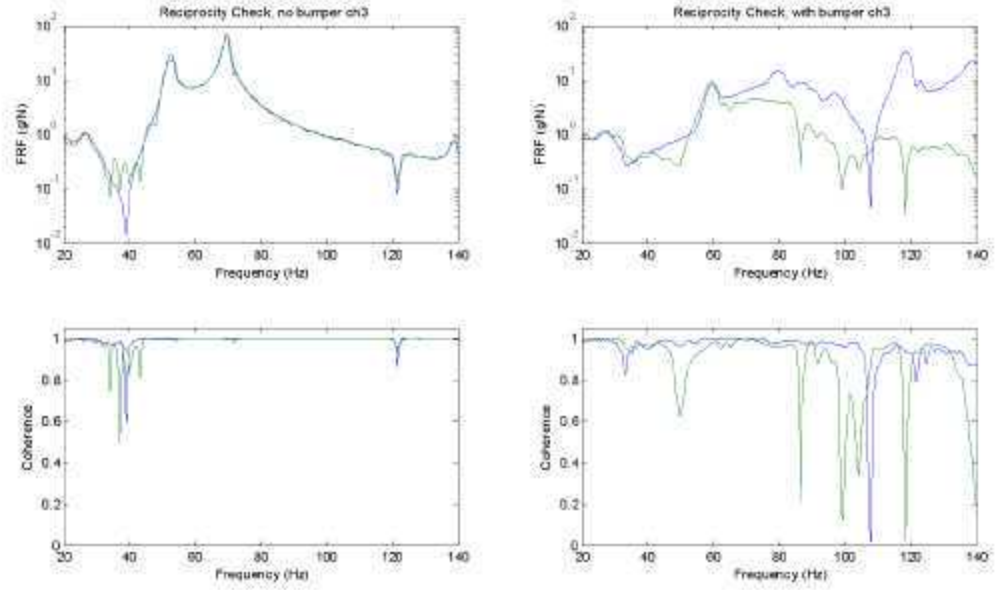

Figure 29. The FRFs and corresponding coherence functions measured during reciprocity tests on the 4 DOF system without nonlinearity (left) and with an impact nonlinearity (right) (see Appendix B). Measurements were conducted using the procedure depicted in Fig. 24. Measurement locations were on the first floor (mass 2) and second floor (mass 3).

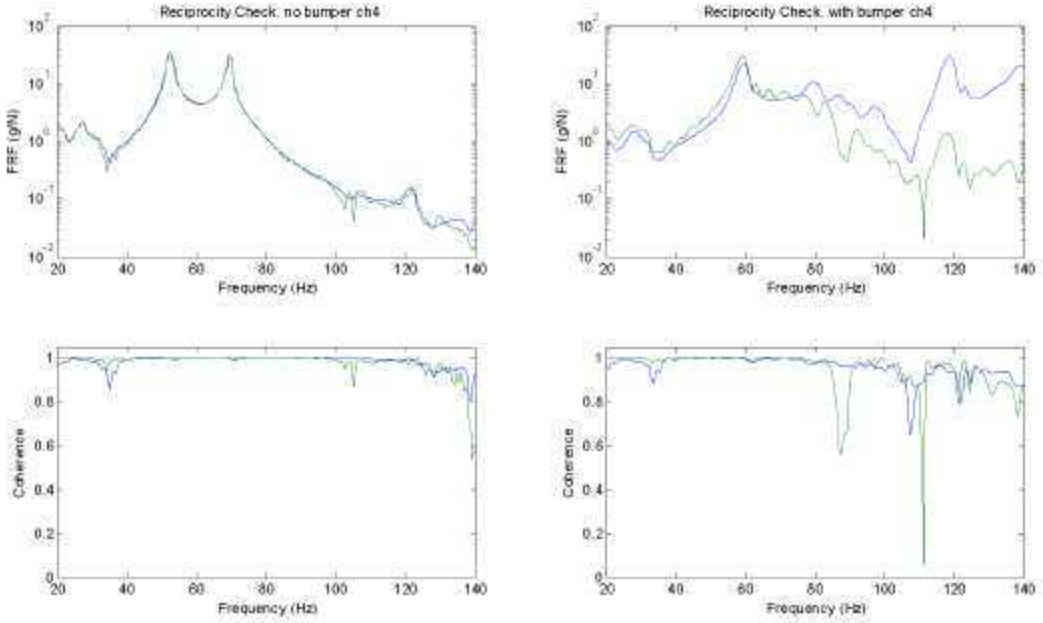

Figure 30. The FRFs and corresponding coherence functions measured during reciprocity tests on the 4 DOF system without nonlinearity (left) and with an impact nonlinearity (right) (see Appendix B). Measurements were conducted using the procedure depicted in Fig. 24. Measurement locations were on the first floor (mass 2) and third floor (mass 4).

6.4 Harmonic Distortion

Harmonic or waveform distortion is one of the clearest indicators of the presence of nonlinearity. Such distortions are the primary damage sensitive feature used to diagnose the condition of rotating machinery [17,26], which is the primary SHM application that has made the transition from research to practice. If the excitation to a linear system is a monoharmonic signal, i.e. a sine or cosine wave of frequency ω, the response will be monoharmonic at the same frequency (after any transients have died out) [24]. In addition, the response of a linear system to some initial disturbance (displacement or velocity impulse) can be represented by a sum of decaying sinusoids after transients have died out as described by the well-known convolution integral [20].

It is not always true to say that a sine wave input to a nonlinear system will not produce a sine wave output. However, this is usually the case and this is the basis of a simple and powerful test for nonlinearity as sine wave inputs are simple signals to generate in practice. The form of the distortion is due to the appearance of higher harmonics in the response. Similar higher harmonics are observed in the response of nonlinear systems excited by an initial displacement or by an initial velocity impulse.

Distortion can be easily detected by observing the input and output time response signals. Fig. 31 shows an example of harmonic distortion where a sinusoidal acceleration response signal is altered by, in this case, a cubic nonlinearity.

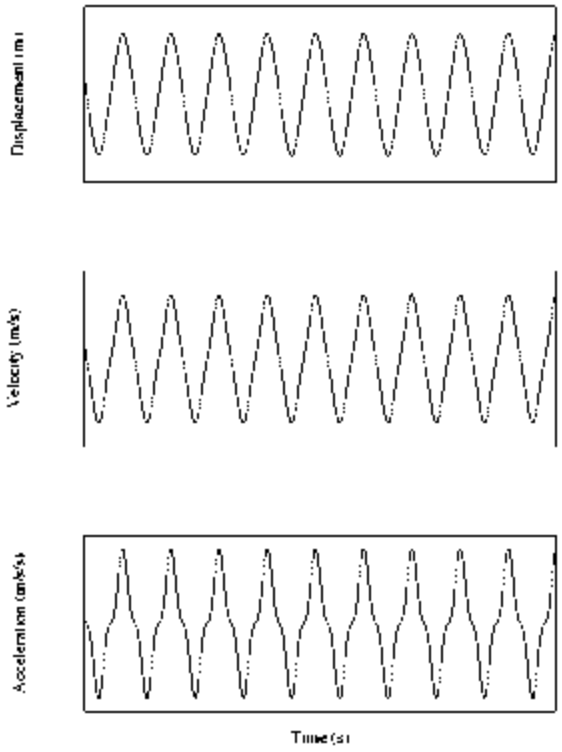

Figure 31. Evidence of distortion in time histories as a result of nonlinearity.

In Figure 31 the output response from a nonlinear system is shown in terms of the displacement, velocity and acceleration. The reason that the acceleration is more distorted compared with the corresponding velocity or displacement is easily explained. Let $f(t) = \sin(\omega t)$ be the input to the nonlinear system. The output, $x(t)$, will generally (at least for weak nonlinear systems) be represented as a Fourier series composed of harmonics written as,

$$x(t) = A_1 \sin(\omega t + \phi_1) + A_2 \sin(2\omega t + \phi_2) + A_3 \sin(3\omega t + \phi_3) \ldots \quad , \tag{20}$$

and the corresponding acceleration, $\ddot{x}(t)$, is,

$$\ddot{x}(t) = -\omega^2 A_1 \sin(\omega t + \phi_1) - 4\omega^2 A_2 \sin(2\omega t + \phi_2) - 9\omega^2 A_3 \sin(3\omega t + \phi_3) \ldots \tag{21}$$

Thus the n^{th} output acceleration term is weighted by the factor n^2 compared to the fundamental.

Harmonic generation can also be seen in systems subjected to nonsinusoidal inputs. Figure 32 shows the Wigner-Ville time-frequency transform applied to free-vibration response data measured at the free end of both uncracked and cracked cantilever beams subject to an initial displacement [27]. The crack is located at the midspan and penetrates half the thickness of the beam. The time-frequency plots in Fig. 32 show the generation of resonant frequency harmonics in the freely vibrating, cracked cantilever beam as well as the change in stiffness state as the crack opens and closes. A comparison of the two plots in Fig. 32 clearly shows that the presence of nonlinearity adds considerable complexity to the frequency response characteristics of the system and measures of this complexity relative to the undamaged system response can be used to infer the presence of damage.

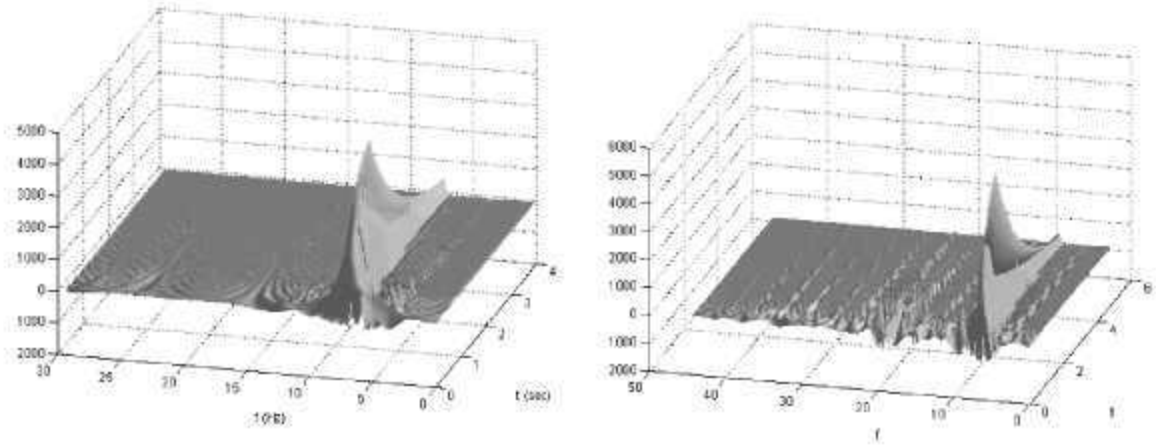

Figure 32. Wigner-Ville transforms of the free-vibration acceleration-time histories measured on an uncracked cantilever beam (left) and a cracked cantilever beam (right) subjected to an initial displacement.

Another illustration of harmonic distortion can be seen in data obtained from the 4 DOF system when the system is subjected to a 53 Hz harmonic base excitation. In one case the system is in a linear configuration and in the other case the excitation excited an impact nonlinearity (see Appendix B). Figure 33 shows a portion of input time histories and corresponding power spectra for the inputs from the two tests. This figure shows that the input remained constant between the two tests. Figures 34 though 37 show a portion of the input time histories and corresponding power spectra (normalized to a peak value of 1) from each floor for both the linear and nonlinear cases. The response measurements show increasing distortion from a harmonic response with increasing distortion from sensors closer to the impact location. Also, harmonics of the driving frequency are visible in the power spectra of the measurements made at the base (mass 1) and each of the floors (masses 2–4) when the impact nonlinearity is present. These harmonics are accompanied by significant drop in the amplitude of response even though Fig. 33 shows that the base excitation remained consistent in each test.

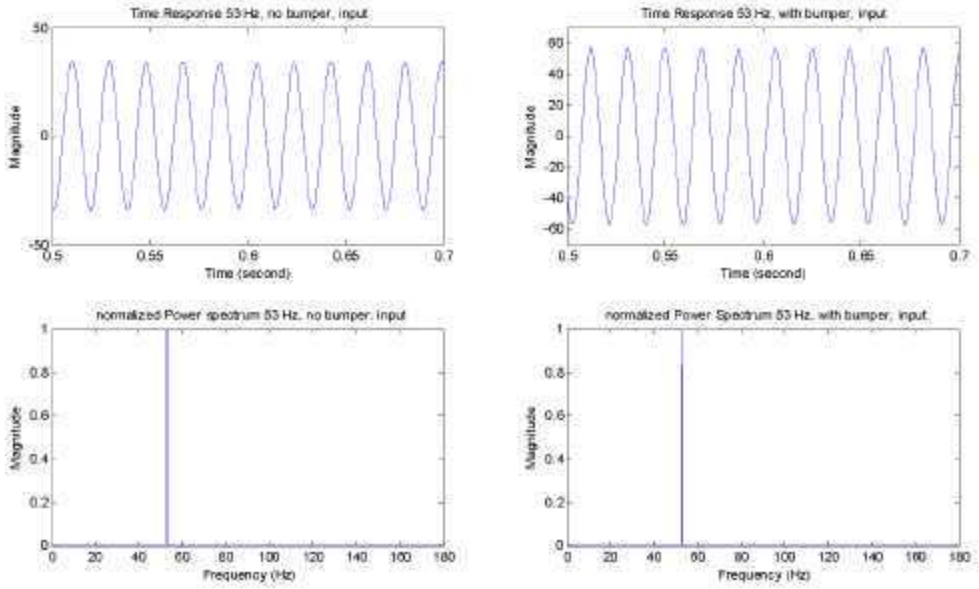

Figure 33. Harmonic base input signals (53 Hz) used to drive the 4 DOF system in its linear and nonlinear configuration.

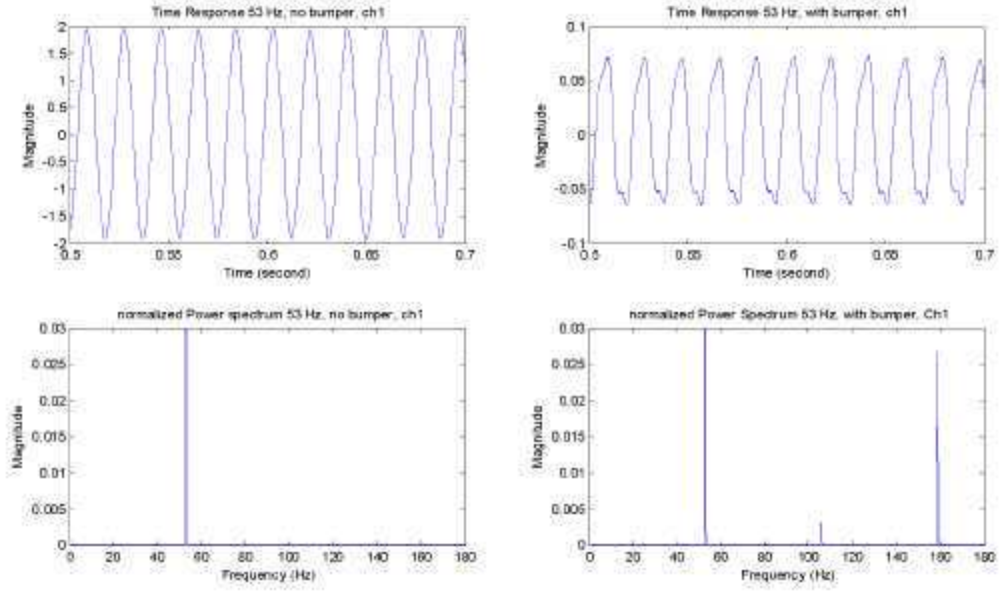

Figure 34. Base (mass 1) response to a 53 Hz harmonic base input signal used to drive the 4 DOF (see Appendix B) system in its linear and nonlinear configuration (impact between floors 2 and 3 [masses 3 and 4]). Peak Amplitudes in the spectra have been scaled to 1 and a peak amplitude of only 0.03 v^2 has been plotted to better show the harmonics that were generated.

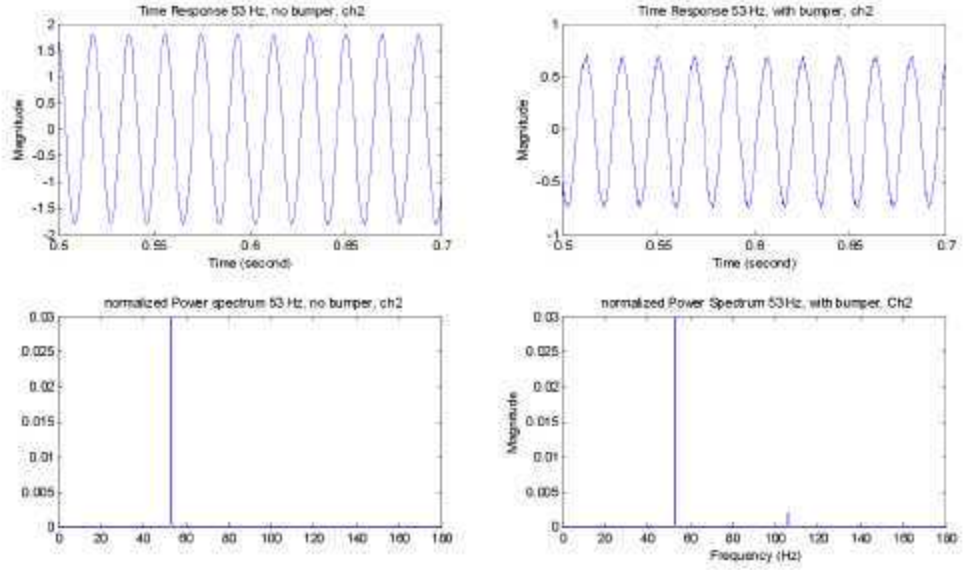

Figure 35. First floor (mass 2) response to a 53 Hz harmonic base input signal used to drive the 4 DOF (see Appendix B) system in its linear and nonlinear configuration (impact between floors 2 and 3 [masses 3 and 4]). Peak Amplitudes in the spectra have been scaled to 1 to better show the harmonics that were generated.

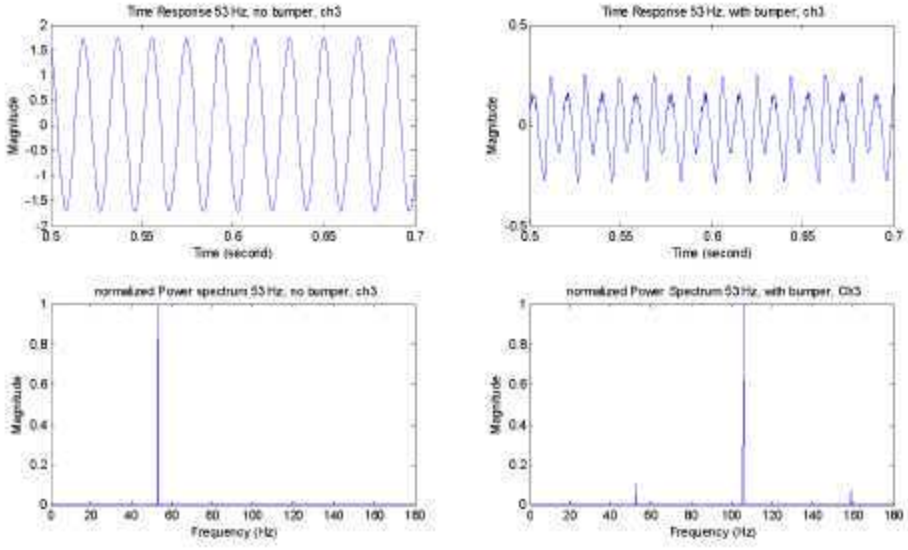

Figure 36. Second floor (mass 2) response to a 53 Hz harmonic base input signal used to drive the 4 DOF (see Appendix B) system in its linear and nonlinear configuration (impact between floors 2 and 3 [masses 3 and 4]). Peak Amplitudes in the spectra have been scaled to 1 to better show the harmonics that were generated.

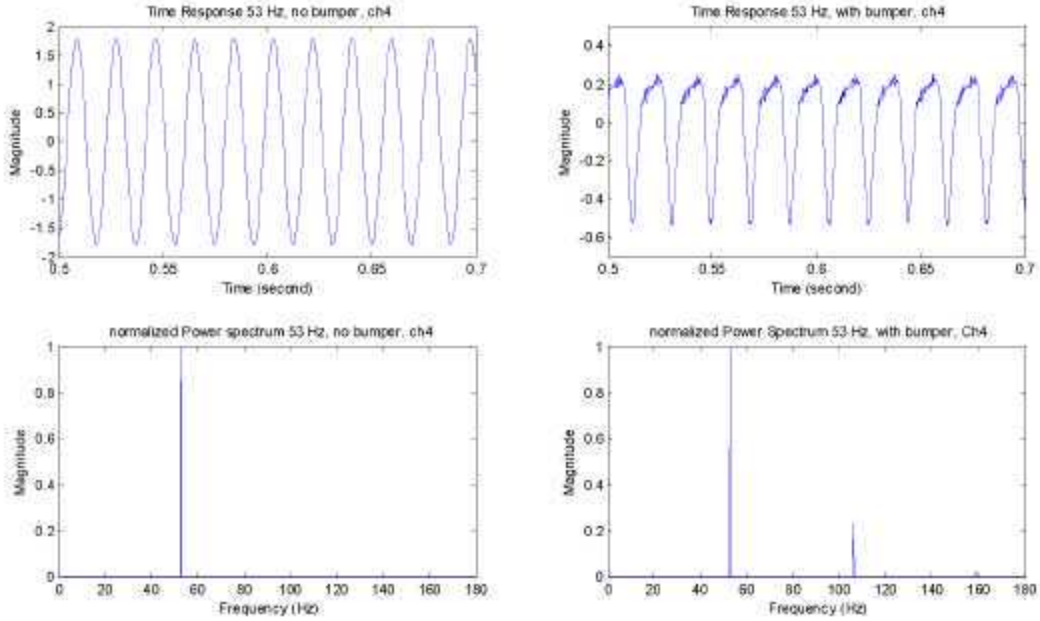

Figure 37. Third floor (mass 3) response to a 53 Hz harmonic base input signal used to drive the 4 DOF (see Appendix B) system in its linear and nonlinear configuration (impact between floors 2 and 3 [masses 3 and 4]). Peak Amplitudes in the spectra have been scaled to 1 to better show the harmonics that were generated.

In general, if the system inputs are nonsinusoidal waveforms, such as band-limited random signals, waveform distortion is difficult to detect and alternate features are required such as those that can be obtained from the coherence function or the probability density function.

6.5 Frequency Response Function Distortions

As previously discussed, damage can be inferred from the loss of amplitude invariance of any number of measured quantities when it is assumed that the system responds in a predominantly linear manner when in its undamaged state. One of the most fundamental constructs for modal analysis is the FRF; this takes a specific form for linear MDOF systems and departures from this form as the excitation level changes can yield information about the type of nonlinearity present in the system. The study of *FRF distortion* was the subject of some of the earliest attempts to reconcile nonlinearity with modal analysis [12].

Before discussing FRF distortion, recall the principal definitions of the FRF; first for a stepped-sine test. If a signal $Fsin(\omega t)$ is input to a linear system, it will result in a response $Xsin(\omega t+\phi)$; the FRF - a function of ω - is defined by,

$$H(\omega) = \left|\frac{X}{F}(\omega)\right| e^{i\phi(\omega)} \quad . \tag{22}$$

This quantity is very straightforward to obtain experimentally Over a range of frequencies, sinusoids $Fsin(\omega t)$ are injected sequentially into the system of interest At each frequency, the time histories of the input and response signals are recorded after transients have died out and Fourier transformed The ratio of the (complex) response spectrum to the input spectrum yields the FRF value at the frequency of interest In the case of a linear system, the FRF in Eq 22 summarizes the input/output process in its entirety and does not depend on the amplitude of excitation F In such a situation, the FRF is referred to as *pure*

In the case of a nonlinear system, it is well-known that sinusoidal forcing generates response components at frequencies other than the excitation frequency In particular, the distribution of energy amongst these frequencies depends on the level of excitation F, so the measurement process described above will also lead to a quantity which depends on F However, because the process is simple, it is often carried out experimentally in an unadulterated fashion for nonlinear systems The FRF resulting from such a test is referred to as *composite* and denoted by $\Lambda_s(\omega)$ Strictly speaking, $\Lambda_s(\omega, F)$ is more appropriate, but the amplitude argument will always be clear from in this context In the control literature, $\Lambda_s(\omega)$ is often called a *describing function*

The form of the composite FRF also depends on the type of excitation used If white noise of constant power spectral density P is used and the FRF is obtained by taking the ratio of the cross- and auto-spectral densities (S_{XF}, S_{FF}) for a linear system,

$$H(\omega) = \frac{S_{XF}(\omega)}{S_{FF}(\omega)} \quad , \tag{23}$$

and it is a textbook matter to show that this quantity is identical to the FRF from stepped-sine testing If however, the same approach is used for a nonlinear system, another composite FRF is obtained,

$$\Lambda_r(\omega, P) = \frac{S_{XF}(\omega)}{S_{FF}(\omega)} \quad , \tag{24}$$

and the function $\Lambda_r(\omega, P)$ is distinct from the $\Lambda_s(\omega, F)$ obtained from a stepped-sine test The object of this section is to outline some ways of computing FRFs, in the hope that the analysis can be used to identify nonlinearities that are indicative of damage

The first calculation will illustrate a well-known means of approximating $\Lambda_s(\omega)$ - the analytical analogue of the stepped-sine test - the method of *harmonic balance* [28] A nonlinear system is needed and without a doubt the most commonly referenced SDOF nonlinear system is given by Duffing's equation,

$$m\ddot{x} + c\dot{x} + kx + k_3x^3 = f(t) \tag{25}$$

and this will be adopted for the analysis here

Harmonic balance simply assumes that the response to a sinusoidal excitation is a sinusoid at the same frequency The trial solution $X\sin(\omega t)$ is substituted in the equation of motion,

$$m\ddot{x} + c\dot{x} + kx + k_3x^3 = F\sin(\omega t - \phi) \tag{26}$$

To simplify matters the phase has been transferred onto the input to allow Y to be taken as real The substitution yields,

$$-m\omega^2 X\sin(\omega t) + c\omega X\cos(\omega t) + kX\sin(\omega t) + k_3X^3\sin(\omega t) = F\sin(\omega t - \phi) \quad , \tag{27}$$

or, after a little elementary trigonometry,

$$-m\omega^2 X\sin(\omega t) + c\omega X\cos(\omega t) + kX\sin(\omega t) + k_3X^3\left\{\frac{3}{4}\sin(\omega t) - \frac{1}{4}\sin(\omega t)\right\} = \tag{28}$$
$$F\sin(\omega t)\cos\phi - F\cos(\omega t)\sin\phi$$

Equating the coefficients of $\sin(\omega t)$ and $\cos(\omega t)$ (the *fundamental* components) yields the equations,

$$-m\omega^2 X + kX + \frac{3}{4}k_3X^3 = F\cos\phi, \text{ and} \tag{29}$$

$$c\omega X = -F\sin\phi \quad . \tag{30}$$

The required gain and phase follow routinely,

$$\left|\frac{X}{F}\right| = \frac{1}{\left[\left\{-m\omega^2 + k + \frac{3}{4}k_3X^2\right\}^2 + c^2\omega^2\right]^{1/2}} \text{ , and} \tag{31}$$

$$\phi = \tan^{-1}\frac{-c\omega}{-m\omega^2 + k + \frac{3}{4}k_3X^2} \quad , \tag{32}$$

and these can be combined into the complex FRF,

$$\Lambda_s(\omega) = \frac{1}{k + \frac{3}{4}k_3X^2 - m\omega^2 + ic\omega} \tag{33}$$

At a fixed level of excitation, the FRF has natural frequency,

$$\omega_n = \sqrt{\frac{k + \frac{3}{4}k_3 X^2}{m}} \quad , \tag{34}$$

so it depends on X and hence, indirectly on F. If $k_3 > 0$, the natural frequency increases with F; such a system is referred to as *hardening*. If $k_3 < 0$ the system is *softening*; the natural frequency decreases with increasing F.

This approximation reproduces experimental results which show that the natural frequency changes with amplitude. Further, the actual form of the FRF can depart substantially from the linear form. For given F and ω, X is obtained by solving the (essentially) cubic Eq. 29. As complex roots occur in conjugate pairs, Eq. 29 will either have one or three real solutions. The effect of this observation is well-known, but remains striking.

At low levels of excitation, the FRF is a barely distorted version of that for the underlying linear system as the k term dominates for $X << 1$. A unique response amplitude (a single real root of Eq. 29 is obtained for all ω. As F increases, the FRF becomes more distorted and departs from the linear form, but a unique response is still obtained for all ω. This continues until F reaches a critical value F_{crit} where the FRF has a vertical tangent. Beyond this point a range of ω values, $[\omega_{low}, \omega_{high}]$, is obtained over which there are three real solutions for the response. This is a *bifurcation point* of the parameter F. As the test or simulation steps past the point ω_{low}, two new responses become possible and persist until ω_{high} is reached and two solutions disappear. The graph of the response is shown in Fig. 38.

The relevant experimental circumstances for this analysis occur during a stepped-sine or a sine-dwell test. Consider an upward sweep. A unique response exists up to $\omega = \omega_{low}$. However, beyond this point, the response stays on branch $x^{(1)}$ essentially by continuity. This condition persists until, at frequency ω_{high}, $x^{(1)}$ ceases to exist and the only solution is $x^{(3)}$, a jump to this solution occurs giving a discontinuity in the FRF. Beyond ω_{high} the solution stays on the continuation of $x^{(3)}$, which is the unique solution in this range. The amplitude follows path ABD in Figure 38. The type of FRF obtained from such a test is shown in Fig. 39. The downward sweep is similarly described and follows path DCA.

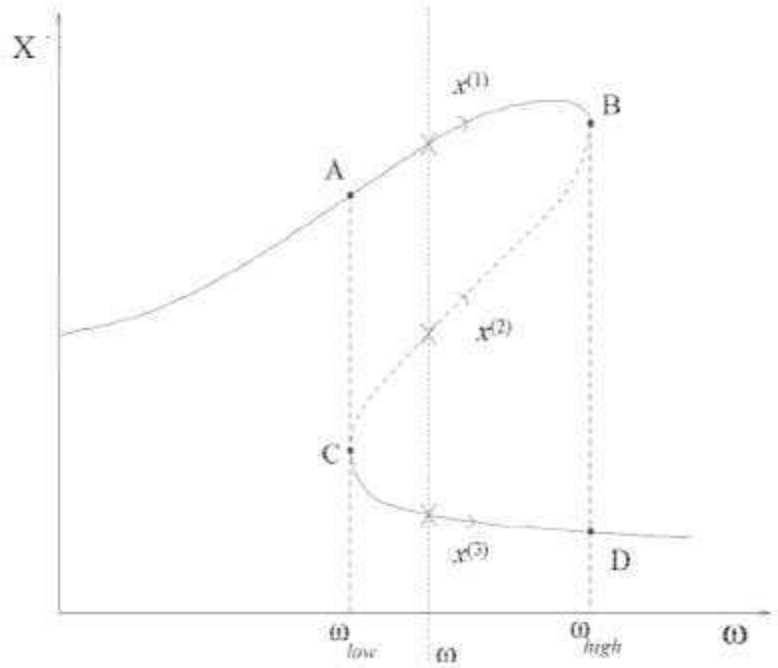

Figure 38. Possible response amplitudes for Duffing oscillator under high level excitation.

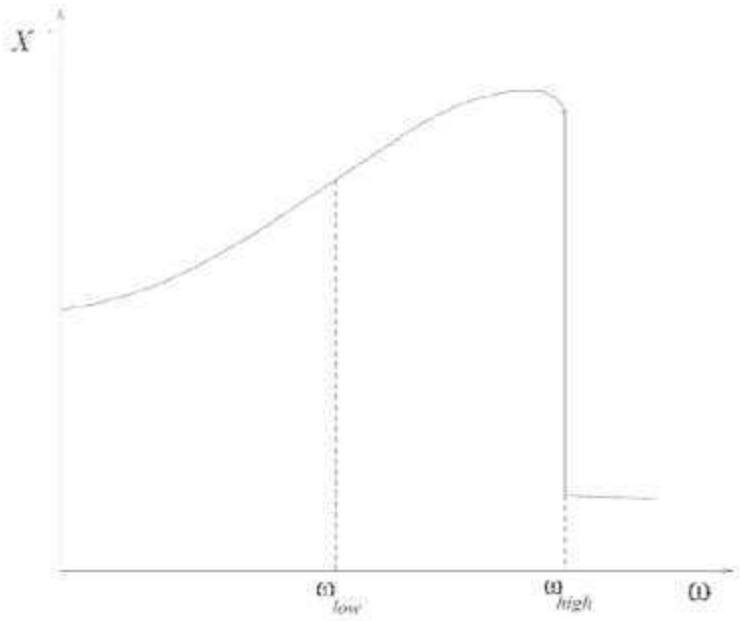

Figure 39. Composite FRF Λ_s for Duffing oscillator at high excitation (upward sweep).

If $k_3 > 0$, the resonance peak moves to higher frequencies and the jumps occur on the right-hand side of the peak as described above. If $k_3 < 0$, the jumps occur on the left of the peak and the resonance shifts downward in frequency. These discontinuities are frequently observed in experimental FRFs. All this is fairly well-known; however, despite the fact that this was one of the first calculations carried out for a nonlinear system, it retains its predictive power and harmonic balance, and its more modern variants are indispensable tools in the analysis of nonlinear systems.

6.6 Probability Density Function

When a linear system is subject to a random input whose amplitudes are described by a Gaussian distribution, the response amplitudes will also have a Gaussian distribution [29]. Also, it is known that a Gaussian distribution has well defined properties such as skewness,

$$\frac{E(\ddot{x} - \mu_{\ddot{x}})^3}{\sigma_{\ddot{x}}^3} = 0 \quad , \tag{35}$$

and the normalized kurtosis,

$$\frac{E(\ddot{x} - \mu_{\ddot{x}})^4}{\sigma_{\ddot{x}}^4} = 3 \quad , \tag{36}$$

where E designates the expectation operator, μ is the sample mean for an acceleration response, $\ddot{x}$ and σ is the sample variance.

When the input is known to be Gaussian in nature, deviations of the acceleration response statistics can result when nonlinearities associated with damage are present. As an example, an estimate of the acceleration response pdf obtained with a kernel density estimator from an 8 DOF system is shown in Fig. 40(a) along with skewness and kurtosis values. This response corresponds to the end mass and the excitation is applied to the mass at the opposite end [30, 31]. The estimated pdf is plotted over the Gaussian distribution that has been fit to these same data. For this undamaged condition the small deviations in the pdf and the associated statistics from those anticipated for a Gaussian input are attributed to an open-loop control system on the shaker that does not allow for a true Gaussian signal to be input to the system. Figure 40(b) shows a similar plot and similar statistics when the same eight DOF system is modified such that impacting occurs between the two end masses located at the opposite end from the shaker. This impacting produces an asymmetry in the response that manifests itself as a more than 500% change in the skewness value as well as a more significant deviation in the pdf from the normal condition.

If baseline statistics are available from the undamaged system, examination of the pdf and the associated statistics can be an indicator of nonlinearities associated with damage. These statistics are used extensively as low-dimension features to diagnose damage to roller bearings [32].

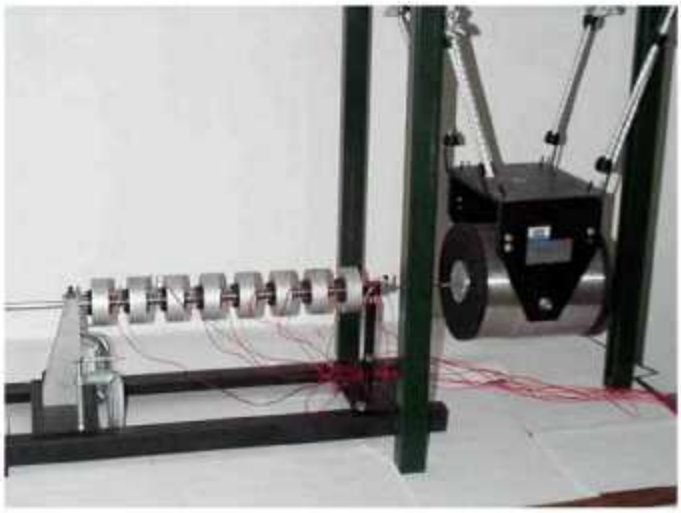

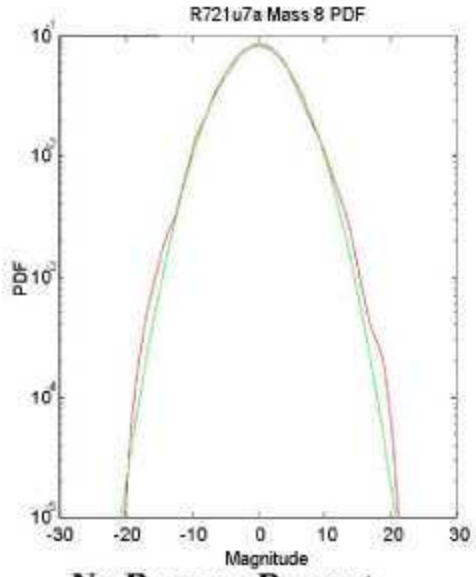

No Bumper Present

Skewness=0.121 Std=0.158

Kurtosis= 3.277 Std=0.084

(a)

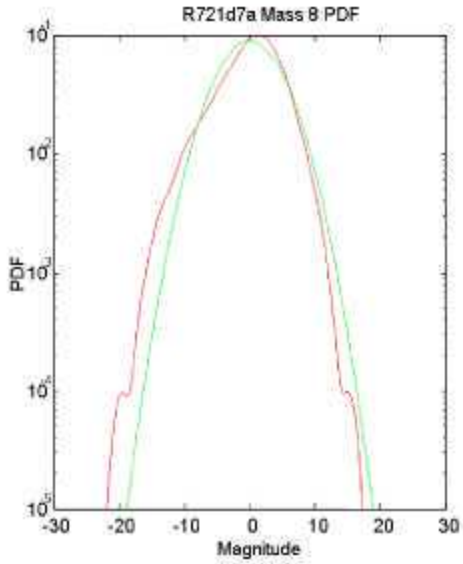

Bumper Present

Skewness=0.768 Std=0.161

Kurtosis= 3.644 Std=0.112

(b)

Figure 40. The 8 DOF system (top) and (a) The pdf of the acceleration response measured on the end mass of the system in its undamaged condition overlaid with a Gaussian distribution fit to these same data. (b) a similar pdf obtained when the end two masses impact.

6.7 Correlation Tests

There are two simple correlation tests that can signal nonlinearity by analyzing measured time data. If records of both input f and output x are available, it can be shown that the correlation function, $\phi_{f^2x'}(k)$, defined as

$$\phi_{f^2x'}(k) = E\left[f(i)^2 x'(i+k)\right] \tag{37}$$

where E designates the expectation operator. $\phi_{f^2x'}$ vanishes for all discrete time delays, k, if and only if the system is linear [33]. The apostrophe signifies that the mean has been removed from the output signal.

If only sampled outputs are available, it can be shown that under certain conditions [34], the correlation function defined as,

$$\phi_{x'x'^2}(k) = E[x'(i+k)x'(i)^2] \tag{38}$$

is zero for all k if and only if the system is linear. In practice, these functions will never be identically zero; however, confidence intervals for a near-zero result can be calculated. As an example, acceleration data were obtained from single degree of freedom system with an offset bilinear stiffness whose force-deformation plot is shown in Fig. 41. The system was subjected to a random excitation. The correlation functions for the response at both low and high excitation are shown in Fig. 42. The dashed lines are the 95% confidence limits for a zero result based on a linear system with the initial stiffness. The function in Fig. 42b indicates that the data from the high-excitation test arises from a nonlinear system. The low-excitation test did not excite the nonlinearity and the corresponding function (Fig. 42a) shows that only approximately five percent of the points are outliers as would be expected.

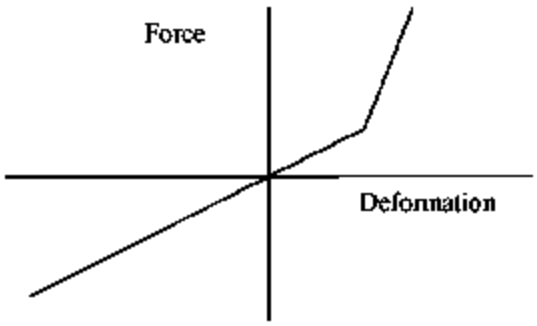

Figure 41. Offset bilinear stiffness system.

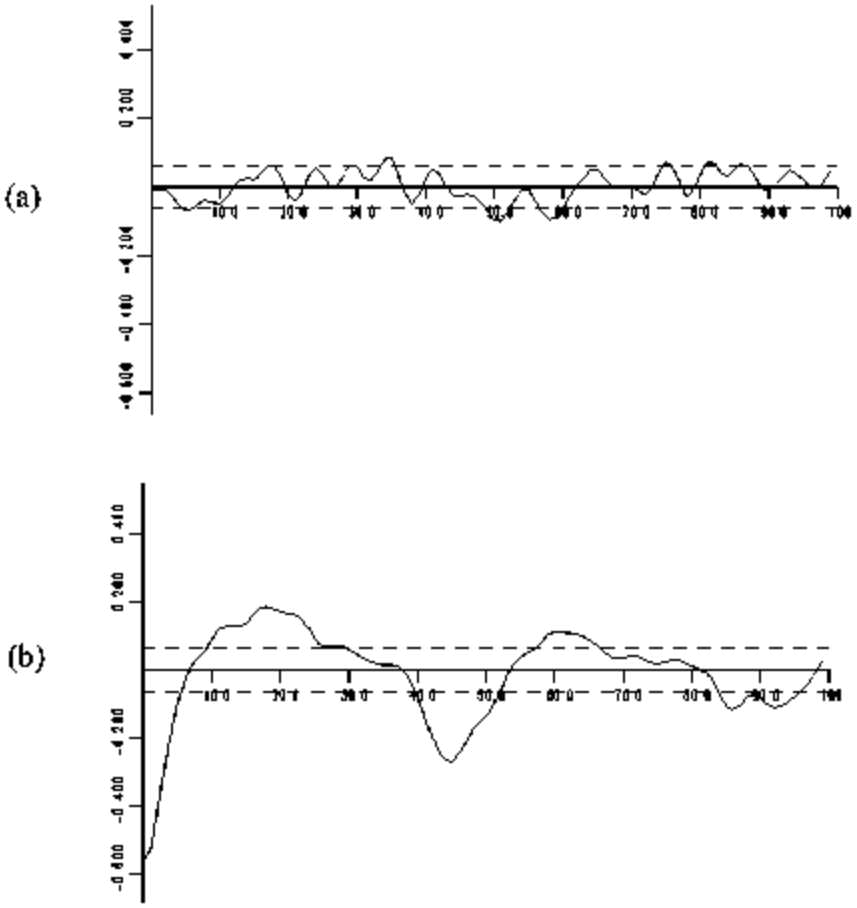

Figure 42. Correlation functions for a (a) linear system and (b) nonlinear system.

Note that Eq 38 as it stands only detects even nonlinearity such as quadratic stiffness In practice, to identify odd nonlinearity, the input signal should contain a D C offset This offsets the output signal and adds an even component to the nonlinear terms

A further restriction on Eq 38 is that it cannot detect odd damping nonlinearity as it is not possible to generate a D C offset in the velocity to add an odd component to the nonlinearity There are implications for damage detection here as the occurrence of damage in a structure may result in the appearance of a friction nonlinearity when the damage allows two surfaces to slide over each other

6.8 The Holder Exponent

Robertson, et al [35] have used the Holder exponent as another damage-sensitive feature This feature identifies nonlinearities associated with discontinuities introduced into the dynamic response data as a result of certain types of damage such as cracks opening and closing In [35] a procedure for capturing the time varying nature of the Holder exponent has been developed based on wavelet transforms This procedure has been successfully applied to detect loose parts in a harmonically excited mechanical system as described below

The Holder Exponent, also known as the Lipschitz Exponent [36], is a tool that provides information about the regularity of a signal. In essence, the regularity identifies to what order the signal is differentiable. For instance, if a signal *f(t)* is differentiable at $t = 0$, it has a Holder Exponent of 1 or greater. If the signal is discontinuous but bounded in the neighborhood of t = 0, such as a step function, then the Holder Exponent is 0. The Dirac Delta function then has a Holder Exponent of -1 because it is unbounded at t = 0. From these examples, one can see that there is a relationship between the Holder Exponent of a function and its derivatives and primitives. Taking the derivative of a function decreases its regularity by 1 and integrating increases it by 1. For SHM applications the assumption is that a linear system will have a continuous response to random, transient or steady state excitation. When a nonlinearity is introduced such as a crack opening and closing, the response signals will have discrete portions that are discontinuous and the Holder exponent will identify such discontinuities.

The Holder regularity is defined as follows. Assume that a signal *f (t)* can be approximated locally at t_0 by a polynomial of the form [37]:

$$\begin{aligned} f(t) &= c_0 + c_1(t-t_0) + \ldots + c_n(t-t_0)^n + C\left|t-t_0\right|^\alpha \\ &= P_n(t-t_0) + C\left|t-t_0\right|^\alpha \end{aligned}, \tag{39}$$

where P_n is a polynomial of order n and C is a coefficient. The term associated with the exponent α can be thought of as the residual that remains after fitting a polynomial of order n to the signal, or as the part of the signal that does not fit into an $n+1$ term approximation [37]. The local regularity of a function at t_0 can then be characterized by this "Holder" exponent:

$$\left|f(t) - P_n(t-t_0)\right| \le C\left|t-t_0\right|^\alpha \tag{40}$$

A higher value of α indicates a better regularity or a smoother function. In order to detect singularities, a transform is needed that ignores the polynomial part of the signal. A wavelet transform that has n-vanishing moments is able to ignore polynomials up to order n:

$$\int_{-\infty}^{\infty} t^n \psi(t)dt = 0 \quad . \tag{41}$$

Transformation of Eq. 40 using a wavelet with at least n vanishing moments then provides a method for extracting the values of the Holder exponent in time:

$$\left|Wf(u,s)\right| \le Cs^\alpha \quad . \tag{42}$$

The wavelet transform of the polynomial is zero and so what remains is a relationship between the wavelet transform of *f(t)* and the error between the polynomial and *f(t)*, which relates to the regularity of the function. When a complex wavelet such as the Morlet wavelet is used, the resulting coefficients are also complex. Therefore, the magnitude of the modulus of the wavelet transform must be used to find the Holder exponent. As detailed below, the exponent α can be calculated at a specific time point by finding the slope of the log of the modulus at that time versus the log of the scale vector *s*.

For the SHM applications, singularities are defined as points in the sensor time history that are discontinuous. As discussed above, bounded discontinuities have a Holder exponent of 0. Therefore, measuring the regularity of the signal in time can be used to detect these singularities. The Holder exponent can pertain to the global regularity of a function, or it can be found locally. A common method for finding its value is through the use of the Fourier transform [36]. The asymptotic decay of a signal's frequency spectrum relates directly to the uniform Holder regularity. However, the Fourier transform approach only provides a measure of the minimum global regularity of the function, and cannot be used to find the regularity at a particular point in time. Wavelets, on the other hand, are well localized in time and can therefore provide an estimate of the Holder regularity both over time intervals and at specific time points. The wavelet method for estimating the Holder exponent is similar to that of the Fourier transform. The wavelet provides a time-frequency map called the scalogram. By examining the decay of this map at specific points in time across all scales (frequencies), the point-wise Holder regularity of the signal can be determined.

It is logical therefore to wonder if a short-time Fourier transform (STFT) can be used to extract a time-varying Holder exponent function as well. In fact, any time-frequency transform can be used for Holder exponent extraction, but certain characteristics of the wavelet transform make it particularly well adapted for this application. Specifically, these characteristics are: the decay of the wavelet basis functions in the frequency domain, which is associated with the number of vanishing moments, and the variability of the bandwidth of the wavelet transform in time and frequency. The order of the wavelet limits the degree of regularity that can be measured in a function. Therefore, wavelets can be tuned to the signals that are being analyzed. Also, the variability of the time and frequency bandwidths provides a finer time resolution at the higher frequencies than the STFT, which can be helpful in detecting the point in time when sudden changes occur in a signal.

The easiest way to identify a discontinuity in a signal is by looking for a distinct downward jump in the regularity (Holder exponent) versus time plot. As previously mentioned a discontinuous point should have a Holder Exponent value of zero, but resolution limitations of the wavelet transform will result in slightly different values. So, identifying time points where the Holder Exponent dips from positive values towards zero, or below, will identify when the discontinuities in the signal occur. A procedure for identifying the discontinuities will be presented in the following sections.

The steps for calculating the Holder exponent in time are as follows. First, take the wavelet transform of the given signal and take the absolute value of the resulting coefficients to obtain the wavelet transform modulus:

$$|Wf(u,s)| = \left| \int_{-\infty}^{\infty} f(t) \frac{1}{\sqrt{s}} \psi^* \left(\frac{t-u}{s} \right) dt \right|. \tag{43}$$

Arrange the coefficients in a two-dimensional time-scale matrix. One dimension of the time-scale matrix (u) represents a different time point in the signal, and the other dimension denotes a different frequency scale (s). Take the first column, which represents the frequency spectrum of the signal at the first time point, and plot the log of it versus the log of the scales, s, at which the wavelet transform was calculated. This can be shown mathematically by taking the log of each side of Equation 43:

$$\log |Wf(u,s)| = \log(C) + \alpha \log(s) \quad . \tag{44}$$

Ignoring the offset due to the coefficient C, the slope m of a straight line fit to the spectrum is then the decay of the wavelet modulus across its scales. Negating the slope will give the decay versus the frequencies of the transform rather than the scales, due to the inverse relationship between scale and frequency. The Holder exponent α is then simply the slope m. This is the Holder exponent for the first time point in the signal. To find the Holder exponent at all time points, repeat this process for each time point of the wavelet modulus matrix.

$$m = \frac{\log |Wf(u,s)|}{\log(s)} = \alpha \tag{45}$$

The following example shows the application of the Holder exponent to data from a mechanical system with a loose part that was subjected to a harmonic base excitation. A schematic of the test structure is shown in Fig. 43. The non-symmetric bumpers cause the structure to exhibit a rattle during one portion of the excitation. Figure 44 shows the response of the structure as measured by accelerometers mounted on the outer structure in the in-axis and off-axis directions. The rattle produced by these impacts is evident in the sensor measurements that are off-axis from the excitation. The short oscillations of increased magnitude in these measurements are indicative of the rattle. These same oscillations are not readily apparent in the in-axis data, particularly if one does not have the off-axis measurements for reference.

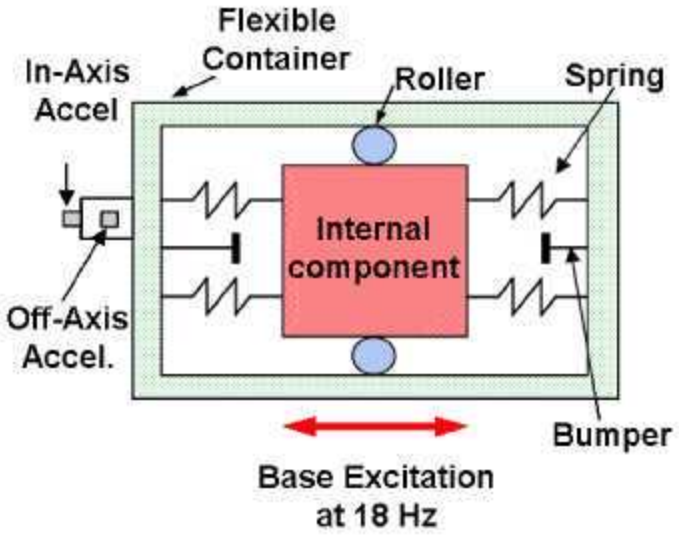

Figure 43. Schematic diagram of the test structure that had a loose internal part.

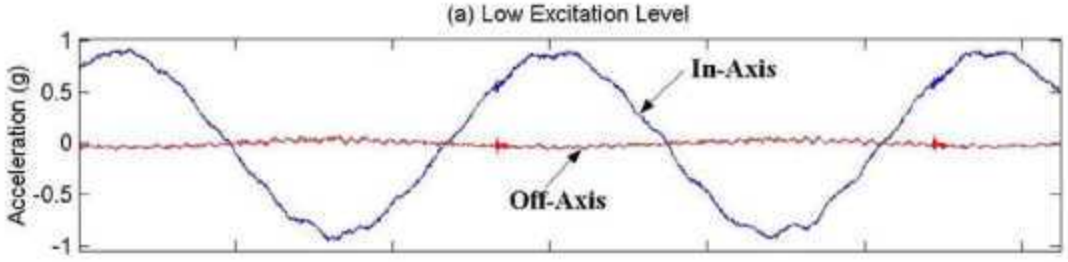

Figure 44. Acceleration response of the test structure as measured in the in-axis and off-axis directions by accelerometers mounted on the outer structure.

In Figure 45 the Fourier transform of the first quarter (1024 points) of the in-axis response, which contains no rattle, is compared to the Fourier transform of the second quarter of this same signal, which does contain a rattle. Examination of the two frequency spectra reveals that the presence of the rattle in the second set of data is not discernable using a Fourier transform. In Figure 46, the wavelet and STFT transforms of each of the signals is given. Lines of high magnitude coefficients are visible in these plots.

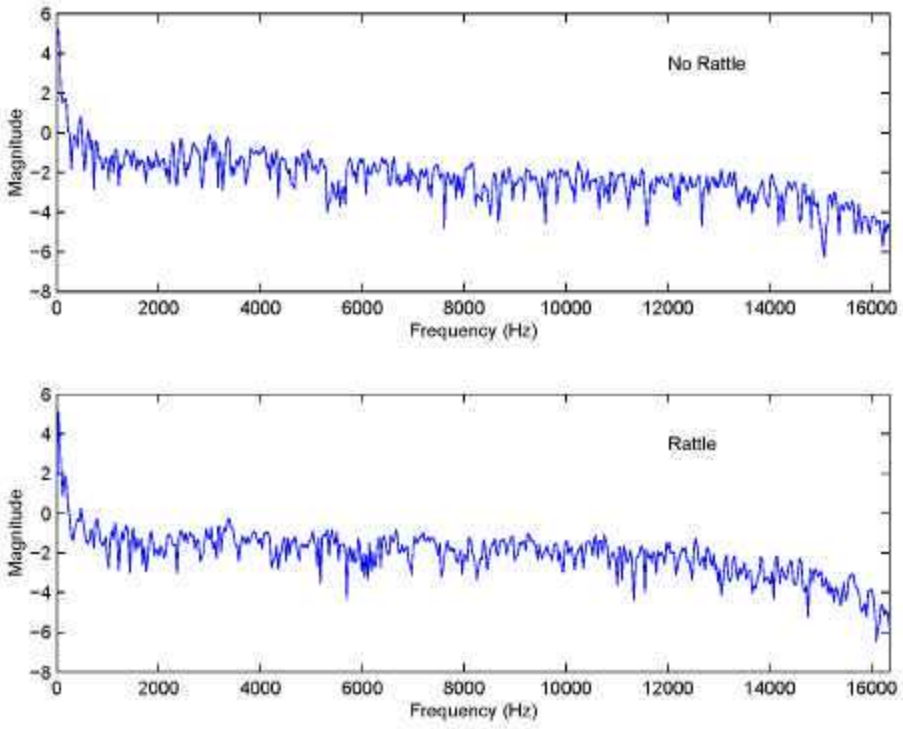

Figure 45. A comparison of the Fourier transforms of the signal with (second quarter of signal) and without (first quarter of signal) the rattle present.

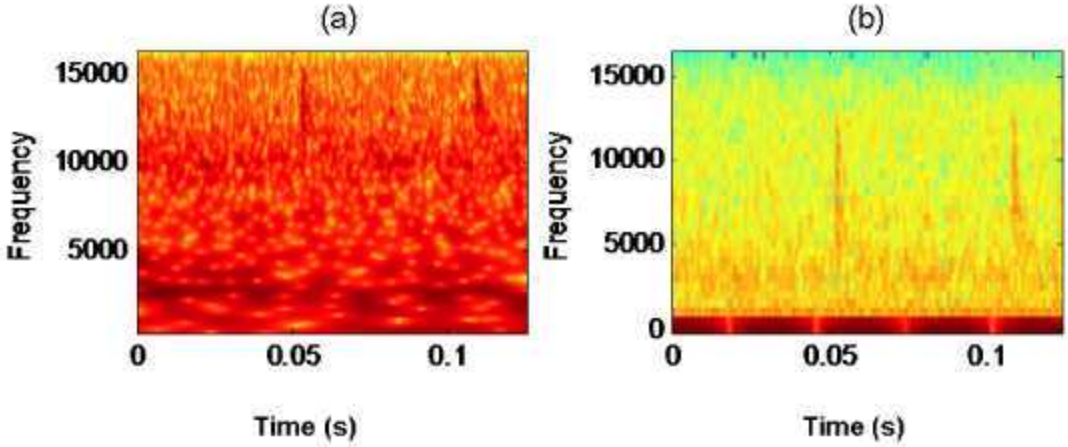

Figure 46. Transforms of test structure response: (a) wavelet transform and (b) short term Fourier Transform.

Extraction of the Holder exponent was then performed using the wavelet transform for the in-axis data, as shown in Figure 47. When compared to Fig. 44, which is plotted on the same time scale, the singularities associated with the rattle are clearly visible in this plot at each time they occur during the oscillatory cycles. For this example, the number of scales was 64, and a Morlet wavelet, 16, was used. The larger width wavelet helped to smooth the Holder exponent function in time, bringing out the more significant changes.

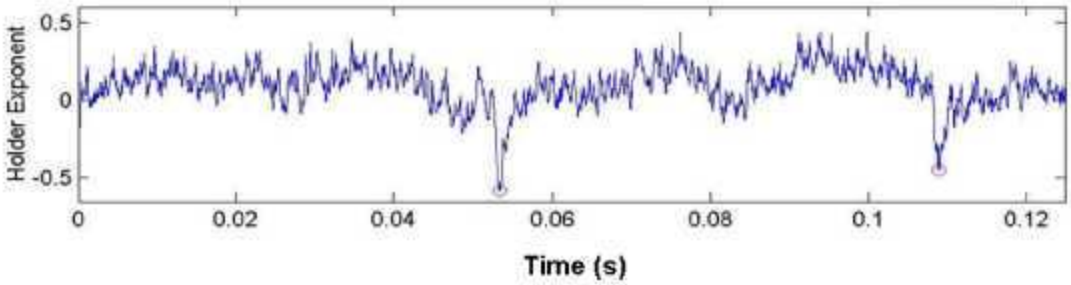

Figure 47. The Holder exponent extracted from the wavelet modulus for the in-axis acceleration data.

6.9 Linear Time Series Prediction Errors

A general approach to feature extraction for systems that exhibit the transition to nonlinear response characteristics as a result of damage is to first fit a linear model to the data obtained from the undamaged structure that is assumed to be responding in a linear manner. This model is then used to predict the measured system response and a residual error is calculated at each time step, which is the difference between the measured and predicted response. This same model is then used to predict the response from data obtained in the potentially damaged state. The assumption is that this linear model will no longer accurately predict the response of the damaged system that is exhibiting nonlinear response and there will be a significant increase in the residual errors associated with this latter prediction. This approach can also signal damage even if the damage does not cause nonlinear response. In this case the procedure does not detect nonlinearity, but rather a deviation from the baseline linear model.

In theory, this approach can be taken with either physics-based models such as finite element models or with data-driven models such as time-series models. The time series models are relatively simple to fit to measured response data and the application of one such model to damage detection in a system that exhibits nonlinear response in its damaged state is illustrated below.

A n^{th} order autoregressive (AR) time-series model is defined as

$$\hat{x}_i = \sum_{j=1}^{n} a_j (x_{i-j}) + \varepsilon_i \ , \tag{46}$$

where $\hat{x}_i$ is the estimate of the i^{th} time series value, n is the model order, $x_{i-j} = j^{th}$ previous measured time series values, a_j are the AR coefficients and ε_i is assumed to be an

unobservable random error with zero mean and constant variance. If $\hat{x}_i$ denotes the estimated acceleration measurement from the fitted AR model, then the residual at time i is

$$\varepsilon_i = x_i - \hat{x}_i . \tag{47}$$

If the fitted model accurately represents the measured signal, the residuals should be nearly uncorrelated. Note that for a fitted n^{th} order model residuals cannot be computed for $i < n$. From a pattern recognition perspective, the residuals can be thought of as features derived from the measured time histories. This feature is of dimension one and many estimates of this feature are obtained from a typical time series.

A key to employing this method is to determine the appropriate model order. A higher order model may end up fitting the noise in the data and, hence will not generalize to other data sets. On the other hand, if one selects a low order model it will not necessarily capture the underlying physical system response. There are a variety of techniques for choosing the model order, such as Akaike's information criterion or a partial autocorrelation function, which is a plot of the magnitude of the last coefficient as a function of model order, often employed to help decide the appropriate model order. A summary of these techniques can be found in most textbooks on time series analysis [38]. In the example below a fifth-order AR model (AR(5)) is applied to the 8192 point acceleration time series data from Sensor 1 on the concrete column tests described in Appendix A. This model has the form:

$$x_t = a_1 x_{t-1} + a_2 x_{t-2} + a_3 x_{t-3} + a_4 x_{t-4} + a_5 x_{t-5} + \varepsilon_t . \tag{48}$$

Typical time series lead to an over determined set of equations that must be solved to obtain estimates of the AR coefficients. For a 8192 point time series the coefficients a_i are solved for by applying the pseudoinverse technique to the following equation to obtain a least square solution for the AR coefficients:

$$\begin{bmatrix} x_1 & x_2 & x_3 & x_4 & x_5 \\ x_2 & x_3 & x_4 & x_5 & x_6 \\ \vdots & \vdots & \vdots & \vdots & \vdots \\ x_{8187} & x_{8188} & x_{8189} & x_{8190} & x_{8191} \end{bmatrix} \begin{Bmatrix} a_5 \\ a_4 \\ \vdots \\ a_1 \end{Bmatrix} = \begin{Bmatrix} x_6 \\ x_7 \\ \vdots \\ x_{8192} \end{Bmatrix} , \tag{49}$$

To compare the residual errors obtained from data measured on the undamaged structure with similar quantities obtained from the structure in its various states of damage, an X-bar control chart is developed using the time history acceleration measurements taken before the column was damaged (Test 6), denoted as damage level 0. An AR(5) model is fit to these data. Figure 48 shows plots of the original signal and an overlay of the signal generated with AR model. From these plots one can qualitatively observe that the AR model developed from the undamaged data appears to do a pretty good job of predicting these data. Figure 49 shows a histogram of the residual errors from this fit and a Gaussian distribution that was fit to these data. One indication that the AR model is accurately

predicting the time series is indicated by a Gaussian-distributed residual error. Figure 49(a) shows that these residual errors are normally distributed. Depending on the type of nonlinearity introduced by the damage, the distribution of residual errors obtained when the AR model developed for the undamaged case is used to predict data from the damage case may or may not be Gaussian.

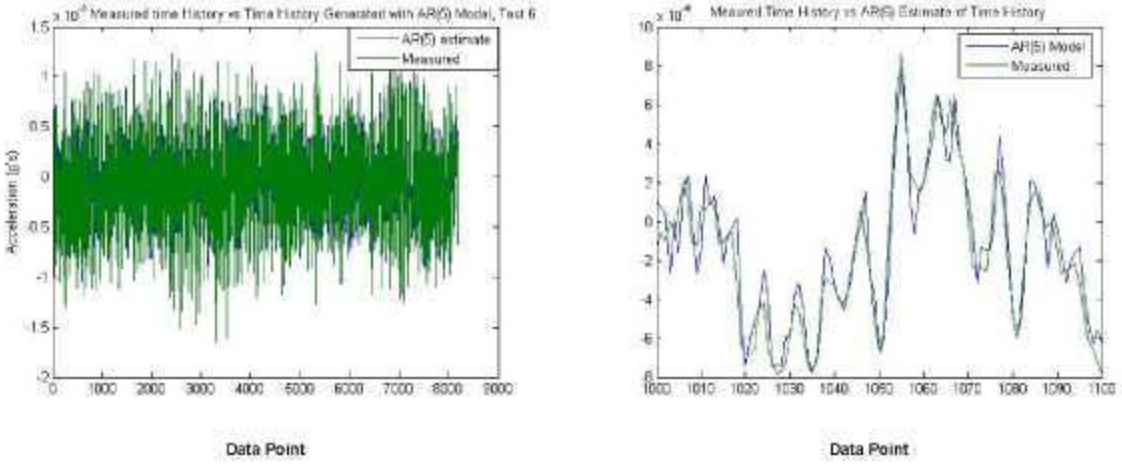

Figure 48. A comparison of the measured acceleration time history and the time series generated by the AR model for the column in its undamaged state.

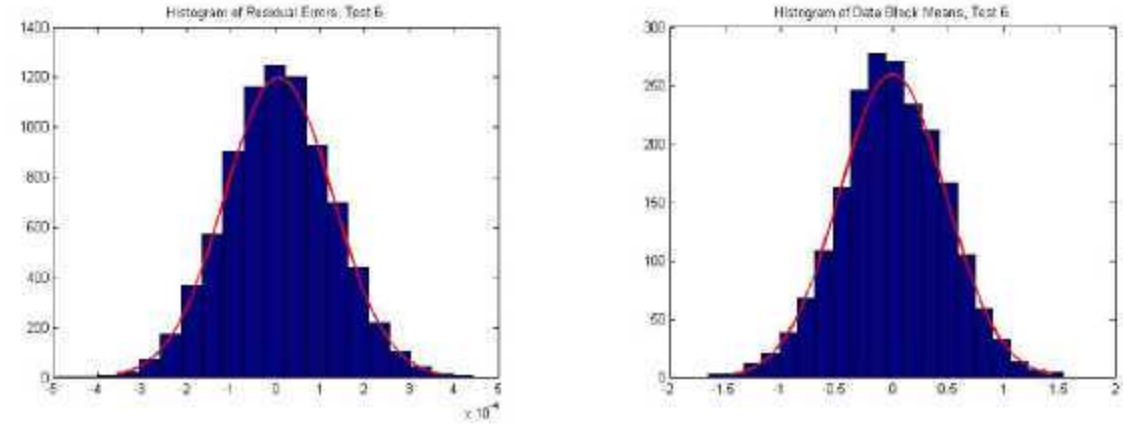

(a) (b)

Figure 49. (a) is a histogram of the AR model residual errors for the undamaged case and a Gaussian distribution fit to these same residual errors. (b) is the same plot for the mean of groups of four residual errors.

Next, an *X*-bar control chart is constructed based on the residuals from this fitted model using subgroups of size 4. As mentioned previously, there are 8192 acceleration measurements. Residuals can be computed for acceleration measurements 6-8192. For convenience, the last 3 residuals are discarded which leaves 8184 residuals. Subgroups of size 4 are constructed by placing the residuals for observations 6-9 in the first group, 10-13 in the second group and so on. This process produces 2046 subgroups of residuals each of size 4. Prior to computing subgroup means and variances, the 8184 residuals, from damage level 0, are normalized by subtracting the mean, μ_ε , and dividing by the standard deviation, σ_ε, of the entire ensemble. The residuals from the incipient damage level (Test 7) where the column was deformed to a point where the rebar first yields and two subsequent damage levels (2.5 and 7 times the deformation that caused incipient yielding, tests 9 and 11) are also adjusted by subtracting μ_ε and dividing by σ_ε from the damage level 0 data. The histogram of the mean values of these subgroups for the undamaged case is shown in Fig. 49 (b).

The centerline of the chart is the sample mean of the charted values. This centerline is the sample mean of the residuals from observations 6-8189, and, after the normalization just described, is 0. The sample variance of each subgroup is determined and these variances are then averaged to give a pooled estimate of variance. A simple average is appropriate because each subgroup is of size 4. The square root of the pooled variance, s_p, is used as an estimate of the population standard deviation. Control limits are drawn at $0 \pm z_{\alpha/2} s_p / \sqrt{n}$ where n=4 and z_α represents the α quantile of the standard normal distribution. For this examples, α was chosen to be 0.01. A more detailed description of the x-bar control chart development can be found in [39]. The X-bar control charts for the undamaged case and for the three damage cases are plotted in Fig. 50.

Note that the upper and lower control limits are determined only with data from the undamaged column and then the control chart was subsequently used to identify outliers in the feature vectors from the other tests. In Figure 50 the three plots corresponding to Test 7, 9 and 11 all show a statistically significant number of features that are outside the control limits. In this case the features are the mean of the 4-point data blocks extracted from the residual error time series. The 3σ confidence intervals used imply that approximately 1% of the data (or approx. 20 points for these 2046 point series) can be expected to fall outside the control limits under normal conditions. For the undamaged case 13 points fall outside the confidence limits. For plots associated with each of the damage cases, the number of points falling outside the control limits is significantly greater than 20.

The strongest indication of damage, as identified by the number of points outside the control limits, is associated with the incipient damage case (Test 7). Fewer outliers, compared to the other damage levels, were detected for damage levels corresponding to Tests 9 and 11. Although not rigorously verified, it is speculated that this trend in damage indication is related to yielding of the rebar. The first damage level corresponds to incipient yielding of the rebar. Because of strain compatibility, this incipient yielding is accompanied by cracking of the concrete. The shaker, which was driven with the same input voltage level during each test, is most likely to cause a non-linear response associated

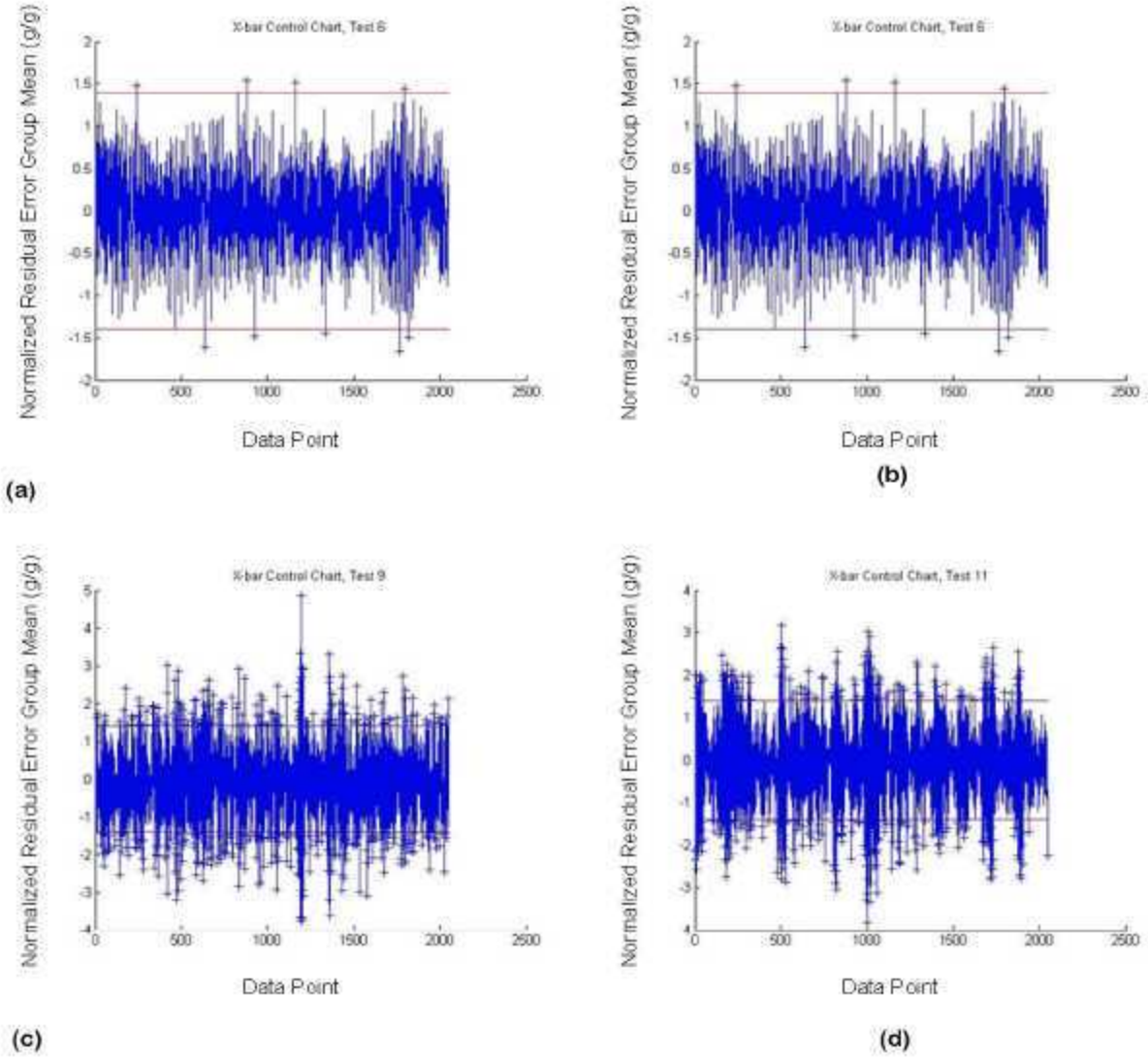

Figure 50. The X-bar control plot of the mean of the residual error groups for (a) data from the undamaged structure, (b) data from the incipient damage level, (c) data from structure that was deformed to 2.5 times the incipient damage level, and (d) data from the structure when it was deformed to 7 times the incipient damage level.

with the cracks opening and closing at this first damage level. At the higher damage levels, the rebar has yielded significantly. When load was removed from the column, this yielding tended to hold the cracks in an open configuration during the subsequent dynamic tests. The excitation provided by the shaker, which was maintained at a consistent amplitude, could not excite the nonlinearities associated with cracks opening and closing to the same degree when the rebar had yielded significantly.

6.10 Nonlinear Auto-Regressive Moving Average with Exogenous Inputs Models

In the previous section a linear time series model was fit to measured system data, and then that model was used to predict system response when damage was present. The underlying assumption was that if the damage caused a nonlinearity, the model would not predict data from the damaged system well, which would manifest itself as an increase in the residual errors between the measured and predicted responses. In this section a method is described to predict the time series with a nonlinear model. This approach has the advantage over the previous linear approach in that it can be better applied to a system that responds in a nonlinear manner in its initial undamaged state. The parameters of the model as well as the residual error can be used as damage sensitive features. In application of this approach to damage detection, one must assure that the model accurately represents the response of the system over the entire range of input. If this process is not done, damage could be inferred when in reality the model does not accurately predict the response to some new loading scenario.

Suppose one is interested in the previously defined SDOF linear system,

$$m\ddot{x} + c\dot{x} + kx = f(t). \tag{50}$$

This equation of motion can be converted by a process of discrete approximation to the discrete-time form,

$$x_t = a_1 x_{t-1} + a_2 x_{t-2} + b_1 f_{t-1}, \tag{51}$$

where a_1, a_2 and b_1 are constants and functions of the original constants m, c, k and the sampling interval $\Delta t = t_{t-1} - t_t$ where the t_t are the sampling instants. In a more general form,

$$x_t = F(x_{t-1}, x_{t-2}, f_{t-1}). \tag{52}$$

Equation 52 represents an Auto-Regressive with eXogenous inputs(ARX) model. The advantage of adopting this model form is that only the two states x and f need be measured in order to estimate all the model parameters a_1, a_2 and b_1 in Eq. 51 and thus identify the system. It is a simple matter to show that a general MDOF linear system has a discrete-time representation,

$$x_t = \sum_{j=1}^{n_x} a_j x_{t-j} + \sum_{j=1}^{n_f} b_j f_{t-j}, \tag{53}$$

or,

$$x_t = F(x_{t-1}, \ldots x_{t-n_x}; f_{t-1}, \ldots f_{t-n_f}). \tag{54}$$

As before, all parameters $a_1 \ldots a_{n_y}; b_1 \ldots b_{n_f}$ can be estimated using measurements of the x and f data only.

The extension to nonlinear systems is straightforward. Consider the Duffing oscillator represented by,

$$m\ddot{x} + c\dot{x} + kx + k_3 x^3 = f(t). \tag{55}$$

One can pass to the discrete-time representation,

$$x_t = a_1 x_{t-1} + a_2 x_{t-2} + b_1 f_{t-1} + c x_{t-1}^3. \tag{56}$$

The model defined by Eq. 56 is now termed a Nonlinear ARX (NARX) model. The regression function $x_t = F(x_{t-1}, x_{t-2}; f_{t-1})$ is now nonlinear; it contains a cubic term. If *all* terms of order three or less were included in the model structure i.e. $(x_{t-2})^2 f_{t-1}$ etc. a much more general model would be obtained,

$$x_t = F^{(3)}(x_{t-1}, x_{t-2}; f_{t-1}), \tag{57}$$

where the superscript above F denotes the highest order product terms which would be sufficiently general to represent the behavior of any dynamical systems with nonlinearities up to third order i.e. containing terms of the form $\dot{x}^3, \dot{x}^2 x$, etc.

The most general polynomial NARX model (including products of order $\leq n_p$) is denoted by,

$$x_t = F^{(n_p)}(x_{t-1}, \ldots x_{t-n_y}; f_{t-1}, \ldots f_{t-n_f}). \tag{58}$$

It has been proved by Leontaritis and Billings [40, 41] under very mild assumptions that any input/output process has a representation by a model of this form. If the system nonlinearities are polynomial in nature, this model will represent the system well for all levels of excitation. If the system nonlinearities are not polynomial, they can be approximated arbitrarily accurately by polynomials over a given range of their arguments (Weierstrass approximation theorem [42]). This means that the system can be accurately modeled by taking the order n_p high enough. However, the model would be input-sensitive as the polynomial approximation required would depend on the data. This problem can be removed by including non-polynomial terms in the NARX model as described in Billings and Chen [43]. The NARX model can even be cast as a Neural Network [44].

The preceding analysis unrealistically assumes that the measured data is free of noise. As shown below, if the system is nonlinear the noise process can be very complex; multiplicative noise terms with the input and output are not uncommon, but can be easily accommodated in the discrete-time models [40, 41, 45, 46].

Suppose the measured output has the form,

$$x(t) = x_c(t) + \zeta(t) \ , \tag{59}$$

where $x_c(t)$ is the "clean" output from the system. If the underlying system is the Duffing oscillator of Eq. 55, the equation satisfied by the measured data is now,

$$m\ddot{x} + c\dot{x} + kx + k_3x^3 - m\ddot{\zeta} - c\dot{\zeta} - k\zeta - k_3\zeta^3 - 3x^2\zeta + 3x\zeta^2 = f(t) \ , \tag{60}$$

and the corresponding discrete-time equation will contain terms of the form $\zeta_{t-1}, \zeta_{t-2}, \zeta_{t-1}y_{t-1}^2$ etc. Note that even simple additive noise on the output introduces cross-product terms if the system is nonlinear. Although these terms all correspond to unmeasurable states, they must be included in the model. If they are ignored the parameter estimates will generally be biased. The system model described by Eq. 58 is therefore extended again by the addition of a *noise model* and takes the form,

$$x_t = F^{(3)}(x_{t-1}, x_{t-2}; f_{t-1}; \zeta_{t-1}, \zeta_{t-2}) + \zeta_t \ . \tag{61}$$

This type of model is referred to as Nonlinear Auto-Regressive Moving-Average with eXogenous inputs (NARMAX). The NARMAX model was introduced in Leontaritis and Billings [40,41].

Finally, the term 'moving-average' requires some explanation. Generally, for a linear system a moving-average model for the noise process takes the form,

$$\zeta_t = e_t + c_1e_{t-1} + c_2e_{t-2} + \dots \ , \tag{62}$$

implying that the system noise is assumed to be the result of passing a zero-mean white noise sequence $\{e_t\}$ through a digital filter with coefficients $c_1, c_2, \dots$. The terminology comes from the literature of time series analysis. Equation 48 requires a generalization of this concept to the nonlinear case. This generalization is incorporated in the NARMAX model that takes the final general form,

$$x_t = F^{(n_y)}(x_{t-1}, \dots x_{t-n_y}; f_{t-1}, \dots f_{t-n_x}; e_{t-1} \dots e_{t-n_e}) + e_t \ . \tag{63}$$

In this form the noise sequence or *residual sequence* e_t is now zero-mean white noise. This allows the model to accommodate a wide class of possibly nonlinear noise terms.

The input and output variables f_t and x_t are usually physical quantities like force and displacement response, respectively. An interesting alternative approach to this was followed by Thouverez and Jezequel [47], who fitted a NARMAX model using modal coordinates.

Having obtained a NARMAX model for a system, the next stage in the identification procedure is to determine if the structure is correct and the parameter estimates are unbiased. It is important to know if the model has successfully captured the system dynamics so that it will provide good predictions of the system output for different input excitations, or if it has simply fitted the model to the data; in this case it will be of little use because it will only be applicable to one data set. Three basic tests of the validity of a model have been established by Billings et al. [48], and they are described below in increasing order of stringency. In the following, y_t denotes a measured output while $\hat{y}_t$ denotes an output value predicted by the model.

For the NARMAX representation of a system given by Eq. 63, the one-step-ahead prediction of x_t is made using measured values for all past inputs *and* outputs. Estimates of the residuals are obtained from the expression $\hat{e}_t = x_t - \hat{x}_t$, that is,

$$\hat{x}_t = F^{(n_p)}(x_{t-1},\ldots x_{t-n_x};f_{t-1},\ldots f_{t-n_f};\hat{e}_{t-1}\ldots\hat{e}_{t-n_e}) \quad . \tag{64}$$

The one-step-ahead series can then be compared to the measured outputs. Good agreement is clearly a necessary condition for model validity.

If the inputs, f_t, are the only measured quantities used to generate the model output, then Eq. 63 takes on the form

$$\hat{x}_t = F^{(n_p)}(\hat{x}_{t-1},\ldots\hat{x}_{t-n_x};f_{t-1},\ldots f_{t-n_f};0\ldots 0) \quad . \tag{65}$$

The zeroes are present because the prediction errors will not generally be available when one is using the model to predict output. In order to avoid a misleading transient at the start of the record for $\hat{x}$, the first n_x values of the measured output are used to start the recursion. As above, the estimated outputs must be compared with the measured outputs, with good agreement a necessary condition for accepting the model. It is clear that this test is stronger than the previous one; in fact the one-step-ahead predictions can be excellent in some cases when the model predicted output shows complete disagreement with the measured data.

These represent the most stringent of the validity checks [49]. The correlation function $\phi_{uv}(k)$ for two sequences of data u_t and v_t is defined by,

$$\phi_{uv} = E(u_t v_{t+k}) \approx \frac{1}{N-k}\sum_{t=1}^{N-k} u_t v_{t+k} \quad . \tag{66}$$

For a linear system the necessary conditions for model validity are,

$$\phi_{ee}(k) = \delta_{0k} \quad , \tag{67}$$

and,

$$\phi_{fe}(k) = 0 \ \ \forall k \quad . \tag{68}$$

The first of these conditions is true only if the residual sequence e_i is a white noise sequence. It is essentially a test of the adequacy of the noise model whose job it is to reduce the residuals to white noise. If the noise model is correct, the system parameters should be free from bias. The second of the conditions above states that the residual signal is uncorrelated with the input sequence f_i i.e. the model has completely captured the component of the measured output that is correlated with the input. Another way of stating this requirement is that the residuals should be unpredictable from the input.

In the case of a nonlinear system it is sometimes possible to satisfy the requirements above even if the model is invalid. An exhaustive test of the fitness of a nonlinear model requires the evaluation of three additional correlation functions [49]. The extra conditions are,

$$\phi_{e(e\bar{e})}(k) = 0 \quad \forall k \geq 0 \quad , \tag{69}$$

$$\phi_{f\bar{e}_e}(k) = 0 \ \ \forall k \ \text{, and} \tag{70}$$

$$\phi_{f\bar{e}_e^2}(k) = 0 \ \ \forall k \, . \tag{71}$$

The dash which accompanies $\bar{f}^2$ above indicates that the mean has been removed. Normalized estimates of all the correlation functions above are usually obtained so that confidence limits for a null result can be added.

6.11 Hilbert Transform

The Hilbert transform (HI) can be used to diagnose nonlinearity on the basis of measured FRF data. If the structure is assumed to respond in a linear manner in its undamaged state, then this diagnosis of nonlinearity can be used as a damage indicator. To begin, the map on a FRF $G(\omega)$ is,

$$H[G(\omega)] = \tilde{G}(\omega) = -\frac{1}{i\pi}\int_{-\infty}^{\infty} d\Omega \frac{G(\Omega)}{\Omega - \omega} \quad . \tag{72}$$

This mapping reduces to the identity on the FRFs of linear systems. Suppose $G(\omega)$ is decomposed so,

$$G(\omega) = G^{+}(\omega) + G^{-}(\omega) \quad , \tag{73}$$

where $G^{+}(\omega)$ (respectively $G^{-}(\omega)$) has poles only in the upper (respectively lower) half of the complex ω-plane. Then,

$$H[G^{\pm}(\omega)] = \pm G^{\pm}(\omega) \quad . \tag{74}$$

The HT distortion is,

$$\Delta G(\omega) = H[G(\omega)] - G(\omega) = -2G^{-}(\omega) \quad . \tag{75}$$

A major problem in using the Hilbert transform occurs when non-baseband or band-limited data are employed. The Hilbert transform can be recast in a slightly different form to that described above,

$$\Re\tilde{G}(\omega) = -\frac{2}{\pi}\int_0^{\infty} d\Omega \frac{\Im G(\Omega)\,\Omega}{\Omega^2 - \omega^2} \quad , \text{ and } \quad \Im\tilde{G}(\omega) = \frac{2\omega}{\pi}\int_0^{\infty} d\Omega \frac{\Re G(\Omega)}{\Omega^2 - \omega^2} \quad . \tag{76}$$

If zoomed data from $(\omega_{min}, \omega_{max})$ is measured, data is missing from the intervals $(0, \omega_{min})$ and (ω_{max}, ∞).

The problem is usually overcome by adding correction terms to the Hilbert transform [50]. An alternative approach to the Hilbert Transform exploits the pole-zero form of the FRF. A general FRF may be expanded into a rational polynomial representation,

$$G(\omega) = \frac{Q(\omega)}{P(\omega)} \quad . \tag{77}$$

Once the rational polynomial model, G_{RP}, is established, it can be converted into a pole-zero form,

$$G_{RP}(\omega) = \frac{\prod_{i=1}^{n_Q} (\omega - q_i)}{\prod_{i=1}^{n_P} (\omega - p_i)} \quad . \tag{78}$$

Long division and partial-fraction analysis produce the decomposition [51],

$$G_{RP}^{+}(\omega) = \sum_{i=1}^{N_+} \frac{C_i^{+}}{\omega - p_i^{-}} \qquad G_{RP}^{-}(\omega) = \sum_{i=1}^{N_-} \frac{C_i^{-}}{\omega - p_i^{-}} \quad . \tag{79}$$

Once this decomposition is established, the Hilbert transform follows.

Consider the Duffing oscillator,

$$\ddot{x} + 20\dot{x} + 10000x + 5\times 10^{9} x^{3} = F\sin(\omega t) \quad . \tag{80}$$

Data were generated from 0 to 38.4 Hz. The data were then truncated by removing data above and below the range 9.25-32.95 Hz.

Figure 51 shows the Hilbert transforms of the FRF calculated by the rational polynomial method on the truncated data and by a standard numerical method that used the full range of the data. An important thing to note in Fig. 51 is the departure from the normal circular appearance of the appropriately scaled Nyquist plot – this is the Hilbert transform distortion. The pole-zero decomposition method can also be used to compute analytical expressions for the Hilbert transform [52].

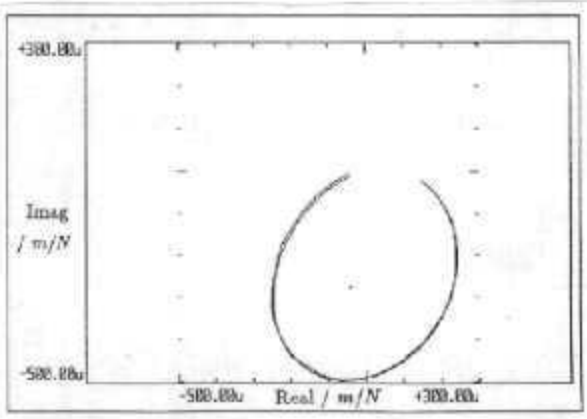

Figure 51. Comparison of Hilbert Transforms from rational polynomial approach and standard integral.

The Hilbert transform has also been used as a direct method of nonparametric identification. The FREEVIB and FORCEVIB approaches espoused in Feldman [53,54], can be used to construct the nonlinear damping or stiffness curves for a large class of nonlinear systems. The method works by extracting the instantaneous phase and frequency curves from experimental data. Alternative approaches have been constructed to yield the same information, in particular the Wigner-Ville approach [51], the method based on the Gabor transform in [55] and the wavelet approach of Staszewski [56]. All of these approaches except FORCEVIB extract the information from the free decay response of the systems.

6.12 Frequency Domain ARX Models

Frequency domain autoregressive exogenous (ARX) input models, based on discrete frequency models developed in [57] and applied in [58,59], take the form

$$X(K) = B(K)F(k) + \sum_{r,s\in\Re_1} A_{r,s}(k) \times f_{r,s}\left(X\left(\frac{p_r}{q_r}k\right), X\left(\frac{p_s}{q_s}k\right)\right) \quad , \tag{81}$$

where k, r, s, $(p_r/q_r)k$, and $(p_s/q_s)k$ are contained in the set of real integers, $\Re_1$, k is a simple frequency counter (i.e. $\omega = k\Delta\omega$), $X(k)$ is the response, $F(k)$ is the input, and $B(k)$ and $A_{r,s}(k)$ are complex frequency coefficients. The first term on the right-hand side of Eq. 81, the exogenous (X) component, accounts for the nominal linear dynamics and the second term, the auto-regressive (AR) component, accounts for the nonlinear frequency correlations. The rational number arguments, $(p_r/q_r)k$, are used to represent different harmonics of the excitation frequency. Equation 81 indicates that the harmonic response of a nonlinear system at each frequency is correlated with both the input and response at potentially all the harmonics of the input frequency. This multidimensional correlation is due to nonlinear feedback in the system.

The linear forms of the functions $f_{r,s}(.)$ indicate in what frequency ranges the nonlinear correlations exist, but may not describe all of the nonlinear dependencies of the response on the input. On the other hand, when the $f_{r,s}(.)$ are nonlinear functions of the harmonics of the spectrum, $X(k)$, then the model can more fully describe different types of nonlinear behavior. In summary, the $f_{r,s}(.)$ determine the degree to which the frequency domain ARX model is able to describe the behavior of the nonlinear system.

These models use frequency spectra of measured signals and spectra are easier to obtain from signals with broad frequency content; therefore, experimental application of this technique is suited to broad-band inputs (e.g., random).

Equation 81 can be written as,

$$X(k) = D\,p \quad , \tag{82}$$

where p are the exogenous and auto-regressive coefficients and D contains the input and the terms $f_{r,s}(.)$. The optimum set of ARX coefficients, the ones that minimize the sum of the squared error, $e(k)\,e(k)$, is given by the pseudo-inverse solution, $\hat{p}$, to the over-determined Eq. (82):

$$\hat{p} = D^{+} X(k) = (D^T D)^{-1} D^T X(k) \quad , \tag{83}$$

where D^{+} is the pseudo-inverse of D and D^T is the transpose.

The order of the nonlinear ARX model is determined by the number of auto-regressive (AR) terms that are included in the function $f_{r,s}(.)$, on one side of the frequency of interest, ω_k. Two forms of the ARX model are used here:

1st Order, Linear:

$$X(K) = B(K)F(k) + \sum_{j=-1\neq 0}^{1} A_j(k)X(k-j) \quad , \tag{84}$$

where only correlations with one frequency above and one frequency below the input frequency are considered.

1st Order, Nonlinear:

$$X(K) = B(K)F(k) + A_{-1}(k)Y^3\left(\frac{k}{3}\right) + A_1(k)Y^3(3k) \ , \tag{85}$$

where correlations with the cubic sub- and superharmonics are considered.

The changes in the auto-regressive coefficients (related to nonlinear behavior) can be used as indicators of damage, as damage often causes changes in the linear/nonlinear behavior of a structural system. A number of other indicators can be used that signify the onset and progression of damage in a system. The indicators used here are $A_j(k)$, the auto-regressive coefficients, and

$$1 - \left| A_{jj} \Big/ A_{jm} \right| \quad , \tag{86}$$

where *'d'* indicates damaged and *'un'* indicates undamaged. This function indicates the change in the nonlinear correlations compared to the undamaged case.

Damage was introduced in the suspension system of the automobile by loosening the bolt connecting the steering knuckle to the control arm, through a ball joint as shown in Fig. 52, from an initial torque of 400 *in-lb* to 250 *in-lb*, 100 *in-lb* and finally removing the bolt completely. Self-loosening is often a problem in bolted joints, especially in joints under cyclic transverse loading [60]. This type of damage has great importance in automotive applications because the fasteners generally represent the largest single cause of warranty claims faced by automobile manufacturers [61].

The models were applied using random input data with a Gaussian distribution for various input amplitudes ranging from 0.5 mm to 6.0 mm RMS displacements of the wheel pan (i.e., tire patch of the car).

Figure 52. Bolt damage location.

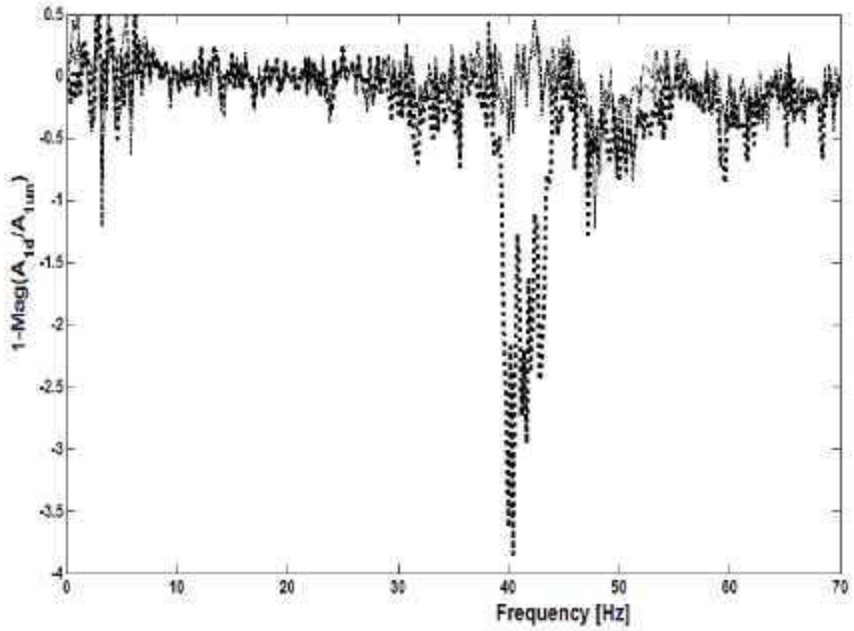

Figure 53. 1-Mag($A_{1d}(k)$/ $A_{1un}(k)$) for 1st order linear model (vertical direction); 250 lb-in torque (– – –), 100 lb-in torque (····) and no bolt (–.–.–).

First, the 1st order, linear model in Eq. 84 was applied to the data from points that had the damage location in their path, and the damage features were estimated. Figure 53 shows the estimated damage feature defined by Eq. 86 for the vertical motion data.

Figure 53 shows the feature defined by Eq. 86 for $A_1(k)$. Any nonzero value shows a change in the auto-regressive coefficients and is an indicator of change in nonlinearity. There is an obvious change in the 40–55 Hz range where the 100 lb-in torque case exhibits more nonlinear correlation than the other cases. It can be seen that the 250 lb-in torque case does not introduce any significant changes in the nonlinear correlations, and the undamaged case and the case with no bolt have very similar behavior. The coefficients $A_1(k)$ show the same trends.

Figure 54 shows a typical self-loosening sequence of a bolted joint caused by transverse cyclic loading [60]. The symbol P represents the clamping force, P_0 represents the initial clamping force or preload, and θ is the rotation angle of the nut against the bolt. This figure is relevant as the loading on the ball joint bolt in the suspension system of the vehicle under investigation is primarily transverse. Two distinct stages can be identified in the figure. During the first stage, there is very little relative motion between the nut and the bolt. The later stage is characterized by backing-off of the nut and rapid loosening of the clamping force with relative motion between the bolt and the joint. The second of the two loose bolt conditions (100 lb-in torque) that is simulated in the experiments belongs to the second stage. These stages of bolt loosening suggest that there is a critical value of the preload at the junction of the two stages seen in Fig. 54 where relative motion occurs at the joint and nonlinear correlations increase. The indicators discussed show that as the bolt is loosened, the nonlinearity in the path between x_2 and x_3 increases, due to the increased friction between the bolt and the ball joint caused by relative motion [62, 63], showed that

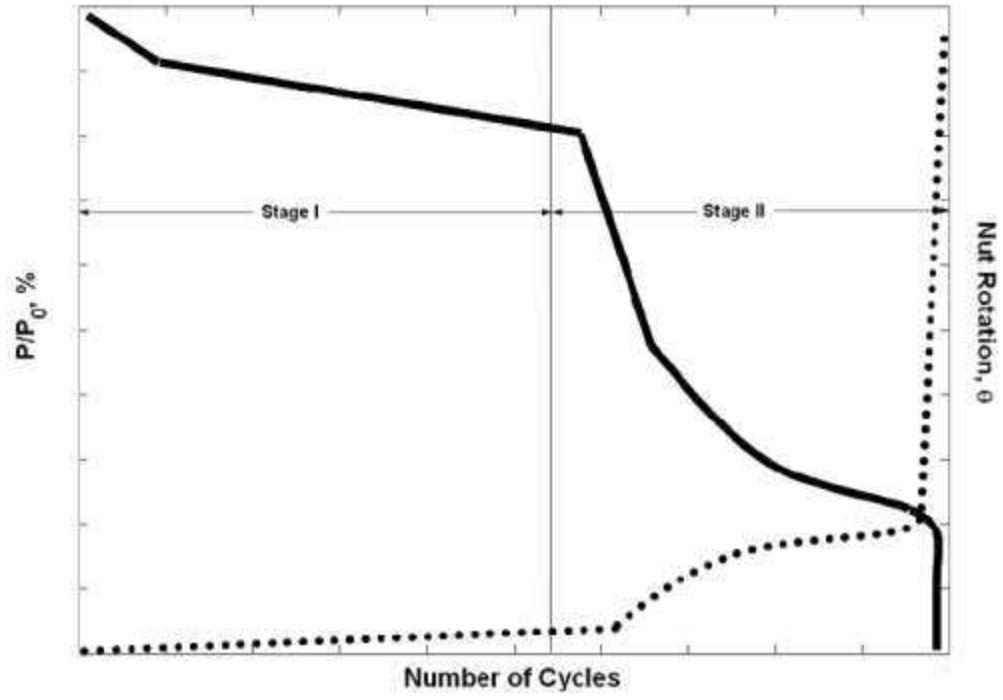

Figure 54. Self-loosening sequence of a bolted joint due to transverse cyclic loading; percentage preload loss (——), nut rotation (degrees) (····).

loosening and relative motion can occur in the presence of vibration). This friction force is governed by the equation for friction between surfaces in contact,

$$F_f = \mu N \quad , \tag{87}$$

where, μ is the coefficient of friction (static or kinetic) and N is the normal load between the joint threads. When the bolt is completely loosened or actually removed from the joint, the normal load goes to zero as there is no contact load and this source of friction force is no longer active. This condition results in the nonlinearity in the path between the two measurement locations returning to the original undamaged level.

The increase in friction caused by the relative motion between the bolt and the joined components results in an increase in the nonlinear frequency correlations seen in Figure 53. On the other hand, the removal of the source of increased friction (namely, the bolt) results in the nonlinear correlations returning to the undamaged levels. This behavior is similar to the behavior observed in the restoring forces. The intermediate damage cases have different characteristics from the undamaged case and the most severe case (no bolt) behaves similar to the undamaged case.

The lateral direction data exhibits the same pattern, but to a lesser extent than the vertical direction, as shown in Fig. 55, which is on the same scale as the vertical case. The longitudinal direction indicator (Fig. 56) shows the least change. In fact, it is almost insignificant compared to the other two cases. The cause of this result is that the bolt axis is in the longitudinal direction. Loosening of the bolt causes motion about the longitudinal axis (motion along the longitudinal axis is restricted because the bolt still applies some clamping force); hence, the vertical and lateral directions show greater changes in nonlinear correlations. So, the axis of the bolt can also be identified.

As explained earlier, the output only formulation of the nonlinear ARX models allows the damage to be located due to increasing sensitivity to changes in local dynamics. To verify this, the 1st order linear model was applied to data from locations that did not have the damage in their path. Figure 57 shows the estimated indicator defined by Eq. 86 for the data from points on the control arm and the sway bar. It is clear that there are no significant changes in the nonlinear correlations in the path between these two points. Hence, the damage has been located.

A 1st order nonlinear model was also applied to the data. A cubic form of the nonlinear model (Eq. (85)) was chosen as opposed to a quadratic form because the Coulomb friction nonlinearity changes with the loosening of the joint as discussed earlier. This discontinuous nonlinearity can be approximated with odd polynomial functions (i.e., x^3, x^5, etc.). In addition, symmetric nonlinearities result in odd response harmonics. It was observed that although there were significant quadratic harmonic correlations, they did not show any significant changes with damage because the damage primarily affects Coulomb friction. The same trends as before were observed (Fig. 58), with the nonlinear correlations increasing for the 100 lb-in case and decreasing when the bolt is removed. In fact, the 100 lb-in torque case shifts the nonlinear correlation with the third superharmonic (Fig. 58(b)) of the input excitation at about 7.5 Hz to 8 Hz. The auto-regressive coefficients also show an interesting result. The superharmonic frequency correlations are much

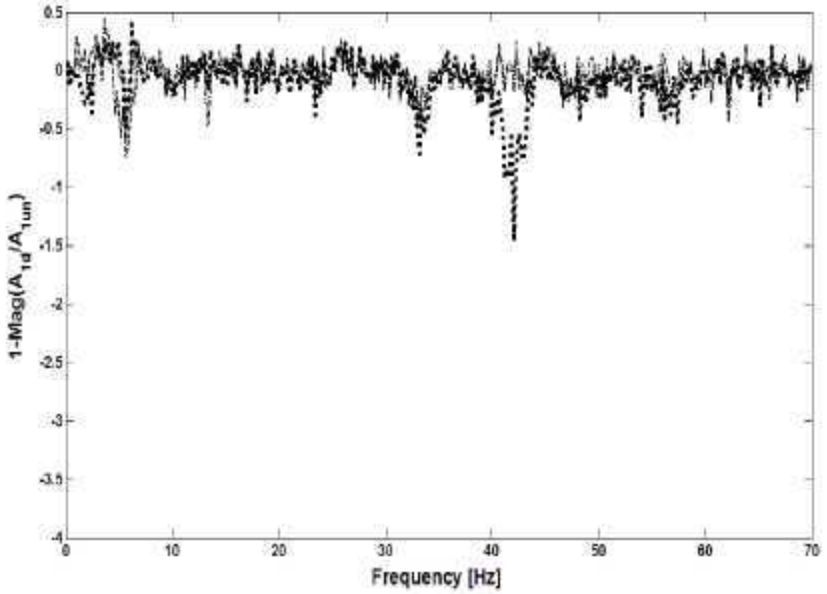

Figure 55. 1-Mag(A1d(k)/ A1un(k)) for 1st order linear model (lateral direction); 250 lb-in torque (– – –), 100 lb-in torque (····) and no bolt (–.–.–).

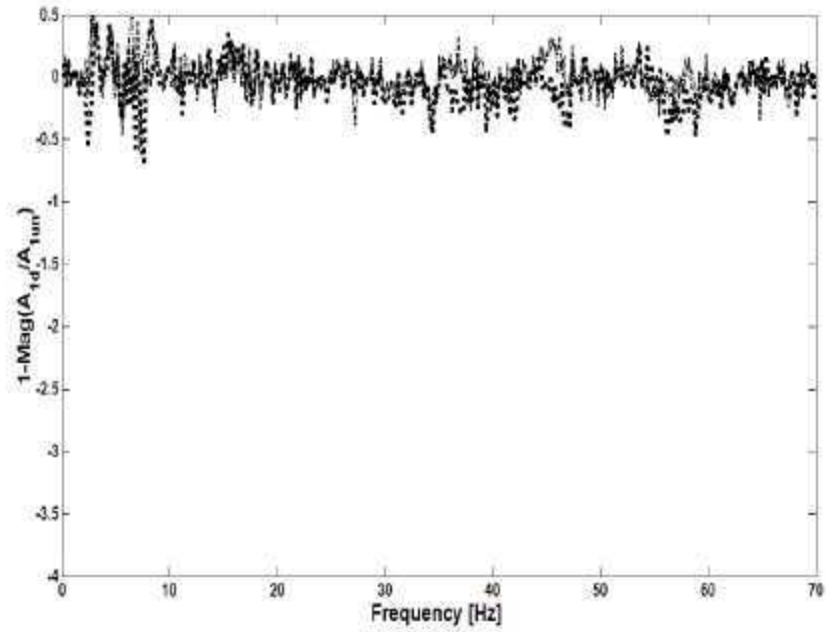

Figure 56. 1-Mag($A_{1d}(k)$/ $A_{1un}(k)$) for 1st order linear model (longitudinal direction); 250 lb-in torque (– – –), 100 lb-in torque (····) and no bolt (–.–.–).

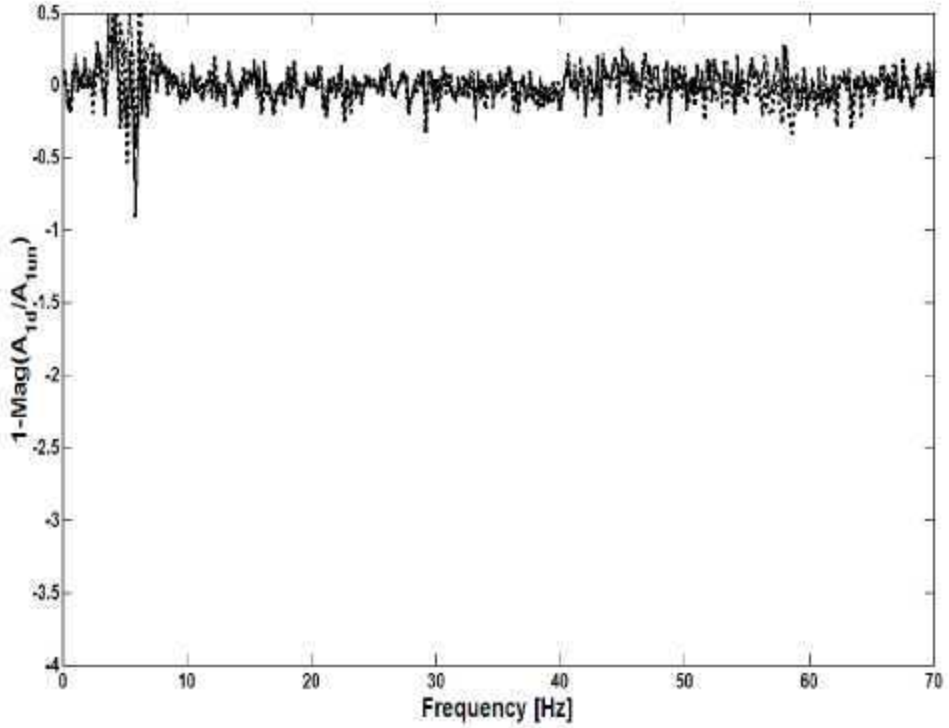

Figure 57. 1-Mag($A_{1d}(k)$/ $A_{1un}(k)$) for 1st order linear model applied to points with no damage in their path (vertical direction); 250 lb-in torque (– – –), 100 lb-in torque (····) and no bolt (–.–.–).

stronger than the sub-harmonic correlations. This result suggests that the nonlinear feedback caused by the third superharmonic of the forced response of the system (which is symptomatic of nonlinear behavior) is much greater than the subharmonic. In the nonlinear model it is assumed that the nonlinearity is cubic in nature, hence, if the forcing function is harmonic (e.g., cos(ωt)) the cube of the function gives frequency components at one and three times the forcing frequency.

$$\left(\cos(\omega t)\right)^3 = \frac{3}{4}\cos(\omega t) + \frac{1}{4}\cos(3\omega t) \tag{88}$$

Equation (88) shows that there are no submultiple components. The superharmonic correlations interact with the forced response components at other excitation frequencies to produce sub-harmonic correlations via frequency combinations. The resulting subharmonic correlations are weaker in this case. The response of the system is primarily forced because the data was collected for a broad-band input after the system had reached steady-state., i.e. the system transients had died out. A more detailed discussion of higher order spectra can be found in [64].

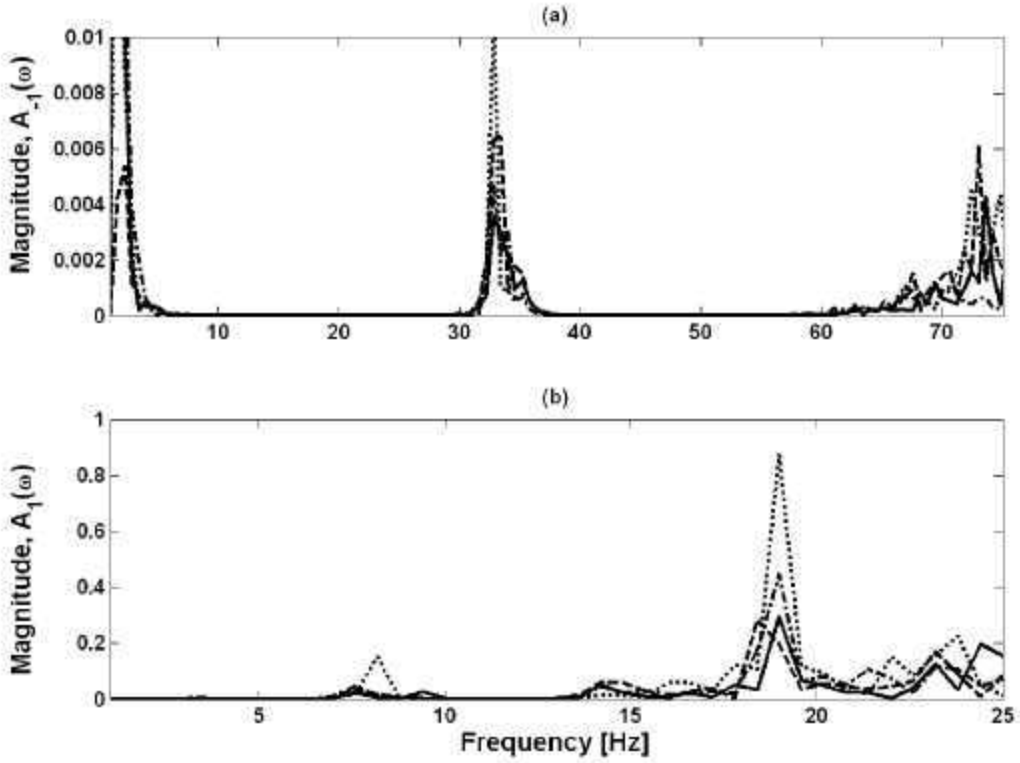

Figure 58. Auto-regressive coefficients $A_{-1}(k)$ (sub-harmonic) and $A_1(k)$ (superharmonic) for 1st order nonlinear model; Coefficients for undamaged case, 400 lb-in (——), and damaged cases, 250 lb-in (– – –), 100 lb-in (····) and no bolt (–.–.–).

6.13 Higher Order Spectra

The bispectrum, also called the third-order spectrum, is the first of the so-called higher-order spectra, which are used to analyze non-linear systems or linear systems subjected to non-Gaussian inputs. The bispectrum decomposes the skewness or third-order moment of a signal and is useful for studying asymmetric nonlinearities. These are nonlinear stiffness or damping characteristics that contain even-order polynomials in their mathematical descriptions. The bispectrum [65] can be defined as,

$$E_{xxx}(f_1, f_2) = X(f_1)^* X(f_2)^* X(f_1 + f_2) \quad , \tag{89}$$

where E is the mathematical expectation operator, $X(\ )$ are the Fourier transform of the signal and * indicated the complex conjugate.Unlike the power spectrum, which presents the contribution of each frequency component individually, the bispectrum is a function of two distinct frequencies f_1 and f_2 and analyzes the interactions between the frequencies at f_1, f_2 and f_1+f_2. The bispectrum of a signal composed of two sinusoids of different

frequencies, p_1 and p_2, will contain eight triple products. If one frequency is twice the other, this will lead to a non-zero bispectrum at (p_1,p_1)in the (f_1,f_2) plane. Thus the bispectra of signals from systems with symmetric nonlinearites (which lead to quadratic frequency coupling) will be non-zero and will change as the nonlinearity changes. The magnitude of the bispectrum is utilized in the example below to illustrate damage detection based on this indicator.

A MTS® 810 Material Test System was used to perform tension-tension fatigue tests on the front stabilizer bar link of an automobile. A picture of the experimental setup is shown in Fig. 59. A fixture was designed to hold the link in the grips of the fatigue machine and two single axis accelerometers with nominal sensitivity of 1000 mV/g were attached to the two ends of the link to measure axial acceleration as shown in Fig. 60. An initial tensile load was applied to the link and then the link was subjected to a cyclic load at 5 Hz, which can be thought of as a durability cycle. Sine sweep and random input characterization tests were run intermittently to estimate and track the nonlinear load and damage indicators. The test parameters are given in Table 3.

Figure 59. Fatigue test setup.

Figure 60. Fixture for placing link under test in fatigue machine grips. Accelerometers attached to the ends of stabilizer bar link.

Table 3. Parameters for Sine Sweep and Random Inputs; Link 1

Input Type	Amplitude (mm)	Frequency Content (Hz)	Sampling Frequency (Hz)	Test Length (sec)
Sine Sweep	0.05	0-15	2000	100
Random	0.05 rms	0-30	2000	100

The front stabilizer bar link was subjected to an initial tensile load of 5500 N. Blocks of 2500 cycles of a 0.10-mm amplitude cyclic load at a frequency of 5 Hz were used to fatigue test the links. This displacement corresponded to a cyclic load range of about 8000 N. The cyclic loading led to the appearance of a circumferential crack at the lower weld location (input side) as shown in Fig. 61. Sine sweep and random tests were conducted between the cyclic loading blocks and the load and damage indicators were estimated.

The bispectrum of the response acceleration of the top end of the link was generated as the circumferential fatigue crack appeared and grew to failure. Figure 62 shows the magnitude of the bispectrum for the undamaged case. It is large at the lower frequencies, which can be anticipated from the power spectrum of the acceleration signal in Fig. 63. Figure 64 shows the progressive change in the magnitude of the bispectrum as the crack appears and progresses in the link. The lighter portions of the plots show areas where there has been an increase in nonlinear coupling. As the crack appears and grows, peaks

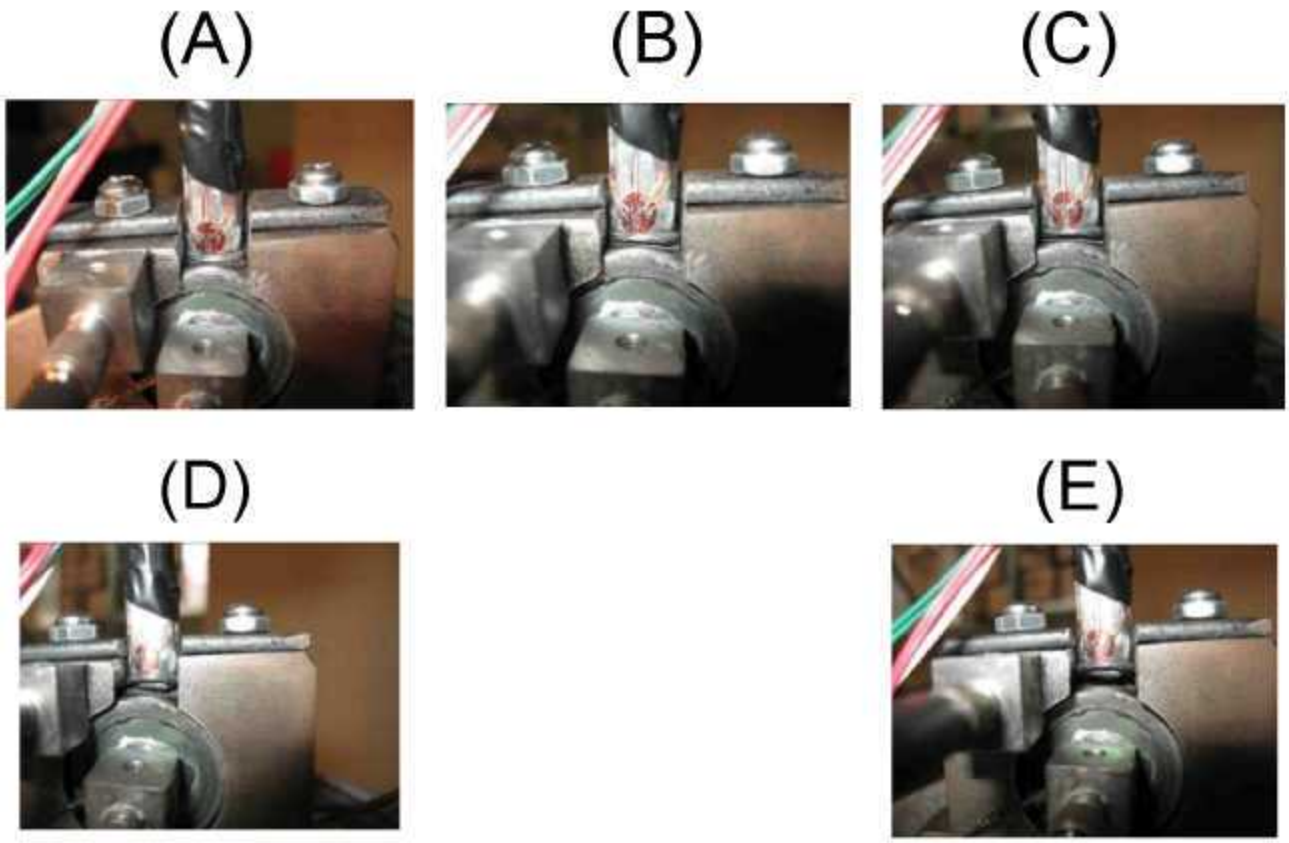

Figure 61. Appearance and progressive growth of circumferential crack to failure in stabilizer bar link under tension-tension fatigue loading; (a) – (e).

suggesting localization of energy occurs signifying increased quadratic coupling in frequency. It is apparent that the nonlinear coupling increases continually as the crack progresses. Finally, just before failure, there is significant nonlinear coupling around 10 Hz. This coupling is evident from the large peaks around 10 Hz along the two frequency axes in Fig. 64(e). The peaks signify strong quadratic coupling between response components around 10 Hz and 1.25 Hz, respectively. The spread of the peaks suggests that the coupling is actually in a band around the afore-mentioned frequencies. The conclusion is that as the crack appears and grows there is increased quadratic coupling signified by localized concentration of energy in the bispectra and the approach of failure is signified by the appearance of large coupling around 10 Hz. Hence, the bispectra qualitatively captures the increase in nonlinear frequency correlations with damage.

In order to quantify the nonlinear changes an index was developed by summing the magnitude of the bispectra in the higher frequency range (above 5 Hz), which shows clear nonlinear change (Fig. 64). The index is shown in Fig. 65. There is a clear increasing trend in nonlinear content as the crack grows with a sharp jump as failure approaches. See Reference [66] for a more detailed description of the bispectrum and its application to damage detection in systems that exhibit nonlinear response.

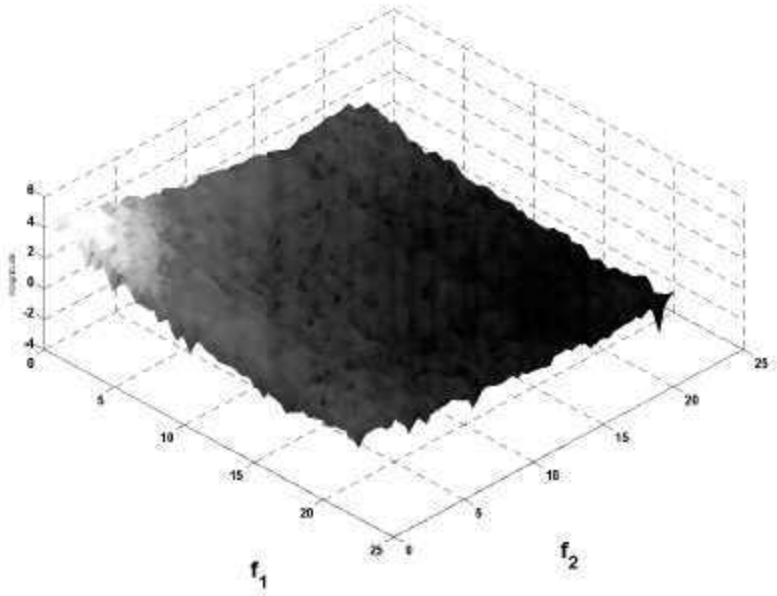

Figure 62. Bispectrum of undamaged acceleration response of stabilizer link top; lighter portions have higher magnitude.

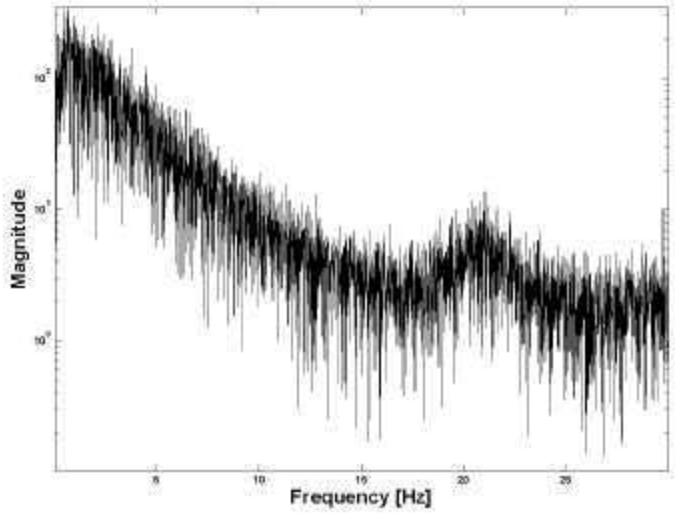

Figure 63. Power spectrum of undamaged acceleration response of stabilizer link top.

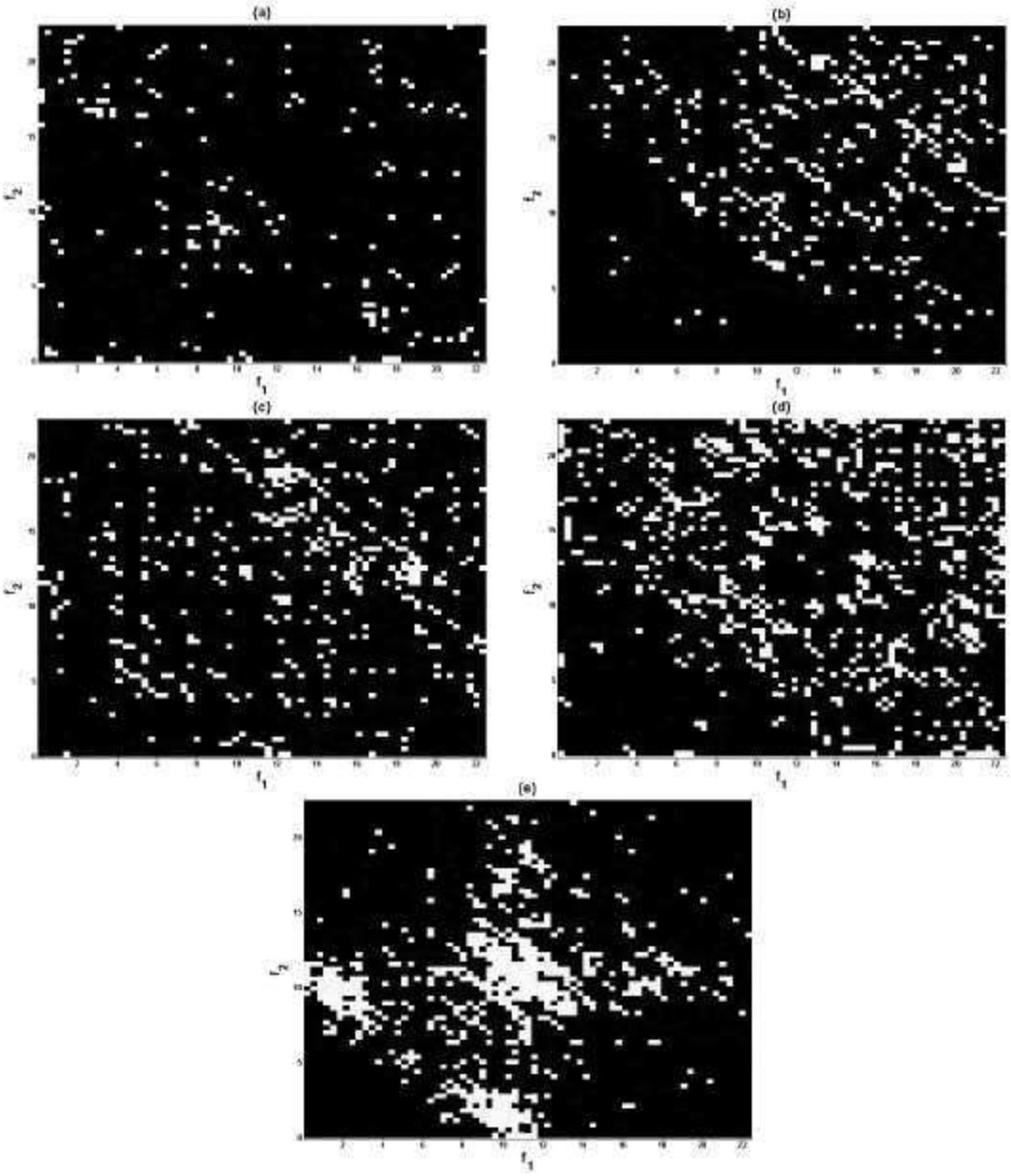

Figure 64. Change in magnitude of bispectrum of stabilizer bar link response with the progress of fatigue crack: (a) initial crack, (b) progression 1, (c) progression 2, (d) progression 3, (e) just before failure.

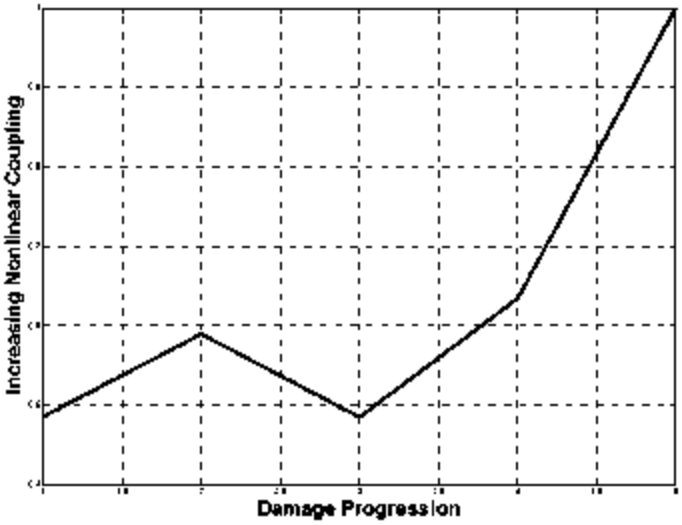

Figure 65. Index based on magnitude of response bispectrum showing progressive increase in nonlinear frequency coupling with growth of fatigue crack.

6.14 Nonlinear Acoustics Methods

Other approaches that capture the nonlinearity caused by structural damage are nonlinear acoustic methods.Damaged materials exhibit a nonlinear response because of wave distortion caused by the irregularities of the damage. This nonlinear response can manifest itself as the generation of harmonics or sum and difference (modulated) frequencies. The premise of the method is the same as those described in the previous sections, but the frequency ranges used in these nonlinear acoustics methods span up to tens of MHz, typically used in the wave propagation regime.

Typical signal processing methods employed by these techniques are the "harmonic distortion" and "frequency modulation" methods. Krohn et al. [67] described the phenomena of generating higher harmonics caused by nonlinear damage. In brief, the tangential movement of a crack causes hysteretic energy dissipation, resulting in distortion of sinusoidal waves in a symmetrical manner. This dissipation will produce strong odd harmonics. On the other hand, upon the application of a perpendicular load, the measured frequency will have components of a sinusoidal part (excitation) and a square signal with a time-dependent load duty cycle (side clapping). This clapping nonlinearity, resulting in a $(\sin \omega)/\omega$ decay, generates even harmonics. These types of nonlinearity are highly localized in the vicinity of the defects, so that the imaging methods utilizing a scanning laser vibro-meter can easily identify the location of damage [67]. As described in the previous section, the harmonic distortion methods have been widely used in structural damage identification, in particular, in the rotating machinery.

Another interesting approach based on nonlinear acoustics is the "frequency modulation" method described in Donskoy and Sutin [68], Zaitsev et al. [69], and Ballad et al. [70]. The idea is to instrument a structure, for example, with two sinusoidal excitation sources of the frequencies of f_h and f_l. When the response time history is converted to a spectrum, if the system is linear, the spectrum contains a single line at f_h as shown in Fig. 66(a). If the system is nonlinear, the nonlinearity will result in the appearance of sidebands at the frequencies $f_h \pm f_l$ as shown in Fig. 66(b). The appearance of the sidebands are the indicator of nonlinearity and, hence, damage. An index of damage extent can then be formed by recording the height of the sidebands [71] or the spread of the sidebands [72]. In order to efficiently excite the nonlinearity, the low-frequency excitation, f_l, can come from ambient excitation, operation frequency such as pumps, or an impact excitation. Some researchers utilize the two different types of actuators, piezoelectric stack and patch actuators, for low and high frequency excitations, respectively [72]. The frequency modulation method has its application in fatigue damage accumulation monitoring [73, 74, 75], and an excellent review of this methods can be found in Donskoy [76].

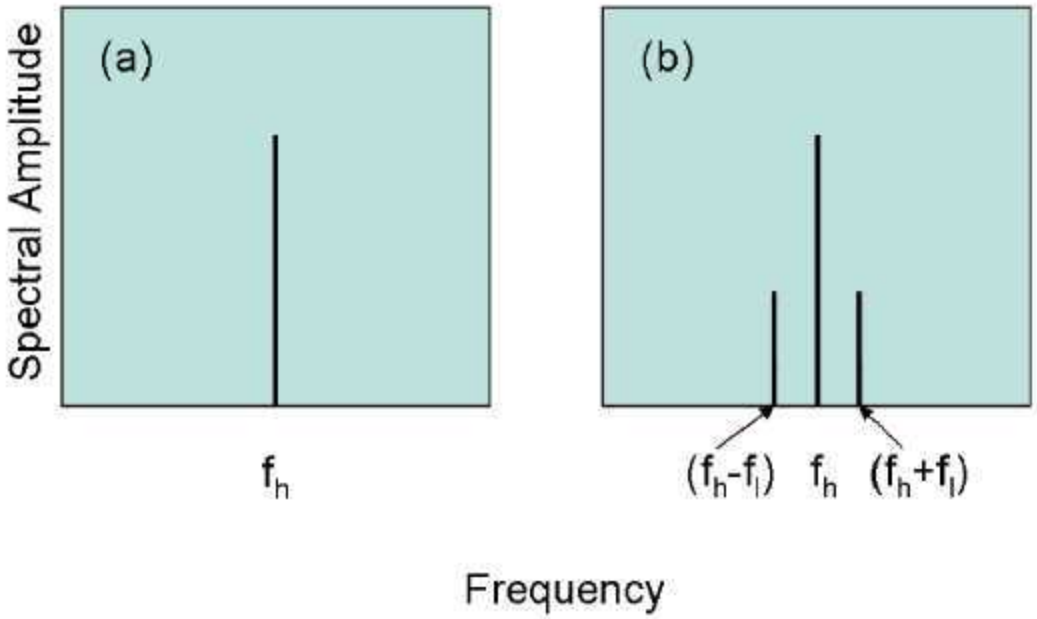

Figure 66. (a) Response to excitation at high frequency f_h, (b) Response to simultaneous excitations at high f_h, and low f_l, frequencies.

Although the nonlinear acoustic methods are much more sensitive to small defects than linear-based methods, there are some limitations. For instance, the level of the "background" nonlinearities, such as those caused by material nonlinearity, joints, or structural contacts, must be well understood and quantified in order to distinguish them from the nonlinearities caused by structural damage. The calibration of modulated frequencies is also important to achieve the repeatable measurement as it is obviously dependent on the magnitude of the low-frequency excitation. Furthermore, most modern instrumentation generate the harmonics, therefore, the method requires higher-cost data acquisition equipment. These issues must be addressed before nonlinear acoustics methods can be reliably used in industrial practice.

7. APPLICATIONS OF NONLINEAR DYNAMICS SYSTEMS THEORY

The main concept of this report is that, if a given type of damage converts a linear system into a nonlinear system, then any observed manifestations of nonlinearity serve to indicate that damage is present. This section discusses one of the most dramatic manifestations of nonlinearity, namely chaos. It is well-known that, under certain conditions of forcing, many nonlinear systems can be driven into a chaotic regime. Here a chaotic regime is defined as one where there is sensitive dependence on initial conditions. Over the years, the dynamical systems community has derived many indicators of chaotic behavior like fractal attractor dimensions and Lyapunov exponents [77]. As only nonlinear systems can behave chaotically, any feature that detects chaos, necessarily detects nonlinearity and might potentially be put to service in detecting damage. The aim of this section is to illustrate the use of such features. It will be shown that these features are suboptimal for damage detection as they do not produce an indicator that monotonically increases with the damage extent. The latter part of the section illustrates a feature motivated by chaotic dynamics that does have this desired property.

Consider a simply supported beam. In its undamaged state an assumption that the beam can be modeled as a linear system is quite adequate, but consider what happens when a crack is introduced halfway along its length, as shown in Fig. 67.

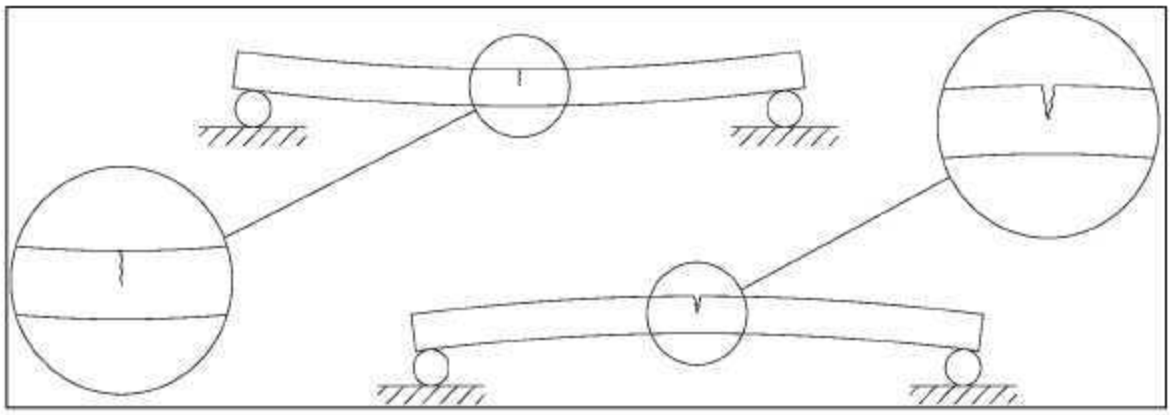

Figure 67. A cracked beam under positive and negative deflections.

When the beam sags, the effects of the crack are negligible because the two faces of the crack come together and the beam behaves as though the crack was not there. When the beam hogs however, the presence of the damage must affect the beam because the crack opens and the effective cross-sectional area of the beam is reduced. Under these circumstances, an appropriate model of the beam would perhaps be that shown in Fig. 68, which has the general equation of motion

$$m\ddot{x} + c\dot{x} + kx = f(t) \quad , \tag{90}$$

Where

$$\kappa = \begin{cases} k & x < 0 \\ \alpha k & x \geq 0 \end{cases} \quad . \tag{91}$$

When the displacement x of the mass m is positive, the stiffness of the system κ is reduced by a factor α. The two stiffnesses produce an overall restoring force F_κ that is bilinear. This type of model can be applied to a number of mechanical systems in which moving parts make contact with each other at intermittent points in time.

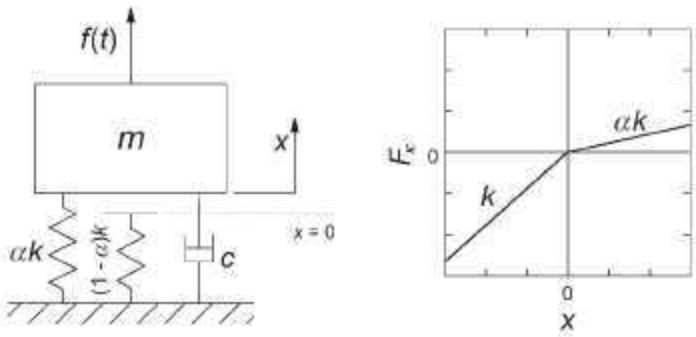

Figure 68. Single Degree-of-Freedom bilinear system.

Various studies both theoretical and experimental [77, 78, 79, 80, 81, 82, 83] have shown that bilinear oscillators are capable of a variety of responses to a sinusoidal force. As well as regular harmonic motions, the system can display sub-harmonic motions and in certain circumstances the system can also exhibit chaotic behavior. This response has even been evident in the experimental studies, for example [78].

The question of importance for damage detection purposes is whether the induced bilinearity from a crack can be used to signify the presence of the fault. More specifically, can one or more features be extracted from the recorded dynamics that detect the crack with a degree of statistical confidence? Further, can a feature be obtained that shows the *severity* of the damage. One might argue that the feature should at least grow monotonically with the damage extent. Examples of features proposed in the past have been the correlation dimension of the attractor (from embedding) and the highest Lyapunov exponent. The use of such features is discussed in the next section.

7.1 Modeling a Cracked Beam as a Bilinear System

The single-degree-of-freedom system shown in Fig. 68 was used to model a simply-supported aluminum beam, 0.8-m long, 50-mm wide and 10-mm thick. Different levels of damage were given to the system by varying the value of the stiffness ratio coefficient α. Putting the bilinear system into the context of a cracked beam made it possible to explore the types of behavior that could be expected from such a beam as the damage level was increased.

A density of $\rho = 2700\,\mathrm{kgm}^{-3}$ and a Young's modulus of E= 70 GPa were assumed as material properties. Using elementary theory of elasticity the undamaged stiffness of the beam was found to be $\kappa = k = 27346\,\mathrm{Nm}^{-1}$. With a mass of $m = 0.6$ kg, the undamaged beam had a natural frequency of $\omega_n = 214\,\mathrm{rad/s}$, which corresponds to 34Hz. A damping constant of $c = 2.6\,\mathrm{Nsm}^{-1}$ was used, which corresponds to 1% of critical damping. A sinusoidal force with an amplitude of 10N was applied to the system so that $f(t) = 10\sin(\omega t)$. As the system is homogeneous the amplitude of the force merely scales the output of the system.

A numerical algorithm based on a fourth-order Runge-Kutta integration scheme was used to integrate the equation of motion and calculate the dynamics response of the beam. The key to the success of the algorithm was its ability to detect each point in time when the displacement of the system crossed $x = 0$. This capability means that the algorithm knows exactly when to change the value of κ.

Examples of the phase portraits obtained from the algorithm, after transient motions have decayed, are given in Fig. 69. They show the displacement-velocity trajectories of the system in response to three different forcing frequencies, but for the same value of the stiffness reduction factor, $\alpha = 0.6$. In each case the system has settled onto a periodic motion or attractor.

Forcing the system at the undamaged natural frequency, $\omega = 214\,\mathrm{rad/s}$, resulted in a harmonic motion, but for $\omega = 384\,\mathrm{rad/s}$ and $\omega = 561\,\mathrm{rad/s}$ subharmonic motions of period 2 and period 3 (i.e. twice and three times the forcing frequency) are found. This subharmonic generation manifests itself in the time-series as a distortion from the sinusoidal form which would be expected from a linear system.

As the forcing frequency is increased from $\omega = 214\,\mathrm{rad/s}$ to $\omega = 384\,\mathrm{rad/s}$, at some point there must be a qualitative change in the topology of the attractor for the period of the motion to change. The point at which such a change occurs is a *bifurcation*. Bifurcations only occur in nonlinear systems.

If the response of the system is sampled at the forcing frequency and the resulting points are plotted in the phase plane, one obtains the *Poincare map* of the response. A moment's thought shows that the map associated with a period 1 motion will be a single point, a period 2 motion will produce two points, etc. If a system is chaotic, the Poincare map is usually much more complicated than this, and considered as a point set in the phase plane will actually have a fractal (non-integer) dimension.This point set can loosely be called the *chaotic attractor* of the system. A *bifurcation diagram* is obtained by varying a system parameter and plotting against this, a one-dimensional projection of the Poincare map associated with each value of the parameter. The bifurcation diagram in Fig. 70, is obtained by varying the forcing frequency and plotting the displacement values from the associated Poincare maps.

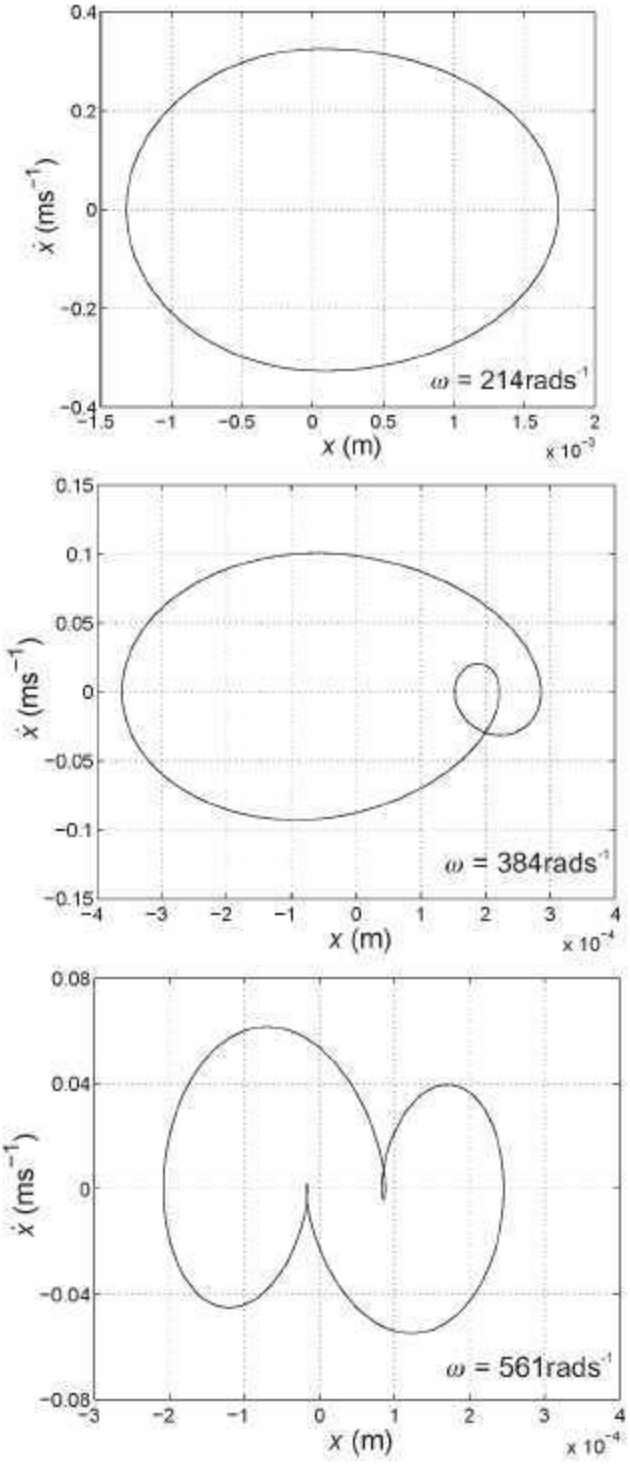

Figure 69. Phase portraits of periodic motions for α = 0.6.

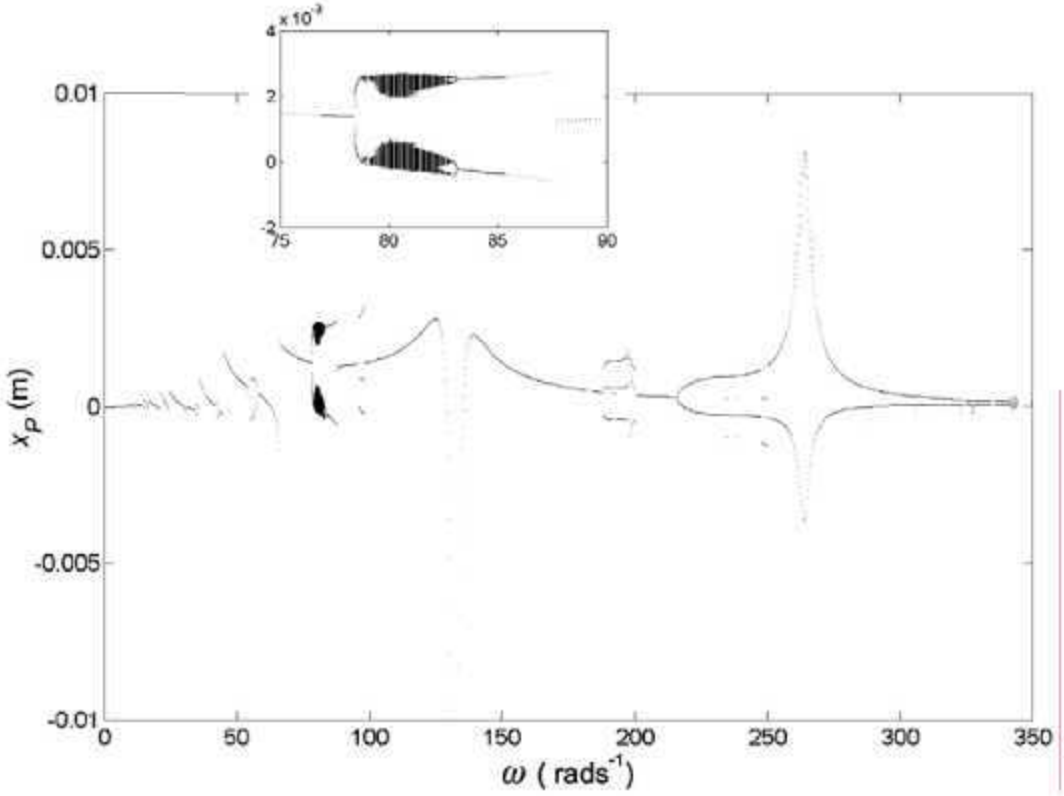

Figure 70. Bifurcation diagram for a = 0.2.

The diagram in Fig. 70 is easy to read. If there is only one point on a given vertical line (value of frequency) the system exhibits a period 1 motion at that frequency. If there are n points at a given frequency this is characteristic of a period n motion.

Figure 70 is the bifurcation diagram for $\alpha = 0.2$. There are many regions of sub-harmonic motion. From $\omega \approx 79$ rad/s to $\omega \approx 83$ rad/s there is a region where the period appears to be very high. In fact, it is infinite and this is characteristic of chaotic motions that do not repeat even if the excitation is periodic. All the period n motions are indicators of nonlinearity. However, only in the limited chaotic regions will features like chaotic attractor dimension show nontrivial behavior (i.e. fractional dimension).

The simulations show the limitations of parameters like attractor dimension for the detection and quantification of damage. Certainly if the undamaged system is linear, the presence of a fractional attractor dimension would indicate nonlinearity and thus damage. However, such parameters will not be reliable. The simulations show that chaotic response is not present at all frequencies. Similar runs have shown that fixing the frequency and varying the stiffness ratio produces the same pattern of movement between subharmonic responses with isolated regions of chaos. This result means that dimension parameters will not vary montonically with the damage extent. The same will be true of any detectors of chaos such as a Lyapunov exponent. The next section investigates a recently proposed feature motivated by chaos theory that does appear to have the required monotonic property.

7.2 Chaotic Interrogation of a Damaged Beam

The use of a chaotic signal to excite a dynamical system presents some interesting features. The structure can be thought of as a filter acting on the signal. Any changes to the system resulting from damage alter the way in which the signal is filtered. The benefits of using a chaotic excitation of the system relate to the way attractor stability (in the Lyapunov sense) and geometry (dimension) interact, and this is discussed in detail in [84].

7.2.1 Local Attractor Variance

The effects of the damage are evident when the attractors of the input and the output are compared. The average local attractor variance ratio (ALAVR) is a simple means of achieving this comparison. It is designed to analyze the geometry changes at a local level.

In many real situations it is only (practically) possible to obtain a single phase-space variable from a system. This limitation is not a problem because this variable will still be affected by all of the relevant dynamical variables, and will therefore contain a relatively complete historical record of the system's dynamics. The ALAVR can be calculated as long as a time series of the input signal $f(n)$ and a time series of one output variable $x(n)$ can be obtained. To achieve a correspondence between the input and output attractors, the two time series must be obtained over the same period of time and using the same sampling frequency such that,

$$f(n) = (f(1), f(2), f(3), \ldots, f(N)) \text{ , and} \tag{92}$$

$$x(n) = (x(1), x(2), x(3), \ldots x(N)) \text{ .} \tag{93}$$

From these time series input and output attractors can be reconstructed by projecting the time series into a pseudo-phase space. In each dimension of this space the time series are delayed by some number of time steps τ and a geometric structure is created that recaptures the dynamics of the system. The reconstructed attractor is usually topologically equivalent to the actual attractor of the system. The dimensionality of the pseudo-phase space required to fully capture the dynamics is not known in advance, but as the ALAVR is designed to merely detect simple geometric changes, a two-dimensional space is adequate. The coordinates of the two reconstructed attractors are then

$$\underline{f}(n) = (f(n), f(n+\tau)) \text{ ,} \tag{94}$$

$$\underline{x}(n) = (x(n), x(n+\tau)) \text{ ,} \tag{95}$$

$$\text{for } n = 1,2,3,\ldots,N-\tau \text{ .}$$

The local geometry of the attractors is analyzed by first selecting, at random, a point on the reconstructed forcing attractor $\underline{f}(i)$. The Euclidean distance from this point to the other points on the attractor is calculated and the coordinates of the points nearest to $\underline{f}(i)$

are extracted from the attractor to form a subset of points $\underline{f}(i,j)$, (where $j = 1,2,3,\ldots N_j$) that express the local geometry of the forcing attractor around the chosen point. There are some subtleties to this process that are explained in [84].

The points with the same indices *i* and *j* are then extracted from the response attractor to give another subset of points $\underline{x}(i,j)$ that contains the local geometry of the corresponding region on the response attractor.

The variance of the coordinates in each set of points $\sigma^2_{\underline{f}(i,j)}$ and $\sigma^2_{\underline{g}(i,j)}$ is used to describe the geometry of each set of points, which means the ratio of the two variances *R(i)* can be used to describe the degree to which the local geometry of the input attractor has been altered by the system,

$$R(i) = \frac{\sigma^2_{\underline{f}(i,j)}}{\sigma^2_{\underline{g}(i,j)}} \quad . \tag{96}$$

This process is then repeated for a total of N_i random points and the average local attractor variance ratio (ALAVR) $\overline{R}$ is found

$$\overline{R} = \frac{1}{N_i}\sum_{i=1}^{N_i} R(i) \quad . \tag{97}$$

The ALAVR metric discussed above is one of several features that have been presented recently as damage indicators. Nichols, Todd, and colleagues have constructed attractor-based auto- and cross-prediction error metrics for a number of bolted joint applications [85,86,87,88,89].The concept here is that a reconstructed attractor may be used to auto-predict itself (or cross-predict another simultaneously sampled attractor) in a baseline condition, and subsequently this prediction will fail as the system changes due to damage.

The fundamental prediction error model is as follows. First, a set of *F* random fiducial points is chosen from the baseline attractor, $X_1(n)$, and a corresponding set of points is obtained from the comparison attractor, $X_2(n)$, correlated in some way, typically either temporally or geometrically (from the state space reconstruction), to the fiducial points from the baseline attractor. Next, a set of *P* nearest neighbors to each point is found for both attractors. These neighbor points will be separated by at least *h* points in time from the fiducial point using a Theiler window [90]; in other words, nearest neighbors to a fiducial point should not be highly correlated temporally to the fiducial point on that individual attractor. This verified that the neighbors are geometrically correlated to the flow dynamics and insensitive to sampling rate. The size of the set of fiducial points, *F*, depends on the total number of points on the attractor and should be chosen to produce invariant statistics (completely 'span' the attractor). The number of nearest neighbors for a given fiducial point, *P*, will also depend on the dynamics and inherent noise of the system. Classic choices for *F* and *P* are *N/10* and *N/1000* respectively, where *N* is the number of points on the attractor [91]. The Theiler window, *h*, is typically a function of the delay choice with the only stipulation that it be larger than the delay *T* chosen to reconstruct the attractors.

After the fiducial points and neighborhoods have been selected, they are time evolved by s time increments, known as the prediction horizon Some simple statistic (typically, the mean location) of the neighborhood is computed (or, the fiducial point iself) so that we have set of means from a reference attractor ϕ_1 and a similar set from a test attractor ϕ_2 Finally, a comparison is drawn between the sets by forming the Euclidean error distance for each fiducial point n

$$\varepsilon = \left\| \phi_2(n+s) - \phi_1(n+s) \right\| \tag{98}$$

This error metric may then be averaged over the whole data set to generate an average prediction error that relates how one attractor "predicts" another [85, 86, 87, 88, 89], or local statistics may be computed [92] Regardless of how the specific error metric is formed, the feature can be normalized by either a representation of the geometrical size of the attractor or by an undamaged reference error value in attempt to establish a quantitative sense of the prediction error values Moniz et al [93] used this general concept of correlation and predictability to build a continuity statistic to detect changes in an electrical circuit that was used to simulate a lumped mass structural system

Other researchers have focused on attractor-based measures derived straight from the local probability structure of the data Bogdan and Yin [94] computed estimates of the local probability density and then used the resulting distribution on the attractor as the damage-indicating feature for a nonlinear aeroelastic plate subject to stiffness degradation Trendafilova looked at the local probability structure of data in detecting static load shifts in a reinforced concrete plate [95] Hively and Protopopescu used a phase space measure of probability to distinguish between healthy and damaged motor-driven systems [96]

Finally, some attention has been given to using Lyapunov Exponents (LEs) as a damage-sensitive feature A system's LEs capture the rate at which trajectories in phase space diverge or converge in each of the phase space directions Global LEs have been used in [97] and [98] to detect backlash in robot joints and in gears, respectively A more complete discussion on the use of LEs in health monitoring, including a discussion of local LE measures, may be found in [92]

7.2.2 Detection of Damage in a Cantilever Beam Using the Local Attractor Variance

The technique just described was used to detect damage in a simulated cantilever beam An eight-degree-of-freedom model was used and a crack at the root of the beam was simulated by placing a bilinear stiffness between the wall and the mass element adjacent to it, as shown in Fig 71 The equation of motion of this system is

$$[m]\{\ddot{x}\} + [c]\{\dot{x}\} + [\kappa]\{x\} = \{B\} f(t) \ , \tag{99}$$

where $[m]$, $[c]$ and $[\kappa]$ are the respective mass, damping and stiffness matrices formed from the elements in the model, with

$$\kappa_{11} = \begin{cases} k & x_1 < 0 \\ \alpha k & x_1 \geq 0 \end{cases} \quad . \tag{100}$$

The vector $\{B\}$ simply selects where the force $f(t)$ is applied to the system, which in this case is the end mass.

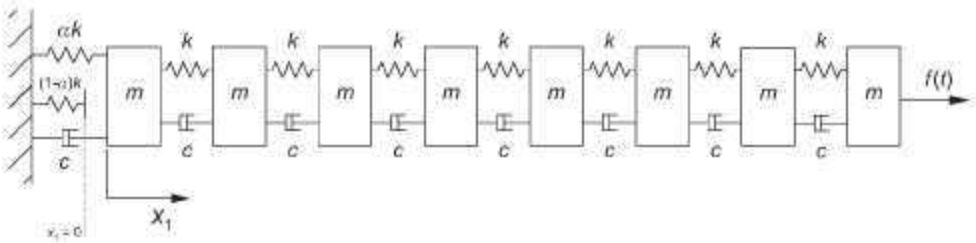

Figure 71. Eight Degree-of-Freedom model of a cantilever beam with a bilinear stiffness tosimulate damage.

A chaotic signal was created from the displacement response of a Duffing oscillator [84], which is known to be chaotic. Details of this process can be found in [99]. The attractor associated with the force is shown in Fig. 72. A time step of 0.0785s was used in the integration. The system parameters of the structure were chosen as $m = 0.01$, $c = 0.15$ and $k = 2$. Again, Fourth-order Runge-Kutta was employed for the simulation. The displacement x_1 of the first mass element was chosen as the variable to use in the calculation of the ALAVR because it was the most sensitive to the bilinear stiffness.

The ALAVR was calculated at each damage level over $N_t = 5000$ randomly selected points and local subsets were created using the $N_j = 40$ nearest points. The values of ALAVR obtained were normalized with respect to the ALAVR of the undamaged system so that

$$\Delta\overline{R} = \frac{|\overline{R} - \overline{R^*}|}{\overline{R}} \quad . \tag{101}$$

where $\overline{R^*}$ refers to the ALAVR of the undamaged system. The results are shown in Fig. 73.

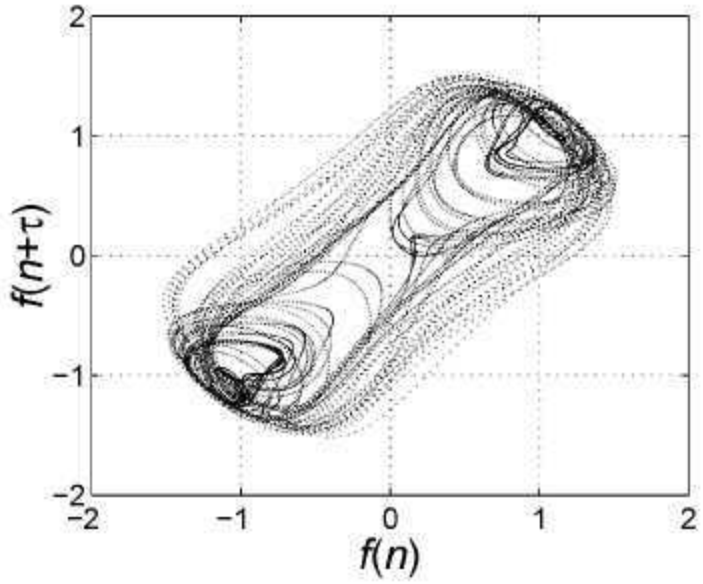

Figure 72. Reconstructed forcing attractor.

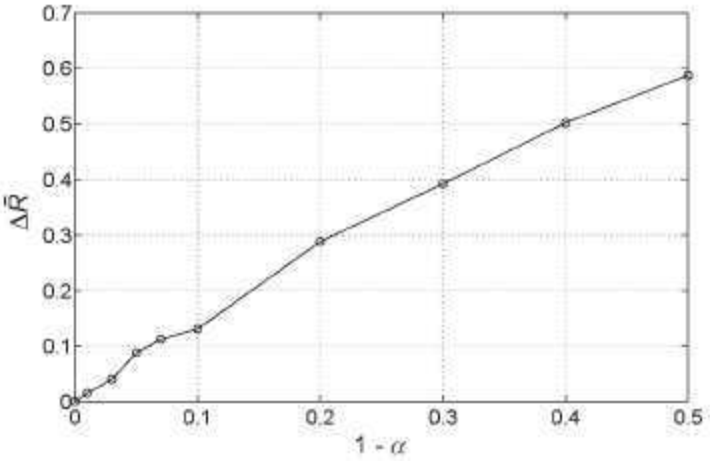

Figure 73. Normalized values of ALAVR at different damage levels.

There is a change in the geometry of the attractors and this is reflected in the values of ALAVR obtained. As the level of damage increased, the value of the ALAVR increased, indicating that the local variance of the attractors was also increasing. It was shown in [84] that the ALAVR can be used in a statistical procedure to flag damage with a given statistical confidence. The same procedure is expected to work here. Moreover, the same input/output attractor variance "mapping" implied by this procedure may be applied to output-only data. In other words, two measured responses can be compared in a similar way, forming their own cross variance ratio, which detects *relative* geometric changes

between responses. Such a formulation is useful when either one cannot measure the input or it may reasonably be hypothesized that the damage mechanism is closely related to synchronization or coupling between two output measurements, for example, a connectivity loss. A related attractor-based correlation metric was also discussed in [100].

8. NONLINEAR SYSTEM IDENTIFICATION APPROACHES

The system identification approach to damage detection proceeds in a different manner. The idea is to obtain estimates of the actual equations of motion of the system of interest using measured time series data. The presence (and location to an extent) of nonlinearities becomes immediately obvious in this approach.

8.1 Restoring Force Surface Model

In order to illustrate the methodology, the restoring force surface approach to identification will be discussed. This is a method developed by Masri and Caughey [101] and independently by Crawley and Aubert [102].

The equation of motion of a standard SDOF mass-spring-damper can be written as,

$$m\ddot{x} + g(x, \dot{x}) = f(t) \quad , \tag{102}$$

where m is the mass of the system and $g(x, \dot{x})$ is the internal restoring force which acts to return the oscillator to equilibrium when disturbed. The function g can be a quite general function of position $x(t)$ and velocity $\dot{x}(t)$. In the special case when the system is linear,

$$g(x, \dot{x}) = c\dot{x} + kx \quad , \tag{103}$$

where c and k are the damping constant and stiffness, respectively. Because g is assumed to be dependent only on x and $\dot{x}$, it can be represented by a surface over the phase-plane, i.e. the $(x, \dot{x})$-plane. A trivial re-arrangement of Eq. 102 gives,

$$g(x, \dot{x}) = f(t) - m\ddot{x} \quad . \tag{104}$$

If the mass m is known and the excitation $f(t)$ and acceleration $\ddot{x}(t)$ are measured, all the quantities on the right hand side of this equation are known and, hence, so is g. If $t_i = (i-1)\Delta t$ denotes the i^{th} sampling instant, then at t_i Eq. 104 gives,

$$g_i = g(x_i, \dot{x}_i) = f_i - m\ddot{x}_i \quad , \tag{105}$$

where $f_i = f(t_i)$ and $\ddot{x}_i = \ddot{x}(t_i)$ and hence g_i are known at each sampling instant. If the velocities $\dot{x}_i$ and displacements x_i are also known (i.e. from direct measurement or from numerical integration of the sampled acceleration data), at each instant $i = 1, \cdots, N$ a triplet $(x_i, \dot{x}_i, g_i)$ is specified. The first two values indicate a point in the phase plane, and the third gives the height of the restoring force surface above that point.

Given this scattering of force values above the phase plane, there are a number of methods of interpolating a continuous surface on a regular grid. The various interpolation and plotting procedures are discussed in some detail in [24]. Two simple approaches are followed here. In the first case, a force surface is obtained by dividing the phase plane into a regular grid and averaging the force values above the resultant cells. These average values are plotted above the centers of the cells. The main disadvantage of this approach is that there may be many phase-space cells that are empty of data points and, therefore, do not have force values. Such cells will produce 'holes' in the surface, although there are some simple heuristics that can be used to fill in some of the holes [24]. The main advantage of this approach is that a regular plotting grid is obtained that is amenable to standard graphics software. The second plotting procedure is to show a slice of the force data on a plane of constant velocity or displacement. This plot gives the stiffness and damping *sections* respectively.

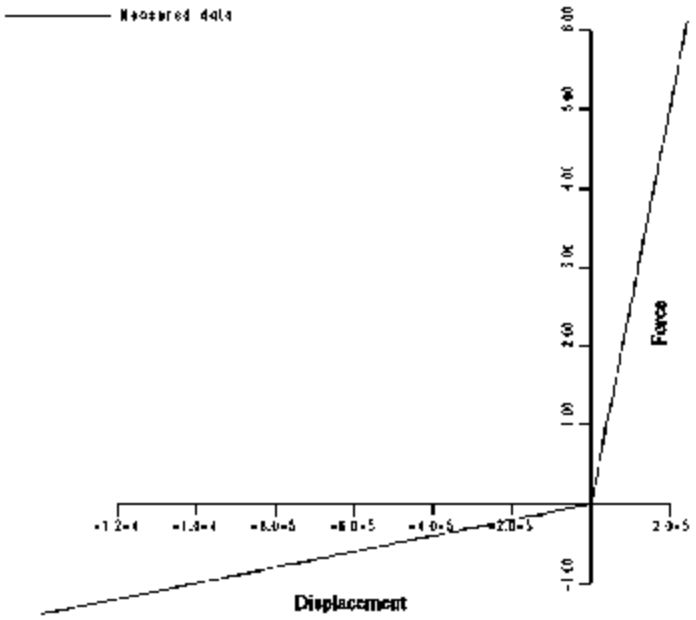

Figure 74. Stiffness section of SDOF system with bilinear stiffness representing a breathing crack.

In order to illustrate the approach in the context of damage identification, consider a bilinear system of the form shown in Fig. 74 that simulates a breathing crack. The k-value used was 10^4 and the stiffness ratio α was chosen as 10. As usual the time data were simulated using fourth-order Runge-Kutta integration scheme. In this case, because random excitation is preferred for system identification, the forcing $f(t)$ was taken as Guassian white noise. For the purposes of this simulation, the velocity and acceleration data were taken directly from the numerical solution of Eq. 90, as described above. In practice one would probably measure acceleration data and numerically integrate these data to obtain the corresponding velocities and displacements. The simplest representation of the force surface is the stiffness section and this is shown in Fig. 74.

A more comprehensive representation of the nonlinearity is given by the full restoring force surface as shown in Fig. 75. Both representations show the bilinear nature of the internal force and thus detect the presence of the 'crack'. In order to extract location information for the damage it is necessary to move to a more sophisticated MDOF model of the system.

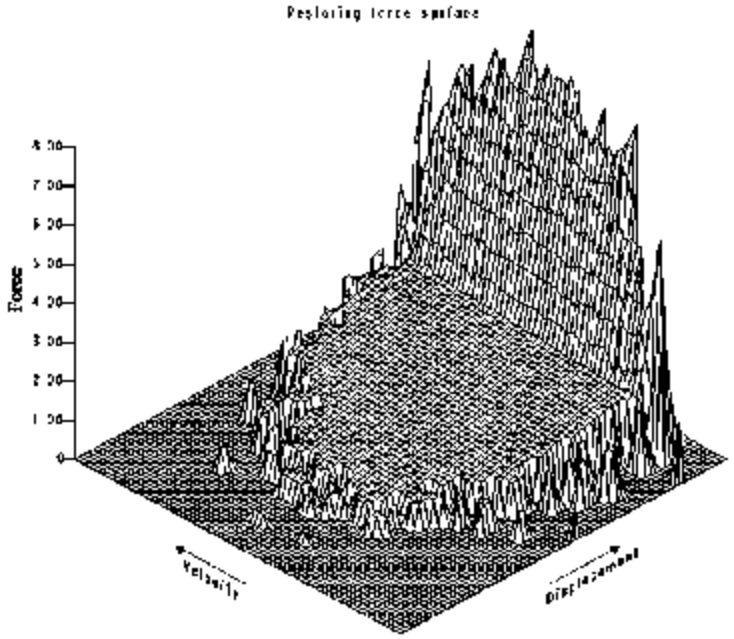

Figure 75. Restoring force surface for SDOF bilinear stiffness system.

For a general N DOF system, it is assumed that the mass is concentrated at N measurement points, m_i being the mass at point i. Each point i is then assumed to be connected to each other point j by a link l_{ij}, and to ground by a link l_{ii}. The situation is illustrated in Fig. 76 for a three degree-of-freedom system.

If the masses are displaced and released, they are restored to equilibrium by internal forces in the links. These forces are assumed to depend only on the relative displacements and velocities of the masses at each end of the links. If $\delta_{ij} = x_i - x_j$ is the relative displacement of mass m_i relative to mass m_j, and $\dot{\delta}_{ij} = \dot{x}_i - \dot{x}_j$ is the corresponding relative velocity, then,

$$\text{Force in link } l_{ij} = g_{ij}(\delta_{ij}, \dot{\delta}_{ij}), \tag{106}$$

where $\delta_{ii} = x_i$ and $\dot{\delta}_{ii} = \dot{x}_i$ for the link to ground. It will be clear that, as links l_{ij} and l_{ji} are the same,

$$g_{ij}(\delta_{ij}, \dot{\delta}_{ij}) = g_{ji}(\delta_{ji}, \dot{\delta}_{ji}) = g_{ji}(-\delta_{ij}, -\dot{\delta}_{ij}). \tag{107}$$

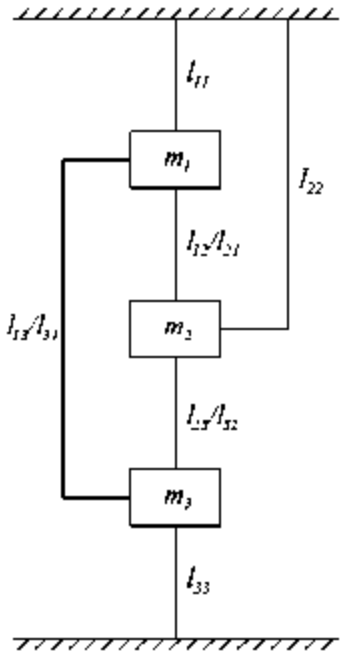

Figure 76. Link model of nonlinear 3DOF system.

If an external force $f_i(t)$ is now applied at each mass, the equations of motion are,

$$m_i\ddot{x}_i + \sum_{j=1}^{N} g_{ij}(\delta_{ij}, \dot{\delta}_{ij}) = f_i(t), \qquad i = 1, \ldots, N \tag{108}$$

It is expected that this type of model would be useful for representing a system with a finite number of modes excited. In practice, only the N accelerations and input forces at each point are measured. Differencing yields the relative accelerations $\ddot{\delta}_{ij}$, which can be integrated numerically to give $\dot{\delta}_{ij}$ and δ_{ij}. If a polynomial representation is adopted for g_{ij}, this gives a model,

$$m_i\ddot{x}_i + \sum_{j=1}^{N}\sum_{k=0}^{p}\sum_{l=0}^{q} a_{(ij)kl}\delta_{ij}^{k}\dot{\delta}_{ij}^{l} = f_i(t) \ . \tag{109}$$

Least-squares parameter estimation can be used to obtain the values of the coefficients m_i and $a_{(ij)kl}$ that best fit the measured data. If there is no excitation at point i, transmissibility arguments yield the appropriate form for the equation of motion of m_i,

$$\ddot{x}_i + \sum_{j=1}^{N}\sum_{k=0}^{p}\sum_{l=0}^{q} a'_{(ij)kl}\delta_{ij}^{k}\dot{\delta}_{ij}^{l} = 0 \ , \tag{110}$$

$$\text{where } a'_{(ij)kl} = \frac{1}{m_i}a_{(ij)kl} \ .$$

In principle, the inclusion of difference variables allows the model to locate nonlinearity; for example, if a term of the form δ_{23}^3 appears in the appropriate expansion one can *infer* the presence of a cubic stiffness nonlinearity between points 2 and 3 [103].

If one of the equations for an MDOF system has a non-zero input $f_i(t)$, then m_i can be estimated and it can be shown that this scale can be transferred to all equations so that the whole MDOF system can be identified using only one input.

A further advantage of adopting this model is that it allows a natural definition of the restoring force surface for each link. After obtaining the model coefficients the surface f_{ij} can be plotted as a function of δ_{ij} and $\dot{\delta}_{ij}$ for each link l_{ij}. In this case the surfaces are purely a visual aid to the identification. They might still be important however, as the polynomial representation does not offer a clue to the type of nonlinearity if it is piecewise linear for example.

To illustrate an MDOF application, a three mass system as shown in Fig. 76 was simulated (again using a Runge-Kutta integration scheme and a white noise excitation). The exact values of the various parameters are not important here, but the nonlinearity was placed between the central mass and ground. The nonlinearity used was a symmetric piecewise linear stiffness, which is the type that might be observed for loss of preload at a joint for example. After identification, the various restoring force surfaces could be plotted. Figure 77 shows the identified restoring force surface for the link l_{21} and is linear as expected. Figure 78 shows the identified surface for the link l_{22} and shows a symmetric nonlinearity. In fact this is only a cubic approximation to the real piecewise linear behavior and is a result of the cubic polynomial fit that was used to form the model. In order to more accurately see the piecewise nature, a higher order polynomial fit would be required.

The final example given here comes from an experimental study. A fatigue crack was grown at the center point of a 3-meter-long concrete beam. A random excitation was applied using an electro-dynamic shaker immediately below mid-span, the response was measured at various points on the top surface. In order to simplify matters, a SDOF restoring force surface analysis was carried out using the measured force and the response from the nearest accelerometer to the crack. The resulting stiffness section is shown in Fig. 79 with a ninth-order least-squares polynomial fit superimposed. Although the section is rather noisy (as a result of the neglected degrees of freedom), the smoothed curve fit shows a very clear bilinear nature as one might expect from a breathing crack.

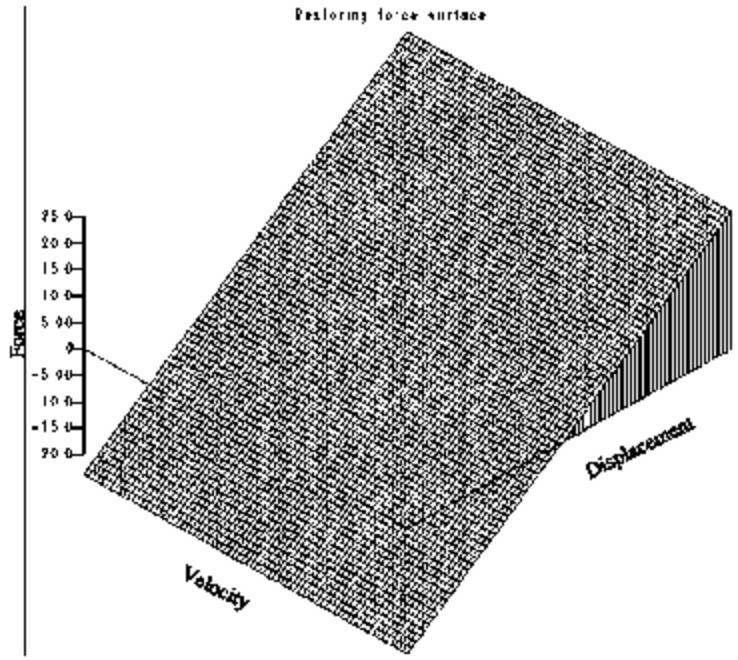

Figure 77. Model restoring force surface for link l21 of the simulated 3 DOF system.

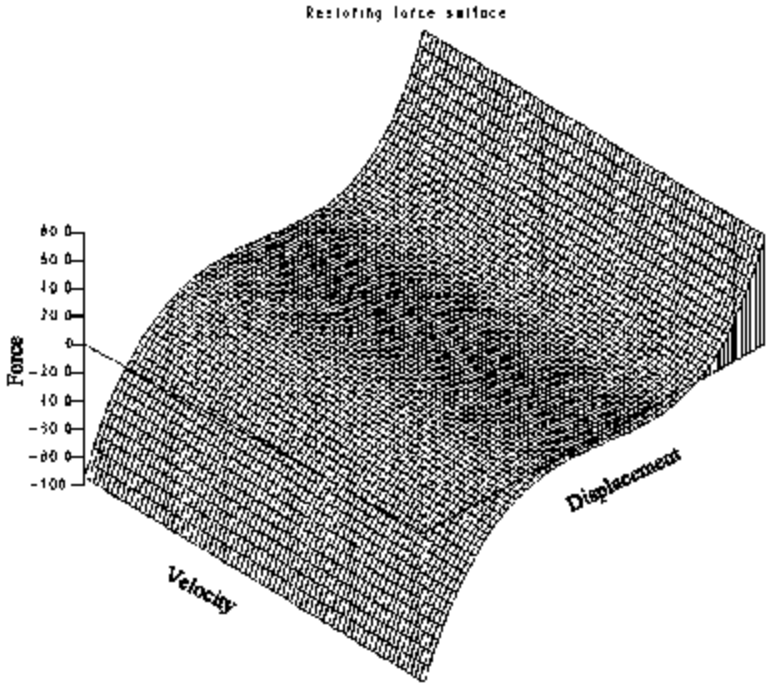

Figure 78. Model restoring force surface for link l22 of the 3 DOF simulated system.

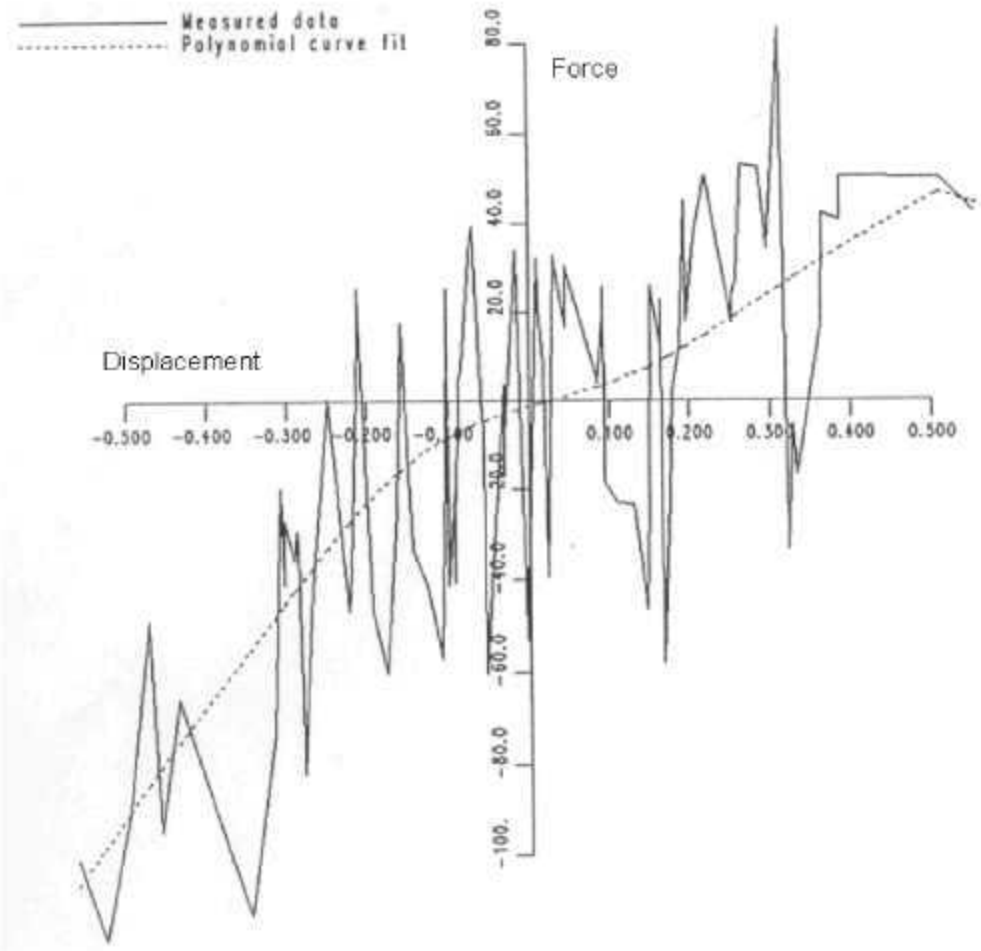

Figure 79. Restoring force surface for a concrete beam with fatigue crack.

8.2 Gradient Descent Methods for Nonlinear System Identification

As previously discussed, many of the nonlinear system identification approaches that are used for SHM require that a parametric model is fit to measured system input and/or response data. Changes in the parameters of these models are then used as damage indicators. Therefore, a fairly general description of the nonlinear system identification problem may be given as follows. The obtained time series data, y, are assumed to have been generated from a system that has a known functional form, but unknown parameters, such as

$$\begin{aligned} \dot{\hat{x}} &= f(\hat{x}, u, t, \theta) \\ \hat{y} &= g(\hat{x}, u, t, \theta) \end{aligned} \quad , \tag{111}$$

where f and g are some known functional forms with parameters θ and input u, and $\hat{x}$ and $\hat{y}$ are the estimated values of the states and outputs, respectively. The goal of the identification procedure is then to determine the parameters θ that best explain y and then

look for changes in those parameters when the identification procedure is repeated with new data. Such changes are inferred to be an indicator of damage. This parameter estimation is usually accomplished by minimizing some cost function. For example, given data from $t = 0$ to T and an estimate of a reasonable set of parameters, θ_0, a simple cost function, J, for the above model might be:

$$J = \int_0^T (y - \hat{y})^T Q(y - \hat{y}) + (\theta - \theta_0)^T R(\theta - \theta_0) dt \quad , \tag{112}$$

where Q is a user defined n x n positive, semi-definite matrix, and R is a user defined m x m positive-definite matrix, with n equal to the number of states and m equal to the number of parameters.

Thus, minimization of this cost function would seek to minimize the error in the estimate $\hat{y}$, without allowing the parameters to assume "unreasonable" values. This cost function can only be minimized iteratively, as it can not be minimized analytically. One minimization technique that can be used is gradient descent. In this method, the gradient of the cost function J with respect to the parameters θ is computed, and θ is updated so as to decrease J. This process is repeated until convergence or some other stopping criteria is achieved. Advantages to gradient descent include simplicity and, depending on the particular problem, rapid determination of $\partial J / \partial \theta$, even when θ is very high dimensional. The key disadvantage is susceptibility to local minima. Global optimization techniques such as evolutionary programming, surrogate management framework, and simulated annealing [104] seek to avoid the problem of local minima, but are not discussed in this section.

Once $\partial J / \partial \theta$ is obtained, one must decide how to use it to update θ. There are many methods that have been developed to perform this update. Among these methods are steepest descent, Newton's method and the conjugate gradient method [105]. For the sake of simplicity, this discussion will focus only on steepest descent. The other methods may loosely be viewed as modifications to the steepest descent method that seek to reduce the number of iterations required for convergence.

The update to θ using the steepest descent method is given by

$$\theta_{n+1} = \theta_n - \alpha \left. \frac{\partial J}{\partial \theta} \right|_{\theta = \theta_n} \quad , \tag{113}$$

where α is the size of the step. A common method of selecting α is by means of a line search, in which α is selected to minimize $J\left(\theta_n + \alpha \left. \frac{\partial J}{\partial \theta} \right|_{\theta = \theta_n} \right)$. One approach by which this minimization can be accomplished is to first perform an abbreviated Taylor series expansion of J.

$$J\left(\theta_n + \alpha \left.\frac{\partial J}{\partial \theta}\right|_{\theta=\theta_n}\right) \cong J(\theta_n) + \left.\frac{\partial J}{\partial \alpha}\right|_{\alpha=0} \alpha + \frac{1}{2}\left.\frac{\partial^2 J}{\partial \alpha^2}\right|_{\alpha=0} \alpha^2 \quad , \tag{114}$$

then, setting $\partial J / \partial \alpha = 0$, results in

$$\alpha = -\frac{\left.\frac{\partial J}{\partial \alpha}\right|_{\alpha=0}}{\left.\frac{\partial^2 J}{\partial \alpha^2}\right|_{\alpha=0}} \quad . \tag{115}$$

This procedure is easily demonstrated through an example. Consider the system in Fig. 80 which consists of two masses connected with springs and dampers to ground.

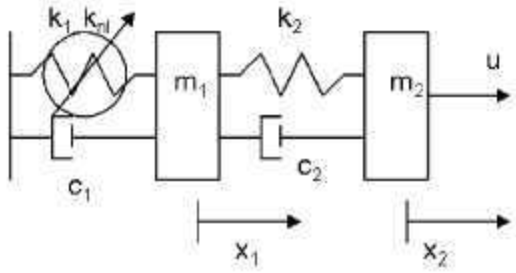

Figure 80.Nonlinear 2-DOF system.

The spring between ground and the first mass is a cubic spring, and the governing equations for the system are given by the following

$$\begin{aligned} m_1\ddot{x}_1 &= -k_1 x_1 - k_{nl} x_1^3 - c_1\dot{x}_1 + k_2(x_2 - x_1) + c_2(\dot{x}_2 - \dot{x}_1) \\ m_2\ddot{x}_2 &= -k_2(x_2 - x_1) - c_2(\dot{x}_2 - \dot{x}_1) + u(t) \\ y &= x_2 \end{aligned} \quad . \tag{116}$$

The goal is to estimate k_{nl} given knowledge of all other parameters and only y as a measurement. Given a measured time series y and some estimate $\hat{k}_{nl}$ of k_{nl} that results in an estimated time series $\hat{y}$, the cost function is then given by

$$J = \int_0^T (y - \hat{y})^T (y - \hat{y}) dt \quad . \tag{117}$$

$DJ / D\hat{k}_{nl}$ can be easily determined via finite difference.Let $\hat{k}'_{nl} = \hat{k}_{nl} + \delta$ be a perturbed $\hat{k}_{nl}$ that results in an estimated time series $\hat{y}'$. Then

$$DJ / D\hat{k}_{nl} = \frac{\int_0^T (y-\hat{y})^T (y-\hat{y}) dt - \int_0^T (y-\hat{y}')^T (y-\hat{y}') dt}{\delta} \quad (118)$$

For this case, the step size α can be seen to be given by

$$\alpha = -\frac{\left.\frac{\partial J}{\partial \alpha}\right|_{\alpha=0}}{\left.\frac{\partial^2 J}{\partial \alpha^2}\right|_{\alpha=0}} = -\frac{\frac{1}{2}\int_0^T (\hat{y}'-\hat{y})^T \hat{y} + \hat{y}^T (\hat{y}'-\hat{y}) dt}{\int_0^T (\hat{y}'-\hat{y})^T (\hat{y}'-\hat{y}) dt} \quad (119)$$

If we let $m_1 = m_2 = 1$, $k_1 = k_2 = 50$, $c_1 = c_2 = 1$, $k_{nl} = 10$, and u equal to the random input, shown in Fig. 81(a), then y is shown in Fig. 81(b). If we start with an initial guess of $\hat{k}_{nl} = 0$, then after approximately 30 iterations of the gradient descent procedure, $\hat{k}_{nl} = 9.999$, which is very close to the exact value of 10.0.

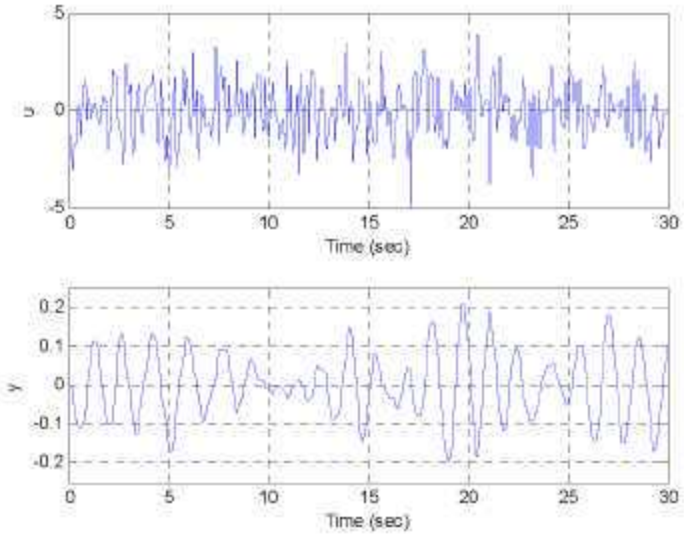

Figure 81. a) Random input (top), b) Response of mass 2 (bottom) for the system shown in Fig. 80.

8.3 Using Nonlinear System Models to Design Inputs for Active Sensing

Most procedures discussed thus far do not use an input that is designed to enhance the damage detection process. Instead, these methods work with whatever input and/or response can be measured during the structure's operation. However, with advent of active sensing approaches there can be SHM applications where the excitation is selectable, and, indeed,

where proper excitation selection is essential. As a simple example, consider a beam or column with a crack which is nominally closed because of a preload. If the provided excitation is not sufficient to open and close the crack, the detectability of the crack in the measured output will be severely limited. Thus, if possible, it is important to answer the question: "Given ever-present physical limits on the level of excitation, and limited outputs that can be measured, what excitation should be provided to a system to make damage most detectable?" When one considers that an excitation may be viewed as a time series with hundreds or thousands of free parameters, optimization in this high dimensional space might be a daunting task. However, as is demonstrated in this section, a gradient based technique may be used in which the gradient can be calculated very efficiently.

First, assume that undamaged and damaged structures excited with an input u may be modeled as follows:

$$\begin{aligned} \dot{x}_u &= f_u(x_u, u, t) \\ y_u &= Cx_u \end{aligned} \tag{120}$$

$$\begin{aligned} \dot{x}_d &= f_d(x_d, u, t) \\ y_d &= Cx_d \end{aligned} \tag{121}$$

or,

$$\begin{aligned} \dot{x} &= f(x, u, t) \\ y &= \begin{bmatrix} C & -C \end{bmatrix} x \end{aligned} \tag{122}$$

where x_u and x_d are the state vector of the undamaged and damaged systems respectively, $x = [x_u \; x_d]^T$ and $f(x,u,t) = \left[f_u(x_u,u,t) \; f_d(x_d,u,t)\right]^T$. C is simply a matrix such that the measurable output y_u and y_d are some linear combination of the states.

The excitation design problem may then be stated as the following optimization problem that seeks to make y (the difference between the outputs of the undamaged and damaged systems) is big as possible, given constraints on u.

$$\max J = \frac{1}{2}\int_0^T y^T y dt \,. \tag{123}$$

subject to Eq. 122 and $\|u\|_\infty < \gamma$.

This may be rewritten as

$$\max J = \frac{1}{2}\int_0^T x^T Q x dt \,. \tag{124}$$

subject to Eq 122 and $\|u\|_{\infty} < \gamma$, where $Q = [C \quad -C]^T [C \quad -C]$

If the input u is perturbed by u', the perturbed state trajectory is given by the tangent linear equation

$$x' = A(t)x' + B(t)u' \text{ or } \ell x = Bu' \tag{125}$$

where $\ell = \frac{d}{dt} - A$, and A and B are obtained by linearizing Eq 122 about x and u The resulting perturbation to J is then given by

$$J' = \int_0^T x^T Q x' dt \tag{126}$$

The goal of what follows is simply to re-express J' as a function linear in u' To that end, lets consider Eq 125 integrated against a test function, r

$$\int_0^T r^T \ell x' dt = \int_0^T r^T (\dot{x} - Ax') dt \tag{127}$$

Using integration by parts, Eq 127 can be rewritten as

$$\int_0^T r^T \ell x' dt = r^T x' \Big|_0^T - \int_0^T (\dot{r} + A^T r)^T x' dt = \int_0^T (\ell^* r)^T x' dt + r^T x' \Big|_0^T \tag{128}$$

where $\ell^* = -\frac{d}{dt} - A^T$ This is true for any test function, r If r is selected such that

$$\begin{aligned} \ell^* r &= Qx \\ r(T) &= 0 \end{aligned} \tag{129}$$

then Eq 126 can be rewritten as

$$J' = \int_0^T (\ell^* r)^T x' dt = \int_0^T r^T \ell x' dt = \int_0^T r^T B u' dt = \int_0^T \frac{DJ}{Du} u' dt \tag{130}$$

Thus,

$$\frac{DJ}{Du} = r^T B \tag{131}$$

Equation 129 is referred to as the adjoint equation. Therefore, given an initial guess at an excitation, u_n, Eq. 122 is solved for x. This x is then used to solve Eq. 129 in reverse-time, because r(T) is known. Thus, the gradient may be calculated from just two simulations, no matter how many points are in the time series for u. A typical gradient ascent procedure then follows, with the constraint being enforced by renormalizing the updated input after each iteration.

If one considers again the example in Section 8.2 and treat $k_{nl} = 10$ as the undamaged case, $k_{nl} = 9$ as the damaged case, and set the maximum input level $\gamma = 5$, then using the same random input as shown in Fig. 81(a), we see very little difference in the outputs of the undamaged and damaged systems, as shown in Fig. 82.

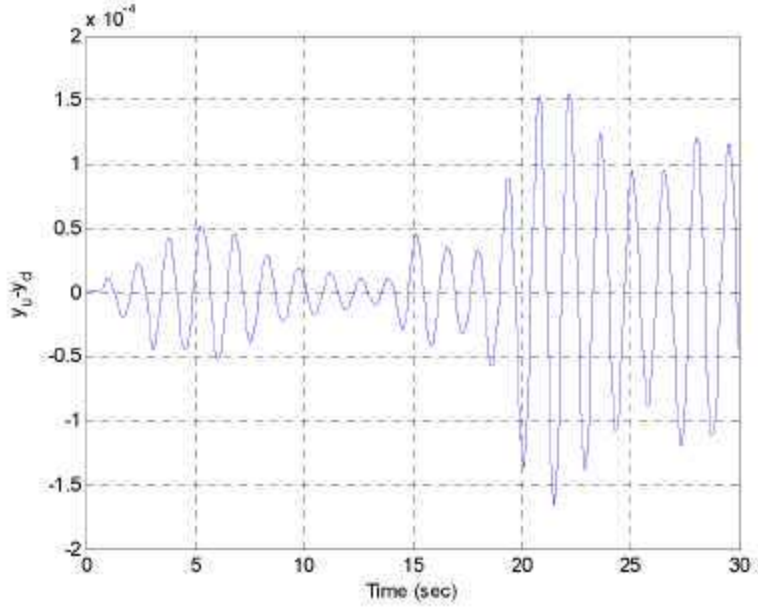

Figure 82. Difference in response due to random excitation for mass 2 shown in Fig. 80.

However, after just 20 iterations using the gradient ascent method outlined above, an excitation, shown in Fig. 83(a) is developed that yields a much larger difference in the outputs of the undamaged and damaged systems (by approximately a factor of 1000!), as shown in Fig. 83(b).

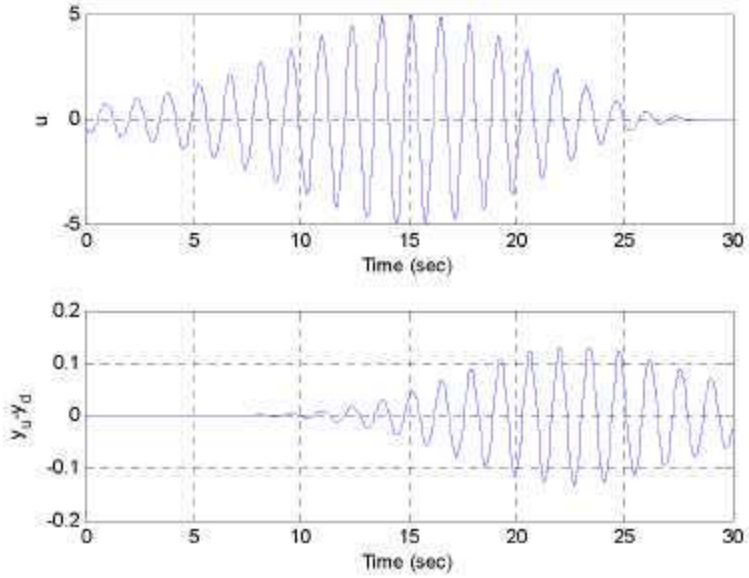

Figure 83. a) Optimized excitation, b) Difference in response with optimized excitation for mass 2 shown in Fig. 80.

No claim can be made that this method can provide a globally optimal excitation. However, if a particular excitation is being considered for a damage detection test, this method does allow one to easily determine if another excitation would be better. The method does require a model of the system and the accuracy of that model will influence the results. A more detailed discussion of the optimal excitation design for active sensing can be found in [106, 107].

8.4 Extended Kalman Filter

Another, more traditional method for parameter estimation is the Extended Kalman filter (EKF). Predictably, the "extended" moniker is due to the fact that it is an extension of the Kalman filter, which, for linear systems subject to Gaussian white noise disturbances to the states and outputs, provides optimal state estimation. By moving to a nonlinear process, the optimality guarantee is lost, and in fact, the estimate may diverge. This possibility for divergence is true even in the case of trying to identify the parameters of a linear system (since this is actually cast as a nonlinear system). However, in many cases, the EKF provides acceptable results. There are no shortage of texts and other resources available for more detailed information regarding the Kalman filter and EKF (e.g. [108, 109]), thus the EKF algorithm will simply be presented below, without proof, using the example problem above.

Recall that the goal is to estimate the value of k_{nl} in the 2-DOF system given by

$$m_1\ddot{x}_1 = -k_1x_1 - k_{nl}x_1^3 - c_1\dot{x}_1 + k_2(x_2 - x_1) + c_2(\dot{x}_2 - \dot{x}_1) \tag{132}$$

$$m_2\ddot{x}_2 = -k_2(x_2 - x_1) - c_2(\dot{x}_2 - \dot{x}_1) + u(t) \tag{133}$$

$$y = x_2 \tag{134}$$

We rewrite this system to treat k_{nl} as one of the states:

$$\begin{aligned}
\dot{x}_1 &= v_1 \\
\dot{v}_1 &= \frac{1}{m_1}\left(-k_1 x_1 - k_{nl} x_1^3 - c_1 v_1 + k_2(x_2 - x_1) + c_2(v_2 - v_1)\right) \\
\dot{x}_2 &= v_2 \\
\dot{v}_2 &= \frac{1}{m_2}\left(-k_2(x_2 - x_1) - c_2(v_2 - v_1) + u(t)\right) \\
\dot{k}_{nl} &= 0 \\
y &= x_2
\end{aligned} \tag{135}$$

For convenience, we can use simple Euler integration to solve this set of ODE's and obtain

$$\begin{aligned}
x_{1,n+1} &= \Delta t(v_{1,n}) + x_{1,n} \\
v_{1,n+1} &= \Delta t\left(\frac{1}{m_1}\left(-k_1 x_{1,n} - k_{nl,n} x_{1,n}^3 - c_1 v_{1,n} + k_2(x_{2,n} - x_{1,n}) + c_2(v_{2,n} - v_{1,n})\right)\right) + v_{1,n} \\
x_{2,n+1} &= \Delta t(v_{2,n}) + x_{2,n} \\
v_{2,n+1} &= \Delta t\left(\frac{1}{m_2}\left(-k_2(x_{2,n} - x_{1,n}) - c_2(v_{2,n} - v_{1,n}) + u_n\right)\right) + v_{2,n} \\
k_{nl,n+1} &= k_{nl,n} \\
y_{n-1} &= x_{2,n+1}
\end{aligned} \tag{136}$$

which is of the form

$$x_{n+1} = f(x_n, u_n), \; y = h(x_n), \tag{137}$$

where $x = [x_1 \;\; v_1 \;\; x_2 \;\; v_2 \;\; k_{nl}]^T$.

We define

$$A = \frac{\partial f}{\partial x} = \Delta t \begin{bmatrix} 0 & 1 & 0 & 0 & 0 \\ -\frac{k_1 + k_2 + 3k_{nl}x_1^2}{m_1} & -\frac{c_1 + c_2}{m_1} & \frac{k_2}{m_1} & \frac{c_2}{m_1} & -\frac{x_1^3}{m_1} \\ 0 & 0 & 0 & 1 & 0 \\ \frac{k_2}{m_2} & \frac{c_2}{m_2} & -\frac{k_2}{m_2} & -\frac{c_2}{m_2} & 0 \\ 0 & 0 & 0 & 0 & 0 \end{bmatrix} + I \tag{138}$$

$$C = \frac{\partial g}{\partial x} = [0\ 0\ 0\ 1\ 0] \tag{139}$$

There are two basic steps in the estimation process: a prediction step and an update step. In the prediction step, the state estimate is given by:

$$\hat{x}_{n-1} = f(\hat{x}_n, u_n) \tag{140}$$

and the error covariance matrix is given by:

$$P_{n+1} = A_n P_n A_n^T + Q \tag{141}$$

where Q is an estimate of the state (or process) error covariance matrix. For this simple example we take it to be

$$Q = \begin{bmatrix} 0 & 0 & 0 & 0 & 0 \\ 0 & 0 & 0 & 0 & 0 \\ 0 & 0 & 0 & 0 & 0 \\ 0 & 0 & 0 & 0 & 0 \\ 0 & 0 & 0 & 0 & 100 \end{bmatrix} \tag{142}$$

because the only state that we don't know at the beginning is k_{nl}, and there isn't any process noise that can perturb the states.

The update step is as follows:

$$\begin{aligned} \tilde{y}_{n+1} &= y_{n+1} - \hat{y}_{n+1} \\ S_{n+1} &= C_{n+1} P_{n+1} C_{n-1}^T + R \\ K_{n+1} &= P_{n+1} C_{n+1}^T S_{n+1}^{-1} \\ \hat{x}_{n-1} &= \hat{x}_{n+1} + K_{n+1} \tilde{y}_{n+1} \\ P_{n-1} &= (I - K_{n+1} C_{n+1}) P_{n+1} \end{aligned} \tag{143}$$

and R is the output noise covariance, which for our example, we take to be R=1.

We start the filter by assuming $\hat{x}_0 = 0, P_0 = 0$. Then, by following the above procedure, and given the actual x_2 that would be obtained using the random input and $k_{nl} = 10$ we obtain the plot shown in Fig. 84 for the estimation of k_{nl}.

Clearly, the estimate for k_{nl} is approaching the value of 10.

From this example one can envision applications to damage detection where changes to the system are not only detected, but also quantified and assigned a physical meaning. Assuming one has a model of the system, data would be acquired in the undamaged condition and state variables associated with this model would be estimated using the extended Kalman filter. Then at periodic intervals, or after a potentially damaging event trigger a new measurement, the system identification process would be repeate. The new state variables would be analyzed to determine if they have changed in a statistically significant manner from the baseline condition. As with many other approaches discussed in this report, the question arises regarding the suitability of a single model for both the damaged and undamaged conditions. Also, environmental and operational variability can cause changes in the system states that are not associated with damage. Such changes are inherent in all damage detection procedures and must be dealt with through additional measurements of conditions such as temperature and through additional statistical pattern recognition procedures.

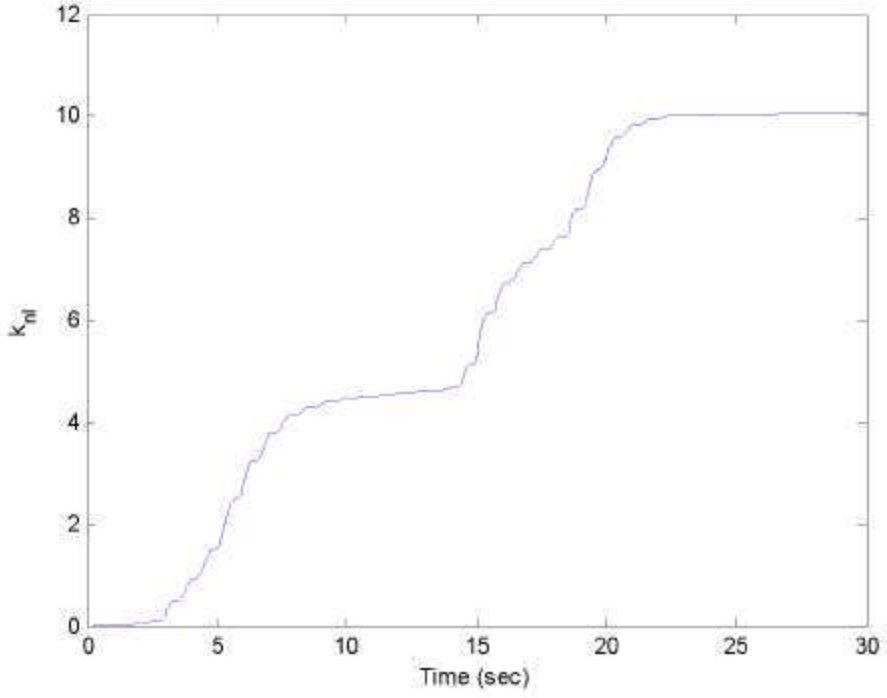

Figure 84. Extended Kalman filter estimate of the nonlinear stiffness coefficient.

9. CHALLENGES AND FUTURE RESEARCH NEEDS

Sections 6–8 of this report discussed many approaches where nonlinearity is either being identified, exploited, or actively used for structural health monitoring and damage prognosis (SHM/DP). Despite the fact that many engineered systems can and do behave in often subtle nonlinear ways—particularly once damage has initiated—these nonlinear identification or exploitation approaches rarely have made the transition into practical use. Does this mean they are of academic interest only? The answer may seem affirmative at present, and there are, very generally, three classes of related reasons why this may be true.

9.1 Nonlinear Behavior Does Not Generalize

In fact, nonlinearity cannot be defined *per se*; rather, it is defined by what it is not, namely, any process that does not fundamentally obey the principles of homogeneity and superposition, that is,

$$H\left(\sum_{n=1}^{N} a_n x_n\right) \neq \sum_{n=1}^{N} a_n H(x_n), \tag{144}$$

where H is the system response to weighted inputs $\sum_{n=1}^{N} a_n x_n$.

For linear systems, an equality sign holds in Eq. 132, and a number of very generalized concepts follow, such as reciprocity, input level insensitivity, and certain symmetries, as discussed in Section 4. These properties lead to a single class of approaches for analysis. Linear systems have well-defined and well-understood behavior, and mathematically they may be solved by fundamental numerical and analytical techniques that are independent of the specific physics of the system. A classic example is the analogous behavior of a simple elastic spring/mass/dashpot mechanical system to a simple capacitor/inductor/resistor electrical circuit. Both have exactly the same form of dynamic behavior, even though the solution parameters (e.g., spring vs. capacitor) have very different physical interpretations. In other words, the typical techniques used to characterize the mechanical system, or changes to it, would in general work equally well to characterize the electrical circuit and its associated changes . This is not the case for a nonlinear system, where specific physics typically dictate the need for a specific nonlinear model, which in most cases subsequently does not have a solution that generalizes for any value of the system parameters. Thus, analysis techniques that may prove useful for one nonlinear system may have little value for another.

With this in mind, perhaps the most directly adverse effect of nonlinear processes on SHM strategies is the lack of invertibility. SHM is inherently an inverse problem; data are measured and mined for information that reveals something about the existence, location, extent, or type of damage. Thus, the practitioner has an effect usually in the form of measured system response data that requires diagnosing a particular cause, which in the case of SHM is damage. Nonlinearity implies lack of a guaranteed unique inverse relationship, or

that one even exists. The practitioner "forces" the effect to match the cause and may very well do so for the limited case or cases at hand, but there is no such guarantee that damage is the only cause that leads to a particular damage set. That is not to say that linearity guarantees inverses or well-conditioned inverses; however, one can much more readily find data transformations in the linear domain that properly reduce and/or orthogonalize the data in order to better condition the inverse by "orthogonalizing" possible multiple causes. The nonlinear problem may be partially mitigated, although not "solved," for nonlinear systems by performing experiments in the forward direction, e.g., damaging a system in a controlled but field-realistic manner and observing what subsequent response changes occur in order to build an appropriate data- or physics-based model. Of course, such a forward approach requires a heavily supervised learning mode, which system owners most often do not have the economic or life-safety justification to implement.

9.2 Nonlinear Approaches are Computationally Cumbersome, Expensive, and Require too Many Parameters to be Defined

In part, this point is related to the previous point about lack of generality. The less general a model or technique is, the more input parameters (i.e., "knobs" or "tweak parameters") the model generally requires to make it function properly. Consequently, the model or technique's outputs are often highly sensitive to these inputs so that the robustness of the technique is called into question. One example of this lack of generality is with some of the information-based metrics such as transfer entropy that are being applied to data to detect nonlinearity. While such a method was clearly shown to be an efficient nonlinearity detector for composite delamination and bolt loosening applications, the parameters chosen to construct the probabilities that go into the calculation (e.g., neighborhood size and kernel condition) have large effects on the quantitative transfer entropy estimation that is directly used as the feature. In another example, the actual calculation of the neighborhoods in the attractor-based methods of Section 7.2 can be very time-consuming, especially for a large data set. While k-d tree methods [110] have given a more computationally efficient means to partition state space in this case, run times for a technique that requires this are an order of magnitude slower than a comparable linear technique that does not require this partitioning. Furthermore, the memory and resident libraries required to implement this makes system-on-a-chip (SOC) solutions less attractive, although still possible. In general, specialized algorithms that do not generalize well, which by definition include most nonlinear analyses, are generally not as conducive to efficient mass production because of a lack of generalized market. They also do not possess the kind of robustness required for consistent application and this lack of robustness results in lack of confidence by owners, regulators, and users.

Finally, it is noted the mathematics, in general, is no setup to deal with nonlinear systems. Historically, mathematics has been built with a complete dependence on linearity. An immediate example of this focus on linearity is the entire framework of vector space theory. This lack of a mathematical framework to address nonlinear problems is possibly the biggest challenge to further development and adaptation of nonlinear system identification approaches for SHM applications.

9.3 Many Existing Engineers, Technicians, and System Certifiers are not Comfortable with and/or Even Trained with Nonlinear Processes or Analysis Techniques

The previous points in part fuel this point. The fact that nonlinearity does not have well-understood ubiquitous behavior and that nonlinear methods can be too parameter-sensitive (and thus nonrobust) fail to give system owners and/or safety certifiers confidence in their use for SHM applications. Economic and liability issues dictate, in most applications, relatively strict or conservative guidelines for design and performance specifications, including monitoring systems, with very high required reliability. The SHM/DP system itself cannot be the most unreliable component. This overall lack of confidence is rooted even earlier by a lack of exposure in technical education programs; most technically-trained personnel do not study nonlinear processes or any form of nonlinear behavior at the undergraduate level. Even at the graduate level, exposure is very limited or narrowly focused and does not at all consider uncertainty propagation or quantification, which are very important concepts linked to assessing a model or technique performance. This issue is particularly acute for nonlinear models where the physics may not be exactly known or characterized.

9.4 Other Technical Challenges

There are still many other outstanding issues for the application of nonlinear system identification methods to SHM problems. In most cases reported herein, almost all studies have been applied to laboratory structures of relatively simple geometry or to numerical simulations of similarly simple structures. If these approaches to SHM feature extraction are to make the transition from a research demonstration to practical application, studies must be conducted on more complicated systems with numerous joints and interfaces between structural elements.

Also, this report has been limited to applications where the structure of interest can accurately be modeled as a linear system when in its undamaged state. Many real-world structures, particularly those with numerous complicated joints and interfaces, will exhibit nonlinear response in their undamaged state. Therefore, approaches that can distinguish changes in nonlinear response associated with varying damage levels from the inherent nonlinearities associated with the system in its undamaged condition are needed.

The studies reported herein have not addressed many other issues associated with using nonlinear system identification for damage detection. These issues include the amplitude dependence of many nonlinearities and the ability of the excitation sources (ambient of prescribed) to excite the nonlinearity. In most studies quantifying the location of the nonlinearity, identifying the type of nonlinearity, identifying the extent of damage associated with the nonlinearity, and the time-rate-of-change of the damage based on changes of the measured response have not been addressed. Also, most studies of systems with nonlinearities caused by damage tend to focus on discrete source nonlinearities such as a local crack or single-stiffness element. Most studies have not focused on distributed sources of nonlinearities such a distributed crack field that may occur in a concrete structure.

Almost all SHM/DP studies that make use of nonlinear system identification do so in a passive sensing mode. By passive sensing, it is implied that a prescribed input with a known waveform that is designed to enhance the damage observability has not been used. The active sensing approaches associated with the nonlinear acoustic methods (Section 6.14), local attractor variance methods (Section 7.2), and the optimal input design (Section 8.3) are examples where researchers are starting to couple active sensing with nonlinear system identification to enhance the damage detection process.

Finally, most of the experimental studies reported herein have been conducted in well-controlled laboratory settings. The ability of these methods to distinguish changes in system response associated with damage from changes associated with varying operational and environmental conditions has not been established.

10. RECOMMENDATIONS

Given these barriers and challenges, a number of things can be done to promote the development, testing, and eventual deployment (if successful) of nonlinear approaches for SHM/DP. The ultimate payoff of many nonlinear assessment techniques or modeling is greatly increased sensitivity to damage characterization, but this cannot come at the cost of excessive economic, execution (e.g., computational), or robustness burdens. Some recommendations for future research and development are listed below.

10.1 Fundamental Benchmark Platforms

The SHM/DP community stakeholders (industry, government agencies, researchers) should propose an array of fundamental platforms in key markets (civil, aerospace, manufacturing, etc.) that will serve to host benchmark studies. Such studies should have the following characteristics:

1. With input from owners and regulatory agencies, develop several long-term test beds that cover aerospace, mechanical and civil applications. A candidate mechanical system might be as a wind turbine where damage to the composite blades and gear boxes are to be identified. Developing a damage detection approach for wing of an unmanned aerial vehicle is a possible aerospace application where damage may result from debris impact. Many aspects of bridge damage detection such the identification of fatigue cracks in welded plate girders is a possible candidate for the application of nonlinear system identification methods.
2. Define realistic damage to be detected. Appropriate failure modes must be controllably introduced and propagated under expected loading scenarios (a *forward direction* test).
3. Operational and environmental variables should be controllable to realistic conditions observed in practice.
4. Sensor and actuator arrays should be defined and deployed to accommodate a wide variety of methods (time and length scales).

5. Have an independent panel run the tests and assess the ability of the SHM system to detect the damage.
6. Make the test bed available to as many researchers as possible.
7. Require completely open disclosure of results. Include what didn't work as well as what did work in these presentations. Also, report information like required SHM system maintenance, down time, false-positives, and comparisons with more traditional linear methods of damage detection

All results should include full, detailed documentation of how each method was applied and what the failures of the method were in addition to any successes. Method 'performance metrics' should be defined (energy budget, execution time, footprint/weight, statistical confidences, resolution, accuracy, economic cost, etc.) and a global objective function defined that each method may be independently and objectively characterized for comparative purposes. These benchmark tests should be funded primarily by government funding agencies (80%) with secondary buy-in from industry (20%).

The data sets being made available at the Engineering Institute web page (www.lanl.gov/projects/ei) and described in Appendices A and B are a start at providing standard test structures and data to validate damage detection algorithms (both linear and nonlinear approaches). However, these structures are laboratory test specimens and do not have all the desired attributes listed above.

10.2 Increased Industry and Government Investment

Industry and government agencies such as the Department of Defense are ultimately the ones that directly stand to benefit from SHM/DP technology. Therefore, after benchmarks have been demonstrated that objectively compare methods on different platforms, industry and government agencies must be willing to invest directly in transitioning promising technologies to practice, including further long-term testing and development, packaging, and appropriate calibrations and certifications.

10.3 Education

The university system also plays a key role in overcoming these challenges, as universities are usually the first major stop in an engineer or scientist's career. Universities must:

1. Start *actively* deploying multidisciplinary educational programs that give a systems-level perspective to students at both the undergraduate and graduate levels. In particular for SHM/DP, the sensing, feature extraction, statistical modeling, and predictive modeling components span almost all traditional engineering departments and degree programs must be designed in which students can transcend these traditional boundaries. Exposure to advanced and emerging technologies such as some forms of nonlinear analysis must be included in this transformation.

2. Actively *encourage and reward* their faculty for forming multidisciplinary teams to solve the systems-level problems that SHM/DP applications pose. No one faculty member, department, or even university can claim to 'corner the market' on SHM/DP expertise, and true collaboration—where the rewards are both external (solving real problems for increased industrial competitiveness in a global market) and internal (faculty/researcher careers are promoted for teamwork)—is the only solution.
3. Be willing to form organizations with industrial partners to work in "IP-free" zones where research and development can be performed in free and open exchange without the restrictions of nondisclosure agreements. Such an arrangement, for example, is currently in place for the sixth-floor laboratories in the University of California San Diego division of the California Institute of Telecommunication and Information Technology (Calit2) (http://www.calit2.net).

11. SUMMARY

The basic premise of this report is that in many cases damage causes a structure that initially behaves in a predominantly linear manner to exhibit nonlinear response when subject to dynamic loads associated with its operating environment. Therefore, many approaches to nonlinear system identification are directly applicable to damage detection. This report has summarized a variety of these nonlinear system identification techniques that have been reported in the structural health monitoring literature and classified them into the following three groups:

Methods based on nonlinear indicator functions

Methods based on nonlinear dynamical systems theory

Methods based on nonlinear system identification approaches

This report has also addressed the levels of damage identification that can be obtained with each method as well as the limitations of these various methods when applied to SHM problems.

Several approaches to SHM based on nonlinear structural dynamics are discussed in this report. First, features that can be used to identify nonlinear system response such as harmonic generation, the coherence function, probability density function distortion, correlation tests, and the Holder exponent were discussed and applications of these indicators to analytical and experimental damage detection studies were presented. These techniques can only identify the presence of a nonlinearity that would be indicative of damage. Information about location or extent of damage can not, in general, be obtained with these features. It was also pointed out that some of the indicators such as the coherence function can change significantly as a result of other factors not related to damage.

Next, a data analysis approach motivated by nonlinear dynamical systems theory was developed to quantify features of chaotic attractors that can be related to damage. It was shown that bilinear stiffness nonlinearity, typical of a breathing crack, caused a chaotic response when the system was subjected to a harmonic excitation and thus produced a fractional-dimensional attractor in phase space. This method was shown to be successful at identifying the presence of damage. However, despite the fact that certain invariants are a necessary consequence of nonlinearity, the simulations indicated that it is unlikely that features of the chaotic response like fractal dimension of the attractor or Lyapunov exponents would be of value for damage quantification. This statement is based on the fact that the response moves between super-harmonic, subharmonic and chaotic response in a disorderly fashion as a function of forcing frequency or damage extent. Therefore, the features are not monotonic functions of damage extent.

In the second illustration motivated by nonlinear dynamical systems theory, the use of a chaotic signal to interrogate a damaged structure provided a sensitive method of quantifying the level of damage in the system. The damage, in the form of a bilinear stiffness in one of the spring elements of a MDOF system, altered the geometry of the input attractor to a great enough extent for it to be measured using the average local attractor variance ratio.

In Section 7 the application of nonlinear system identification to the SHM problem was considered. To simplify matters, a single technique known as the restoring force method was illustrated. The analysis showed that for SDOF systems at least, a picture of the nonlinearity can be obtained and this picture can be used to characterize the nonlinearity. For MDOF systems, the analysis can potentially be extended to locate the source of the nonlinearity. In both cases, the coefficient of the nonlinear terms in the equations of motion can give guidance on the extent of the damage present. This portion of the report concluded by showing how a nonlinear system model can be used to design an optimal input for damage observability when the SHM process makes use of an active sensing approach.

To conclude, the authors acknowledge that this report has only really just begun to introduce possible nonlinear dynamics system assessment methods that are applicable to the SHM problem. The literature on nonlinear structural dynamics is extensive and other nonlinearity detectors have not been discussed. Similarly, identification methods like Reverse Path Analysis [111] have been neglected. Readers may wish to consult one of the major reviews or books [24] available on the subject of nonlinear dynamics to become familiar with these various approaches to nonlinear dynamics system assessment.

12. REFERENCES

1. K. Worden, J.M. Dulieu-Barton, "An Overview of Intelligent Fault Detection in Systems and Structures," *International Journal of Structural Health Monitoring*, 2004, **3**(1) pp. 85–98.

2. C. R. Farrar, S. W. Doebling, and D. A. Nix, "Vibration-Based Structural Damage Identification," *Philosophical Transactions of the Royal Society: Mathematical, Physical & Engineering Sciences*, 2001, **359**(1778) pp. 131–149.

3. H. Sohn, C. R. Farrar, F. M. Hemez, D. D. Shunk, D. W. Stinemates, and B. R. Nadler, "A Review of Structural Health Monitoring Literature from 1996–2001," *Los Alamos National Laboratory report LA-13976-MS*, 2004.

4. S. W. Doebling, C. R. Farrar, M. B. Prime, and D. Shevitz, "Damage Identification and Health Monitoring of Structural and Mechanical Systems From Changes in their Vibration Characteristics: A literature Review," *Los Alamos National Laboratory report LA-13070-MS*, 1996.

5. G. Park, H. Sohn, C. R. Farrar, and D. J. Inman, "Overview of Piezoelectric Impedance-Based Health Monitoring and Path Forward," *Shock and Vibration Digest*, 2003, **35**(6) pp. 451–463.

6. H. Sohn, G. Park, J. R. Wait, N. Limback, and C. R. Farrar, "Wavelet-Based Signal Processing for Detecting Delamination in Composite Plates," *Smart Material and Structures*, 2004, **13**(1) pp. 153–160.

7. S. S. Kessler, S. M. Spearing, and C. Soutis, "Damage Detection in Composite Materials using Lamb Wave Methods," *Smart Materials and Structures*, 2002, **11**(2) pp. 269–278.

8. J. B. Ihn and F. K. Chang, "Detection and monitoring of hidden fatigue crack growth using a built-in piezoelectric sensor/actuator network: II. Validation using riveted joints and repair patches," *Smart Materials and Structures*, 2004, **13**(3) pp. 621–630.

9. C. R. Farrar, H. Sohn, and K. Worden, "Data Normalization: A Key to Structural Health Monitoring," *Proc. of the Third International Structural Health Monitoring Workshop*, Stanford, CA. DEStech Publications, Inc., Lancaster, PA 2001, pp. 1229-1238.

10. G. Park, C. R. Farrar, M. D. Todd, W. Hodgkiss and T. Rosing "*Power Harvesting for Embedded Structural Health Monitoring Sensing Systems,*" Los Alamos National Laboratory report, LA-14314-MS, 2007.

11. N. M. M. Maia and J. M. M. Silva, *Theoretical and Experimental Modal Analysis*. John Wiley and Sons, Inc., NY, 1997.

12. D. J. Ewins, *Modal Testing: Theory and Practice*. John Wiley and Sons, Inc., NY, 1995.

13. M. I. Friswell and J. E. Mottershead, *Finite Element Modal Updating in Structural Dynamics*, Kluwer Academic Publishers, Dordrecht, The Netherlands, 1995.

14. M. Link, "Updating of analytical models – review of numerical procedures and application aspects," In *Structural Dynamics @ 2000: current status and future direction*, Research Studies Press LTD., Bladock, England, 2001.

15. C. R. Farrar, P. J. Cornwell, S. W. Doebling, and M. B. Prime, Structural health monitoring studies of the Alamosa Canyon and I-40 bridges. *Los Alamos National Laboratory report, LA-13635-MS*, 2000.

16. C. R. Farrar, et al., "*Dynamic Characterization and Damage Detection in the I-40 Bridge over the Rio Grande,"Los Alamos National Laboratory report LA-12767-MS*, June 1994.

17. J. S. Mitchell, *Introduction to Machinery Analysis and Monitoring*, PenWel Books, Tulsa, 1993.

18. A. R. Crawford, *The Simplified Handbook of Vibration Analysis*, Computational Systems, Inc., Knoxville, 1992.

19. B. Watts and J. Van Dyke, Sr., "An Automated Vibration-Based Expert Diagnostic System", *Sound and Vibration*, September, 1993, pp. 14–20.

20. W. T. Thomson and M. D. Dahleh, *Theory of Vibrations with Applications*, Prentice-Hall, Inc. Englewood Cliffs, NJ, 1998.

21. J.-P Eckmann and D. Ruelle, "Ergodic Theory of Chaos and Strange Attractors", *Reviews of Modern Physics*, 1985, **57**(3), pp. 617-656.

22. J. T. Oden and L. F. Demkowicz, *Applied Functional Analysis*, CRC Press, Boca Raton Fla., 1996.

23. T. Schreiber and A. Schmitz, "Surrogate Time Series", *Physica D*, 2000, **142**, pp. 346-382.

24. K. Worden and G. R. Tomlinson, *Nonlinearity in Structural Dynamics: Detection, Identification and Modelling*, Institute of Physics Publishing, Bristol, 2001.

25. M. I. Friswell and J. E. T. Penny, "Crack modelling for structural health monitoring," *International Journal of Structural Health Monitoring* 2002, **1**, pp. 139–148.

26. J. S. Rao, *Vibratory Condition Monitoring of Machines*, C.R.C. Press, 2000.

27. M. B. Prime and D. W. Shevitz, "Linear and nonlinear methods for detecting cracks in beams," *Proceedings of the 14th International Modal Analysis Conference*, 1996, pp. 1437–1443.

28. A. H. Nayfeh and D. T. Mook, *Nonlinear Oscillations*. Wiley Interscience, 1979.

29. F. Dinca and C. Teodosiu, *Nonlinear and Random Vibrations*. Academic Press. 1973.

30. H. Sohn, and C. R. Farrar, "Damage Diagnosis Using Time Series Analysis of Vibration Signals," *Journal of Smart Materials and Structures*, 2001, **10**, pp. 446–451.

31. H. Sohn, K. Worden, C. R. Farrar, "Statistical damage classification under changing environmental and operational conditions," *Journal of Intelligent Material Systems and Structures*, 2003, **13**(9) pp. 561–574.

32. H. R. Martin, "Statistical moment analysis as a means of surface damage detection," *Proceedings of the International Modal Analysis Conference* 1989, pp. 1016–1021.

33. S. A. Billings and K. M. Tsang, "Spectral analysis of block-structured nonlinear systems.," *Mechanical Systems and Signal Processing*, 1990, **4**, pp. 117–130.

34. S. A. Billings and M. B. Fadzil, "The practical identification of systems with nonlinearities," *Proceedings of IFAC Symposium on System Identification and Parameter Estimation, York*, 1985.

35. A. N. Robertson, C. R. Farrar and H. Sohn, "Singularity detection for structural health monitoring using Holder exponents," *Mechanical Systems and Signal Processing* 2003, **17**(6), pp. 1163–1184.

36. S. Mallat, S. and W. L. Hwang, "Singularity detection and processing with wavelets", *IEEE Transactions on Information Theory*, 1992, **38**, pp. 617–643.

37. A. Struzik, "Wavelet Methods in (financial) time-series processing", *Physica A*, 2001, **296**, pp. 307–319.

38. P. J. Brockwell and R. A. Davis, *Time Series: Theory and Methods*, New York: Springer, 1991.

39. M. L. Fugate, H. Sohn, and C. R. Farrar "Vibration-Based Damage Detection Using Statistical Process Control," *Mechanical Systems and Signal Processing*, 2001, **15** (4) pp.707–721.

40. I. J. Leontaritis and S. A. Billings "Input-output parametric models for Nonlinear systems. Part I: deterministic nonlinear systems," *International Journal of Control*, 1985, pp. 303–328.

41. I. J. Leontaritis and S. A. Billings "Input-output parametric models for Nonlinear systems. Part II: stochastic nonlinear systems," *International Journal of Control*, 1985, pp.329–344.

42. G. F. Simmons, *Introduction to Topology and Modern Analysis*, McGraw-Hill, New York, 1963.

43. S. A. Billings and S. Chen "Extended model set, global data and threshold model identification of severely non-linear systems," *International Journal of Control*, 1989, pp.1897–1923.

44. S. A. Billings, H. B. Jamaluddin and S. Chen, "A comparison of the back propagation and recursive prediction error algorithms for training neural networks," *Mechanical Systems and Signal Processing, 1991*, pp. 233–255.

45. M. Korenburg, S. A. Billings and Y. P. Liu "An orthogonal parameter estimation algorithm for nonlinear stochastic systems," *International Journal of Control*, 1988, pp.193–210.

46. S. Chen, S. A. Billings and Y. P. Liu, "Orthogonal least-squares methods and their application to nonlinear system identification," *International Journal of Control*, 1987, pp.1873–1896.

47. F. Thouverez and L. Jezequel, "Identification of NARMAX models on a modal base," *Journal of Sound and Vibration*, 1996, pp.193–213.

48. S. A. Billings and W. S. F. Voon, "Structure Detection and Model Validity Tests in the Identification of Nonlinear Systems," *IEE Proc.*, **130**, pp.193–199.

49. S. A. Billings, S. Chen and R. J. Backhouse "Identification of linear and nonlinear models of a turbocharged automotive diesel engine," *Journal of Mechanical Systems and Signal Processing*, 1989, pp.123–142.

50. M. Simon and G. R. Tomlinson "Use of the Hilbert transform in modal analysis of linear and nonlinear structures," *Journal of Sound and Vibration*, 1984, pp.421–436.

51. M. Feldman "Identification of non-linear system parameters via the instantaneous frequency: application of the Hilbert transform and Wigner-Ville technique," *Proceedings of the 13th International Modal Analysis Conf.* 1995, pp.637–642.

52. N. E. King and K. Worden , "A rational polynomial technique for calculating Hilbert transforms," *Structural dynamics : recent advances*, Institute of Sound and Vibration Research, Southampton, 1997, pp. 1669–1683

53. M. Feldman "Nonlinear system vibration analysis using the Hilbert transform - I. Free vibration analysis method 'FREEVIB'," *Mechanical Systems and Signal Processing*, 1994, pp. 119–127.

54. M. Feldman "Nonlinear system vibration analysis using the Hilbert transform - I. Forced vibration analysis method 'FORCEVIB'," *Mechanical Systems and Signal Processing*, 1994, pp. 309–318.

55. F. Brancaleoni, D. Spina and C. Valente, "A free oscillation based technique for the identification of nonlinear dynamic systems," *Proceedings of 13th IMACS*, Dublin (1992).

56. W. J. Staszewski, "Analysis of non-linear systems using wavelets," *Proceedings of the Institution of Mechanical Engineers Part C—Journal of Mechanical Engineering Science, 2000*, 214, pp. 1339–1353.

57. D. E. Adams and R. J. Allemang, "Discrete frequency models: A new approach to temporal analysis," *ASME Journal of Vibration and Acoustics*, 2001, **123**(1), pp. 98–103.

58. D. E. Adams, "Frequency domain ARX model and multi-harmonic FRF estimators for nonlinear dynamic systems," *Journal of Sound and Vibration*, 2002, **250**(5), pp. 935–950.

59. D. E. Adams, and C. R. Farrar, "Classifying linear and non-linear structural damage using frequency domain ARX models," *Structural Health Monitoring*, 2002, **1**(2), pp. 185–201.

60. J. Jiang, M. Zhang and C. H. Lee, "An experimental investigation of self-loosening of bolted joints," *ASME pressure vessel and piping conference*, Cleveland, Ohio, 2003.

61. J. H. Bickford, *An Introduction to the Design and Behavior of Bolted Joints*, Marcel Dekker, Inc., NY, 1990.

62. D. P. Hess and K. Davis, "Threaded components under axial harmonic vibration, Part 1: experiments," *ASME Journal of Vibration and Acoustics*, 1996, **118**(3), pp.417-422.

63. D. P. Hess and S. V. Sudhirkashyap, "Dynamic loosening and tightening of a single-bolt assembly," *ASME Journal of Vibration and Acoustics*, 1997, **119**, pp. 311–316.

64. H. Muhammad and D. E. Adams, "Time and Frequency Domain Nonlinear Systems Characterization for Mechanical Fault Identification." *Nonlinear Dynamics*, 2007 (in print).

65. W. B. Collis, P. R. White, P.R. and J. K. Hammond, "Higher-order spectra: The bispectrum and trispectrum," *Mechanical Systems and Signal Processing*, 1998, **12**, pp. 375–394.

66. H. Muhammad and D. E. Adams, "Identification of Damage in a Suspension Component Using Narrowband and Broadband Nonlinear Signal Processing Techniques," *Proceedings of the SPIE Conference on Nondestructive Evaluation and Smart Structures and Materials*, 2007, Chulha Vista, CA.

67. N. Krohn, R. Stoessel and G. Busse, "Acoustic Nonlinearity for defect selective imaging," *Ultrasonics*, 2002, **40**, pp. 633–637.

68. D. M. Donskoy, and A. M. Sutin, "Vibro-Acoustic Modulation Nondestructive Evaluation Technique," *Journal of Intelligent Material Systems and Structures*, 1999, **9**, pp. 765–777.

69. Z. Vladimir, V. Nazarov, V. Gusev, and B. Castagnede, "Novel nonlinear-modulation Acoustic Technique for Crack Detection," *NDT&E Journal*, 2006, **39**, pp. 184–194.

70. E. M. Ballad, S.Y. Vezirov, K. Pfleiderer, I. Y. Solodov, and G. Busse, "Nonlinear Modulation Technique for NDE with Air-Coupled Ultrasound," *Ultrasonics*, 2004, **42**, pp. 1031–1036.

71. D. M. Donskoy, A. Zagrai, E. Chudnovsky, E. Golovin, and V. Agarwala, "Nonlinear Vibro-Acoustic Modulation Technique for Life Prediction of Aging Aircraft Components", *Proceedings of the Third European Workshop on Structural Health Monitoring, Granada*, 2006, pp.251–258.

72. M. Ryles, I. McDonald, F. H. Ngau, and W. J. Staszewski, "Ultrasonic Wave Modulations for Damage Detection in Metallic Structures", *Proceedings of the Third European Workshop on Structural Health Monitoring, Granada*, 2006, pp.275–282.

73. C. Campos-Pozuelo, C. Vanhille, and J. A. Gallego-Juarez, "Comparative Study of the Nonlinear Behavior of Fatigued and Intact Samples of Metallic," *IEEE Transaction on Ultrasonics, Ferroelectrics, and Frequency Control*, 2006, **53**, pp. 175–184.

74. J. H. Cantrell and W. T. Yost, "Nonlinear Ultrasonic Characterization of Fatigue Microstructures," *International Journal of Fatigue*, 2001, **23**, pp. 487–490.

75. A. Zagrai, D. M. Donskoy, A. Chudnovsky, E. Golovin and E. Agarwala, "Micro/Meso Scale Fatigue Damage Accumulation Monitoring using Nonlinear Acoustic Vibro-modulation Measurements," *Proceedings of SPIE*, 6175, 2006.

76. D. M. Donskoy "Nonlinear Acoustics Methods," *Encyclopedia of Structural Health Monitoring*, (in press).

77. J. M. T. Thompson and H. B. Stewart, *Nonlinear Dynamics and Chaos*, John Wiley and Sons Ltd, 2001.

78. M. D. Todd and L. N. Virgin, "An experimental impact oscillator," *Chaos, Solitons and Fractals*, 1997, **8**, pp. 699–714.

79. S. W. Shaw and P. J. Holmes, "A periodically forced piecewise linear oscillator," *Journal of Sound and Vibration*, 1983, **90**, pp. 129–155.

80. S. Natsiavas, "On the dynamics of oscillators with bi-linear damping and stiffness," *International Journal of Non-Linear Mechanics*, 1990, **25**, pp. 535–554.

81. J. M. T. Thompson, A. R. Bokaian, and R. Ghaffari, "Subharmonic resonances and chaotic motions of a bilinear oscillator," *Journal of Applied Mechanics*, 1983, **31**, pp. 207–234.

82. F. C. Moon and S. W. Shaw, "Chaotic Vibrations of a beam with non-linear boundary conditions," *International Journal of Non-Linear Mechanics*, 1983, **18**, pp. 465–477.

83. S. W. Shaw, "Forced vibration of a beam with one-sided amplitude constraint: theory and experiment," *Journal of Sound and Vibration*, 1985, **99**, pp. 199–212.

84. M. D. Todd, J. M. Nichols, L. M. Pecora, and L. N. Virgin, "Vibration-based damage assessment utilizing state space geometry changes: local attractor variance ratio," *Smart Materials and Structures*, 2001, **10**, pp.1000–1008.

85. J. M. Nichols, M. D. Todd, M. Seaver, and L. N. Virgin, "The Use of Chaotic Excitation and Attractor Property Analysis in Structural Health Monitoring," *Physical Review E*, **67/016209**, 2003.

86. J. M. Nichols, M. D. Todd, and J. R. Wait, "Using State Space Predictive Modeling with Chaotic Interrogation in Detecting Joint Preload Loss in a Frame Structure Experiment," Smart Materials and Structures, 2003, **12**(4), pp. 580–601.

87. J. M. Nichols, C. J. Nichols, M. D. Todd, M. Seaver, S. T. Trickey, and L. N. Virgin, "Use of Data Driven Phase Space Models in Assessing the Strength of a Bolted Connection in a Composite Beam," *Smart Materials and Structures*, 2004, **13**(2), pp.241-250.

88. M. D. Todd, K. Erickson, L. Chang, K. Lee, and J. M. Nichols, ``Using Chaotic Interrogation and Attractor Nonlinear Cross-Prediction Error to Detect Fastener Preload Loss in an Aluminum Frame," Chaos: An Interdisciplinary Journal of Nonlinear Science, 2004, **14**(2), 387–399.

89. L. Overbey, C. Olson, and M. D. Todd, "Parametric Investigation of Stochastically-Driven, State Space-Based Prediction Methods for Structural Health Monitoring," accepted for publication in *Smart Materials and Structures*, 2007.

90. J. Theiler J "Spurious dimension from correlation algorithms applied to limited time-series data," *Physical Review A*, 1986, **34** pp. 24-27.

91. L. M. Pecora and T. L. Carroll, "Discontinuous and nondifferentiable functions and dimension increase reduced by filtering chaotic data," *Chaos*, 1996, **6** pp. 432–439.

92. L. Overbey and M. D. Todd, "Analysis of Local State Space Models for Feature Extraction in Structural Health Monitoring", *Structural Health Monitoring: An International Journal*, 2007 **6**(2), pp. 145–172.

93. L. Moniz, L. Pecora, J. M. Nichols, M. D. Todd, and J. Wait, ``Dynamical Assessment of Structural Damage Using the Continuity Statistic," *Structural Health Monitoring: An International Journal*, 2004, **3**(3), pp. 199–212.

94. B. I. Epureanu, S. H. Yin, "Identification of damage in an aeroelastic system based on attractor deformations," *Computers and Structures*, 2004, **82**, pp. 2743–2751.

95. I. Trendafilova, "Vibration-based damage detection in structures using time series analysis," Proceedings of the Institution of Mechanical Engineers Part C - Journal of Mechanical Engineering Science 2006, **220**(3) pp. 261–272.

96. I. Trendafilova, H. V. Brussel, "Non-linear dynamics tools for the motion analysis and condition monitoring of robot joints," *Mechanical Systems and Signal Processing*, 2001, **15**, pp. 1141–1164.

97. L. M. Hively, V. A. Protopopescu, "Machine failure forewarning via phase-space dissimilarity measures", *Chaos*, **14**(2), pp. 408–419.

98. M. Golnaraghi, D. Lin, P. Fromme, "Gear damage detection using chaotic dynamics techniques: A preliminary study," Proc. of the 1995 ASME Des. TEch. Conf., Symposium on Time-varying Systems and Structures, Boston, MA, 1995, pp. 121–127.

99. F. C. Moon, *Chaotic Vibrations*. Wiley. 1987.

100. J. M. Nichols, M. D. Todd and J. R. Wait, "Using state space predictive modeling with chaotic interrogation in detecting joint preload loss in a frame structure experiment," *Smart Materials and Structures*, 2003, **12**, pp. 580–601.

101. S. F. Masri and T. K. Caughey, "A nonparametric identification technique for nonlinear dynamic problems," *Journal of Applied Mechanics*, 1979, **46**, pp. 433–447.

102. E. F. Crawley and A. C. Aubert, "Identification of nonlinear structural elements by force-state mapping," *AIAA Journal*, 1986, **24**, pp. 155–162.

103. M. A. Al-Hadid and J. R. Wright, "Developments in the force-state mapping technique for non-linear systems and the extension to the location of non-linear elements in a lumped-parameter system," *Mechanical Systems and Signal Processing*, 1989, **3**, pp. 269–290.

104. O. Nelles, *Nonlinear System Identification: from classical approaches to neural networks and fuzzy models*, Springer-Verlag, 2001.

105. T. R. Bewley, *Numerical Renaissance*, in development.

106. M. T. Bement and T. Bewley, "Optimal excitation design for damage detection using adjoint based optimization Part 1 Theoretical Development," submitted for publication in *Mechanical Systems and Signal Processing*.

107. M. T. Bement and T. Bewley, "Optimal excitation design for damage detection using adjoint based optimization Part 2 Experimental Verification" submitted for publication in *Mechanical Systems and Signal Processing*.

108. R. F. Stengel, *Optimal Control and Estimation*, Dover, 1994.

109. Kalman filter. In Wikipedia, The Free Encyclopedia. Retrieved 19:20, November 21, 2007, from http://en.wikipedia.org/w/index.php?title=Kalman_filter&oldid=172693326

110. R. P. Preparata and M. I. Shamos, *Computational Geometry: An Introduction*, Springer-Verlag, 1985.

111. C. M. Richards and R. Singh, "Identification of multi-degree-of-freedom nonlinear systems under random excitation by the 'reverse-path' spectral method," *Journal of Sound and Vibration* , 1998, **213**(4), pp. 673–708.

13. APPENDIX A. UC-IRVINE CONCRETE COLUMN TESTS

The University of California, Irvine (UCI) had a research contract with CALTRANS to perform static, cyclic load tests on seismically retrofitted, reinforced-concrete bridge columns. This project was under the direction of Professor Gerry Pardoen at UCI and Mr. Tim Leahy at CALTRANS. The primary purpose of these tests was to study the relative strength and ductility provided by two retrofit construction procedures. The first procedure extends the diameter of the existing column with cast-in-place concrete. The second procedure extends the diameter of the existing column using shotcrete that is sprayed onto the exterior of the existing column. With funds obtained through Los Alamos National Laboratory's (LANL) University of California interaction office, staff from the LANL's Engineering Analysis Group and a faculty member from the Mechanical Engineering Department at Rose-Hulman Institute of Technology were able to perform experimental modal analyses on the columns. These modal tests were performed at various stages during the static load cycle testing. Results obtained from the experimental modal analyses provide further insight into the relative effectiveness of the two retrofit procedures. The data from these tests are provided on The Engineering Institute web site (www.lanl.gov/projects/ei) for others to analyze.

13.1 Test Structure Description

The test structures consisted of two 24-in-dia (61-cm-dia) concrete bridge columns that were subsequently retrofitted to 36-in-dia (91-cm-dia) columns. The first column tested, labeled Column 3, was retrofitted by placing forms around existing column and placing additional concrete within the form. The second column, labeled Column 2, was extended to the 36-in-diameter by spraying concrete in a process referred to as shotcreting. The shotcreted column was then finished with a trowel to obtain the circular cross-section.

The 36-in-dia. portions of both columns were 136 in. (345 cm) in length. The columns were cast on top of 56-in-sq. (142-cm-sq.) concrete foundation that was 25-in-high (63.5-cm-high). A 24-in-sq. concrete block that had been cast integrally with the column extends 18-in. above the top of the 36-in-dia. portion of the column. This block was used to attach the hydraulic actuator to the columns for static cyclic testing and to attach the electromagnetic shaker used for the experimental modal analyses. As is typical of actual retrofits in the field, a 1.5-in-gap (3.8-cm-gap) was left between the top of the foundation and the bottom of retrofit jacket. Therefore, the longitudinal reinforcement in the retrofitted portion of the column did not extend into the foundation. The concrete foundation was bolted to the 2-ft-thick (0.61-m-thick) testing floor in the UCI laboratory during both the static cyclic tests and the experimental modal analyses. The structures were not moved once testing was initiated. Figure 85 shows the test structure geometry.

The columns were constructed by first placing the foundations on July 18, 1997. Then the 24-in-diameter columns were placed on August 19th and the retrofits were added on September 19. Corresponding portions of both test structures were constructed from the same batch of concrete. The only measured material property for these columns was the 28-day ultimate strength of the concrete and the test day ultimate strength. The 28-day ultimate strength of

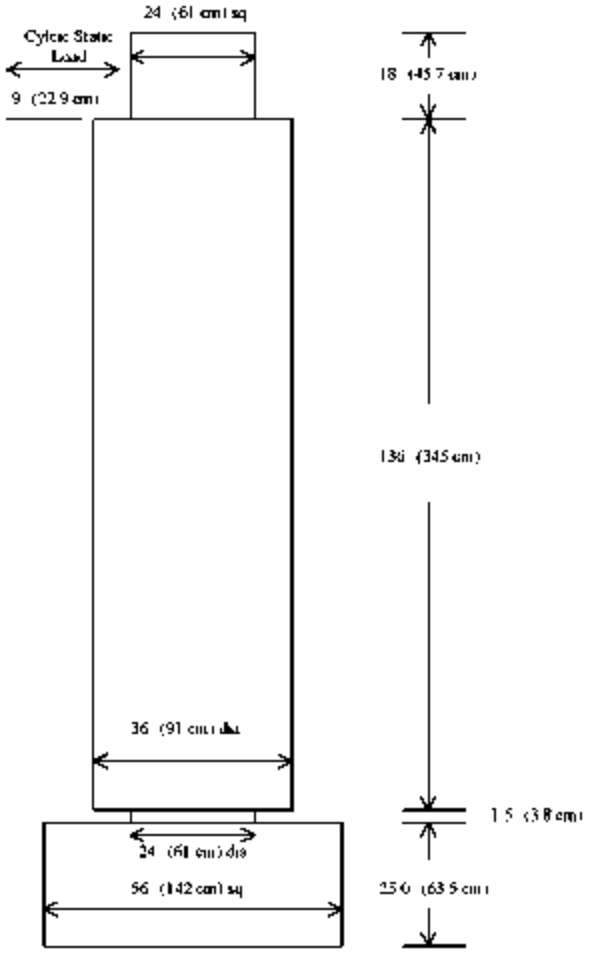

Figure 85. Concrete column dimensions.

foundations was 4600 psi (32 MPa) Test day ultimate strength was not measured for the foundations The 24-in-dia column 28-day ultimate strength was 4300 psi (30 MPa) and the test day ultimate strength was 4800 psi (33 MPa) The 28-day-ultimate strength of the retrofit portion of the structures was 5200 psi (36 MPa) On test day the strength of the retrofit concrete was found to be 4900 psi (34 MPa)

Within the 24-in-dia initial column reinforcement consisted of an inner circle of 10 #6 (3/4-in-dia, 19-mm-dia) longitudinal rebars with a yield strength of 74 9 ksi (516 MPa) These bars were enclosed by a spiral cage of #2 (1/4-in-dia, 13 5-mm-dia) rebar having a yield strength of 30 ksi (207 MPa) and spaced at a 7-in pitch (18 cm) Two-inch-cover (5- cm-cover) was provided for the spiral reinforcement The retrofit jacket had 16 #8 (1-in-dia, 25-mm-dia) longitudinal rebars with a yield strength of 60 ksi (414 MPa) These bars were enclosed by a spiral cage of #6 rebar spaced at a 6-in pitch (15 cm) The spiral steel also had a yield strength of 60 ksi Again, 2-in -cover was provided for this reinforcement Lap-splices 17-in (43-cm) in length were used to connect the longitudinal reinforcement of the existing 24-in column to the foundation

13.2 Static Loading

Before applying lateral loads, an axial load of 90 kips (400 kN) was applied to simulate dead loads that an actual column would experience. A steel beam was placed on top of the column. Vertical steel rods, fastened to the laboratory floor, were tensioned by jacking against the steel beam that, in turn, applied a compressive load to the column. A photo of the test configuration is shown in Fig. 86.

Figure 86. Test configuration.

A hydraulic actuator was used to apply lateral load to the top of the column in a cyclic manner. The loads were first applied in a force-controlled manner to produce lateral deformations at the top of the column corresponding to $0.25\Delta y_T$, $0.5\Delta y_T$, $0.75\Delta y_T$ and Δy_T. Here Δy_T is the lateral deformation at the top of the column corresponding to the theoretical first yield of the longitudinal reinforcement. The structure was cycled three times at each of these load levels.

Based on the observed response, a lateral deformation corresponding to the actual first yield, Δy, was calculated and the structure was cycled three times in a displacement-controlled manner to that deformation level. Next, the loading was applied in a displacement-controlled manner, again in sets of three cycles, at displacements corresponding to $1.5\Delta y$, $2.0\Delta y$, $2.5\Delta y$, etc. until the ultimate capacity of the column was reached. Load deformation curves for columns 3 and 2 are shown in Figs 87 and 88, respectively. This manner of loading put incremental and quantifiable damage into the structures. The axial load was applied during all static tests.

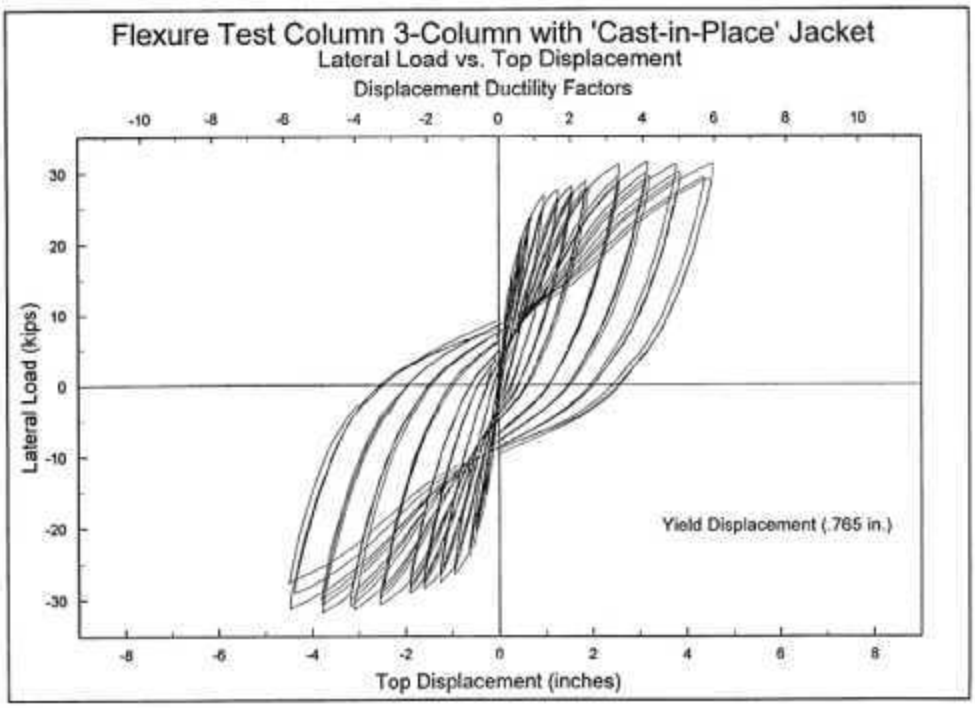

Figure 87. Load –displacement curves for the cast-in-place column.

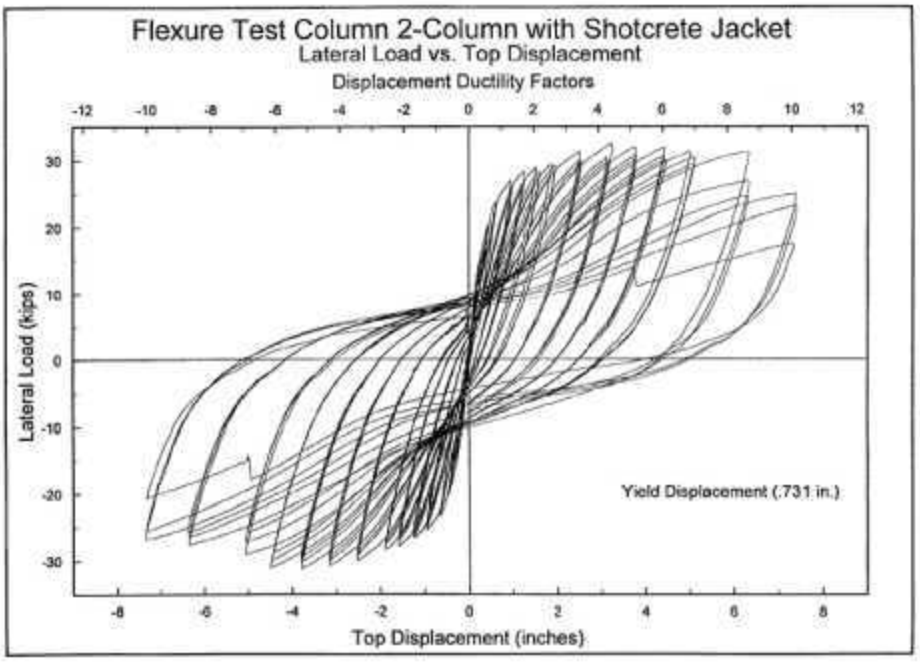

Figure 88. Load-displacement curves for the shotcrete column.

13.3 Dynamic Excitation

For the experimental modal analyses the excitation was provided by an APS electro-magnetic shaker mounted off-axis at the top of the structure. The shaker is shown in Fig 89. The shaker rested on a steel plate attached to the concrete column. Horizontal load was transferred from the shaker to the structure through a friction connection between the supports of the shaker and the steel plate. This force was measured with an accelerometer mounted to the sliding mass of the shaker 0.18 lb-s^2/in (31 Kg). A 0 - 400 Hz uniform random signal was sent from a source module in the data acquisition system to the shaker, but feedback from the column and the dynamics of the mounting plate produced an input signal that was uniform over the specified frequency range. Fig. 90 shows a typical input power spectrum. The same level of excitation was used in all tests except for one at twice this nominal level that was performed as a linearity check.

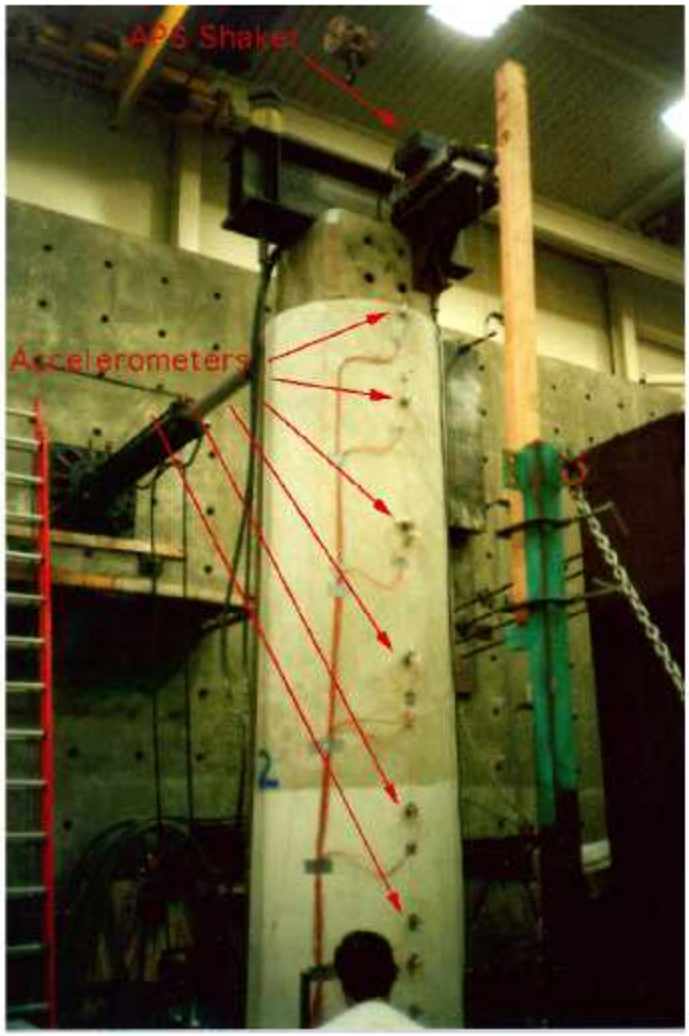

Figure 89. Shaker used during experimental modal analyses.

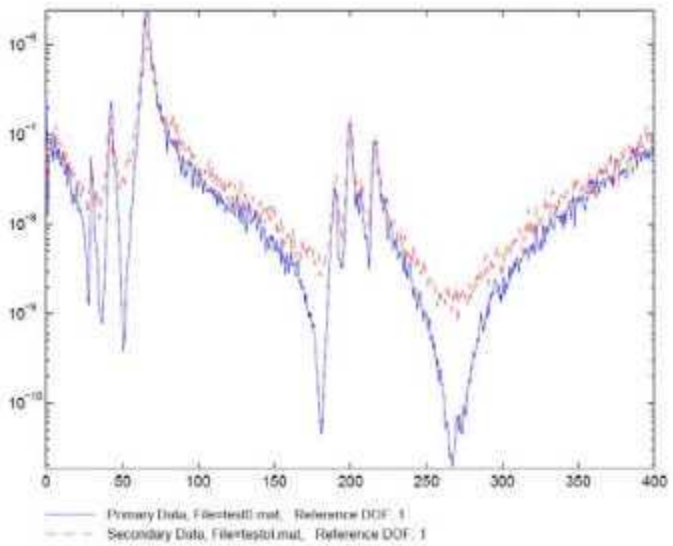

Figure 90. Input power spectra.

13.4 Data Acquisition

Forty accelerometers were mounted on the structure as shown in Fig. 91. Note that locations 2, 39 and 40 had PCB 302A accelerometers. These accelerometers have a nominal sensitivity of 10 mV/g and were not sensitive enough for the measurements being made. Locations 33, 34, 35, 36, and 37 were Wilcoxon 736-t accelerometers that had a nominal sensitivity of 100 mV/g. All other channels were PCB 336C accelerometers with a nominal sensitivity of 1V/g. During the test on the shotcrete column (column 2) the 336C accelerometer at location 23 had to be replaced with a PCB 308b02 accelerometer that had a sensitivity of 1V/g. All calibration factors were entered into the data acquisition system prior to the measurements. A calibration factor of 1.0 was entered for the accelerometer that monitored the sliding mass on the shaker.

Data were sampled and processed with a Hewlett-Packard (HP) 3566A dynamic data acquisition system. This system includes a model 35650 mainframe, 35653A source module used to drive the shaker, five 35653A 8-channel input modules, which provided power for accelerometers and performed the analog to digital conversion of accelerometer signals, and a 35651C signal-processing module that performed the needed Fast Fourier Transform calculations. A Toshiba Tecra 700CT Laptop was used for data storage and as a platform for the HP software that controls the data acquisition system.

Data acquisition parameters were specified such that frequency response functions (FRFs), input and response power spectra, cross-power spectra and coherence functions in the range of 0-400 Hz could be measured. Each spectrum was calculated from 30 averages of 2-s-long time histories discretized with 2048 points. These sampling parameters produced a frequency resolution of 0.5 Hz. Hanning windows were applied to all measured time histories before the calculation of spectral quantities. A second set of measurements was acquired from 8-s-long time histories discretized with 8192 points. Only one average was measured. A uniform window was specified for these data, because the intent was to measure a time history only.

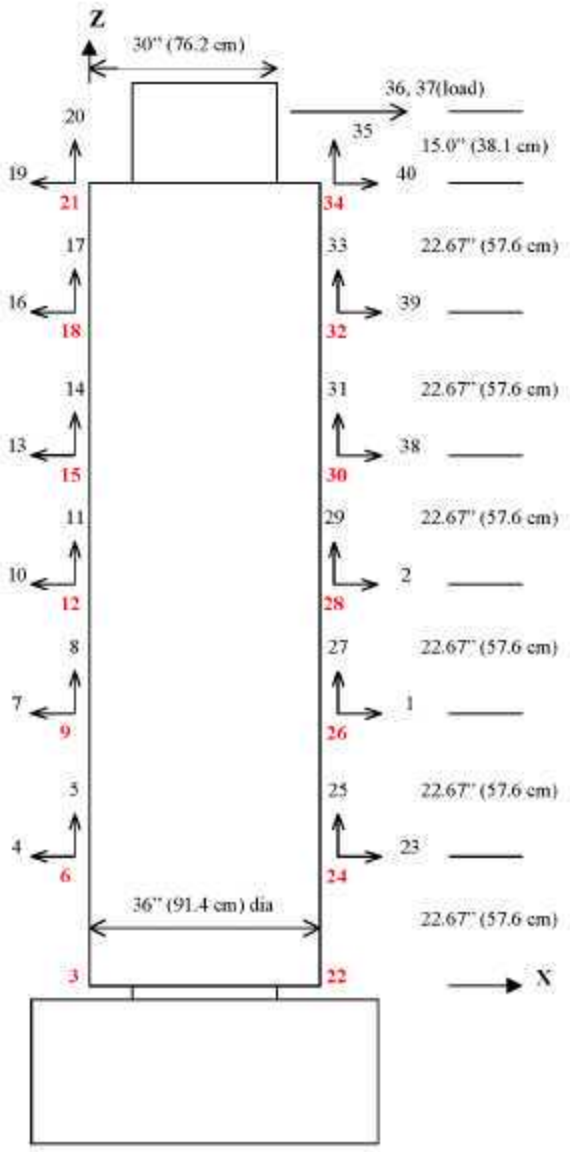

Figure 91. Accelerometer locations and coordinate system for modal testing. Red numbers indicate accelerometers mounted in the –y direction. Accelerometers 1, 3 – 32 are PCB 336C with 1V/g sensitivity. Accelerometer 23 was replaced during test on the shotcreted column (Column 2) with a PCB 308b02 that had 1 V/g sensitivity. Accelerometers 2, 39 and 40 are PCB 302A with 10 mV/g sensitivity. Accelerometers 33–37 are Wilcoxon 736-t with 100 mV/g sensitivity. Accelerometers 36 and 37 are located 8 in. (20. 3 cm) off axis in the –y direction.

13.5 Data Files

Data that were collected during the experimental modal analyses are described below in Table 4. All files are in Universal File (Type 58) format. In general, FRF and time-history measurements made at each damage level were done both with and without the preload applied.

Files are designated TEST#*

Where # indicates the sequential test number and * is a suffix indicating the type of test. The suffixes are:

P – indicates preload was applied

T-indicates time history measurement

L- test performed using twice the excitation level

Note that no "**T**" implies a test where FRFs based on 30 averages were measured. These files include the last time history used to form the average. No "**P**" indicates a test where the preload had been removed.

Table 4. Summary of Concrete Column Tests

Tests on Cast-In-Place Column 10/21/97	Tests on Shotcrete Column 10/23/97
Undamaged Tests TEST0 TESTOT TESTOL TESTOP TESTOPT	**Undamaged Tests** TEST6 TEST6T TEST6P TEST6PT
Cycled to theoretical rebar first yield, Δy TEST1 TEST1T TEST1P TEST1PT	**Cycled to theoretical rebar first yield, Δy** TEST7 TEST7T TEST7P TEST7PT
Cycled to 1.5 Δy TEST2T TEST2P TEST2PT	**Cycled to 1.5 Δy** TEST8 TEST8T TEST8P TEST8P
Cycled to 2.5 Δy TEST3 TEST3T TEST3P TEST3PT	**Cycled to 2.5 Δy** TEST9 TEST9T TEST9P TEST9PT
Cycled to 4.0 Δy TEST4 TEST4T TEST4P	**Cycled to 4.0 Δy** TEST10 TEST10T TEST10P

14. APPENDIX B: FOUR-DEGREE-OF-FREEDOM TEST STRUCTURE

14.1 Test Structure Description

A four-story building structure was used as a test bed, shown in Fig. 92. The structure consists of assembled aluminum columns and blocks using bolted joints with a rigid base. At each floor, four aluminum columns (17.78 × 2.54 × 1.27 cm) are connected to top and bottom aluminum blocks (30 × 30 × 2.54 cm), which constructs a four-degree-of-freedom system. Additionally, a center column (15 × 2.54 × 2.54 cm) is suspended from the top floor, shown in Fig. 92, which is used to induce nonlinear behaviors when it contacts a bumper mounted on the bottom of the floor. The position of the bumper can be adjusted to vary the extent of the nonlinearity. The structure slides on rails that allow movement in the x-direction only, as shown in the figure.

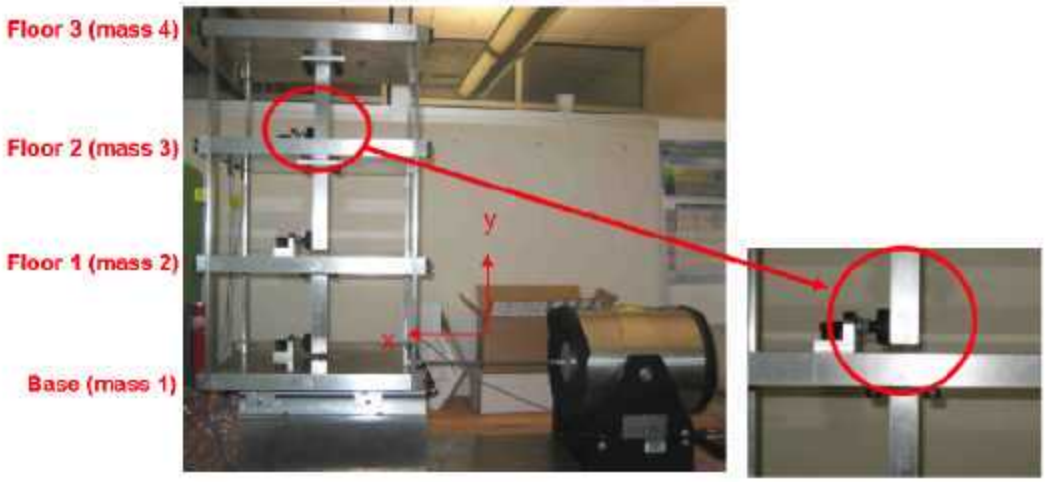

(a) Four-story building structure

(b) A bumper in contact with the suspended column

Figure 92. Test structure setup.

14.2 Data Acquisition

An electromagnetic shaker provides the excitation to the base floor (mass 1) of the structure. The structure and shaker are mounted together on a baseplate (76.2 × 30 × 2.54 cm). A force transducer (sensitivity 2.2 mV/N) was attached at the end of stinger to measure the input force from the shaker. Four accelerometers of sensitivity 1 V/g were attached at the opposite side from the excitation source to measure the response from each floor. Figure 93 shows the location of the accelerometers. These accelerometers are mounted in the middle of the floor in order to avoid measuring the torsion modes of the structure.

A Dactron Spectralbook FFT Analyzer was used to collect and process data. The output channel of this system is connected to a Techron 5530 Power Supply Amplifier that drives the shaker. The five input channels were utilized through out the testing shown in Table 5.

Figure 93. Attachment of accelerometers.

Table 5. Data Acquisition Channels

	Transducers	Sensitivity
Channel 1	Force Transducer	2.2 mV/N
Channel 2	Accelerometer from Mass 1	1000 mV/g
Channel 3	Accelerometer from Mass 2	1000 mV/g
Channel 4	Accelerometer from Mass 3	1000 mV/g
Channel 5	Accelerometer from Mass 4	1000 mV/g

14.3 Data Files

The data set correspond to testes performed with band-limited random excitation. The sampling frequency was set to 320 Hz with 800 lines (2048 time domain data points, which correspond to a frequency resolution of 0.156 Hz). A band-limited random excitation in the range of 20–150 Hz was provided to the system. This excitation signal was chosen in order to avoid the rigid body modes of the structure that are present at lower than 20 Hz.

For the linearity check, two different levels of excitation were provided, one with 2 V RMS and the other with 0.5V RMS. Three measurements were made with each excitation level. In order to introduce the nonlinearity, the bumper was set in contact with the center column between Mass 3 and Mass 4. The testing was then repeated at each excitation level, recording two measurements under this condition.

A Hanning window was applied to the time domain data for frequency response estimates and 15 averages were performed to improve the signal to noise ratio. For each test, time domain data, frequency response functions, and coherence functions were recorded.

Table 6 summarizes the band-limited random excitation data files that are available at www.lanl.gov/projects/ei

Table 6. Band-Limited Random Excitation Data Files

Filename	Contents of File	
	Test Conditions	# of Tests
Lin_2VRMS.mat*	2V RMS input, No bumper	3
NonLin_2VRMS.mat*	2V RMS input, With bumper	2
Lin_05VRMS.mat*	0.5V RMS input, No bumper	3
NonLin_05VRMS.mat*	0.5V RMS input, With bumper	2
* The files are in the Matlab structure data format. H: frequency response functions; C: coherence functions; T: time domain data; freq, time: frequency and time axis respectively. The number corresponds to the channel number.		

Next a single-frequency harmonic excitation was used to excite the structure. The same experimental setup as in the Band-limited random excitation was applied. Instead of providing random excitation, a single frequency sinusoidal signal was provided to the system in order to observe superharmonics caused by nonlinearity. Two frequencies (53 Hz and 70Hz) were chosen, which corresponds to 3rd and 4th resonant frequencies of the system.

Both sinusoidal signals were applied with the sampling frequency of 2560 Hz and 16384 data points. The same bumper was used to introduce the nonlinearity. Two measurements at each condition (with and without bumper contact, 53 and 70 Hz) were made. Time domain data and auto-power spectrum data were recorded for each test.

Table 7 summarizes the single-frequency harmonic excitation data files that are available at www.lanl.gov/projects/ei

Table 7. Single-Frequency Harmonic Excitation Data Files

Filename	Contents of File	
	Test Conditions	# of Tests
Lin_53 Hz.mat*	53 Hz sinusoidal input, No bumper	2
NonLin_53 Hz.mat*	53 Hz sinusoidal input, With bumper	2
Lin_70 Hz.mat*	53 Hz sinusoidal input, No bumper	2
NonLin_70 Hz.mat*	53 Hz sinusoidal input, With bumper	2
* The files are in the Matlab structure data format. T: time domain data; G: autospectrum, freq, time: frequency and time axis respectively. The number corresponds to the channel number.		

Finally, an impact excitation was applied to the structure. For this testing, the stinger and the force transducer used to connect the shaker were removed from the structure. The excitation was given to Mass 2 at the exact opposite location of the accelerometer connected to Channel 3. An impact hammer (PCB086D20, 0.23 mV/N) was used. The sampling frequency was set to 320 Hz with 400 lines (1024 time domain data points, a frequency resolution of 0.312 Hz). The frequency response functions, auto-power spectra, and coherence functions were calculated with 15 averages and no window. For the reciprocity test, an accelerometer was placed to the excitation location and the impact was applied to the location where the accelerometer was placed. The reciprocity test was done in sequence for all four accelerometers. These tests were performed with and without the bumper contact.

Table 8 summarizes the impact excitation data files that are available at www.lanl.gov/projects/ei.

Table 8. Impact Excitation Data Files

File Name	Contents of File	
	Test Conditions	No. of Tests
Lin_Impact.mat*	Impact input, No bumper	5
Lin_Impact_Reciprocity.mat*	Impact input, No bumper**	2
NonLin_Impact.mat*	Impact input, With bumper	5
NonLin_Impact_Reciprocity.mat*	Impact input, With bumper**	2

* The files are in the Matlab structure data format. H: frequency response functions; C: coherence functions; freq: frequency axis. The number corresponds to the channel number.

** Each frequency response function is measured after the locations of the accelerometer and the impact location is switched.

15. OTHER ENGINEERING INSTITUTE STRUCTURAL HEALTH MONITORING REPORTS AND THESES

All reports and theses can be downloaded from www.lanl.gov/projects/ei

Reports

- *"Power Harvesting for Embedded Structural Health Monitoring Sensing Systems,"* Los Alamos National Laboratory report, LA-14314-MS (2007).
- *"A Review of Structural Health Monitoring Literature from 1996-2001,"* Los Alamos National Laboratory report LA-13976-MS (2004).
- *"Damage Prognosis: Current Status and Future Needs,"* Los Alamos National Laboratory report LA-14051-MS (July 2003).
- *"Damage Detection in Mechanical Structures Using Extreme Value Statistics,"* Los Alamos National Laboratory report, LA-13903-MS (August 2002).

- "*Applying the LANL Statistical Pattern Recognition Paradigm for Structural Health Monitoring to Data from a Surface-Effect Fast Patrol Boat*," Los Alamos National Laboratory Report Los Alamos National Laboratory report LA-13761-MS, (Jan. 2001).
- "*Structural Health Monitoring Studies of the Alamosa Canyon and I-40 Bridges*," Los Alamos National Laboratory report, LA-13635-MS (July, 2000).
- "*Damage Identification and Health Monitoring of Structural and Mechanical Systems From Changes in their Vibration Characteristics: A literature Review*," Los Alamos National Laboratory report LA-13070-MS (April 1996).
- "*Damage Detection Algorithms Applied to Experimental and Numerical Modal Data From the I-40 Bridge*," Los Alamos National Laboratory report LA-13074-MS (March 1996
- "*Finite Element Analysis of the I-40 Bridge Over the Rio Grande*," Los Alamos National Laboratory report LA-12979-MS, (February 1996).
- "*Dynamic Characterization and Damage Detection in the I-40 Bridge over the Rio Grande*," Los Alamos National Laboratory report LA-12767-MS, (June 1994).

Theses and Dissertation

1. Development and Integration of Hardware and Software for Active-sensors in Structural Health Monitoring by Timothy Overly (LA-14342-T)
2. Structural Diagnostics of CFRP Composite Aircraft Components by Ultrasonic Guided Waves and Built-In Piezoelectric Transducer by Howard Matt (LA-14319-T)
3. Development of an Impedance Method Based Wireless Sensor Node for Monitoring of Bolted Joint Preload by David Mascarenas (LA-14303-T)
4. Pipeline Structural Health Monitoring Using Macro-fiber Composite Active Sensors by Andrew Thien (LA-14285-T)
5. Software for Manipulating and Embedding Data Interrogation Algorithms into Integrated Systems (Special Application to Structural Health Monitoring) by David Allen (LA-14180-T)
6. Use of Response Surface Metamodels in Damage Identification of Dynamic Structures by Amanda Cundy (LA-14045-T)

16. WORKSHOP PARTICIPANTS

Name	Affiliation
Adams, Douglas	Purdue University
Adhikari, Sondipon	University of Bristol
Baca, Tom	Sandia National Laboratory
Barhorst, Allen	Texas Tech University
Chelidze, David	University of Rhode Island
Cornwell, Phil	Rose- Hulman Institute of Technology
Hartman, Daniel	Beyond Six Sigma, LLC
He, Xianfei (Daniel)	University of California, San Diego
Hochmann, David	Goodrich Fuel and Utility Systems
Hodgkiss, Bill	University of California, San Diego
Jata, Kumar	Air Force Research Lab
Kennel, Matt	University of California, San Diego
Lynch, Jerry	University of Michigan
Masri, Sami	Univ. of Southern California
Nichols, Jonathan	U.S. Naval Research Laboratory
Paez,Tom	Sandia National Laboratory
Pecora, Louis	Naval Research Laboratory
Rumsey, Mark	Sandia National Laboratory
Seaver, Mark	Naval Research Laboratory
Sohn, Hoon	Carnegie Mellon University
Sutin, Alexander	
Todd, Michael	University of California, San Diego

Virgin, Lawrence	Duke University
White, Edward	The Boeing Company
Zagrai, Andrei	Stevens Institute Technology
Zimmerman, David	University of Houston
Bement, Matthew	LANL/INST-OFF
Farrar, Charles	LANL/INST-OFF
Flynn, Eric	LANL/WT-2
Fugate, Mike	LANL/CCS-6
Gonzales, Manny	LANL/WT-2
Guyer, Robert	LANL/EES-11
Hemez, Francois	LANL/X-3
Jacobs, Laura	LANL/WT-2
Johnson, Paul A.	LANL/EES-11
Mascarenas, David	LANL/WT-2
McKay, Kirsten	LANL/WT-2
Nothnagel, Matt	LANL/WT-2
Overly, Tim	LANL/WT-2
Park, Gyuhae	LANL/INST-OFF
Puckett, Anthony	LANL/WT-2
Saleh, Tarik	LANL/MST-16
Whyte, Catherine	LANL/WT-2

17. DISTRIBUTION

Los Alamos National Laboratory

Sami Ayyorgun MS B-287
Carl Beard, MS E-585
Doug Beason, MS A-135
John Benner, MS A-115
Alan Bishop, MS B-210
Steve Black, MS C-926
Malcolm Boshier, MS D-454
Mike Burns, MS A-135
Dave Clark, MS G-756
Robert Ecke, MS B-258
Michael Fazio, MS B-241
Herb Funsten, MS D-446
Gerald Geernaert, MS C-305
Scott Gibbs, MS C-921
Allen Graham, MS T-011
Gary Grider, MS B-272
Francois Hemez, MS B-259
Nick Hengartner, MS M-997
Dave Higdon, MS F-600
Kevin Jones, MS H-809
Brett Knapp, MS A-109
Craig Leasure, MS A-109
Denise Liechty, MS D-471
Mike Mallory, MS E-585
Glen Mara, MS A-107
Duncan McBranch, MS A-127
Charles McMillan, MS A-113
Albert Migliori, MS E-536
Evelyn Mullen, MS B-276
Richard Oldenborg, MS B-226
Bill Priedhorsky, MS M-708
Nancy Sauer, MS T-001
John Sarrao, MS A-127
Dan Thoma, MS T-001
Terry Wallace, MS A-127
Steve Buelow, MS J-576
Paul Wantuck, MS C-921

External

Emin Aktan
Drexel University
3201 Arch Street, Suite 240
Philadelphia, PA 19104

Brandon Arritt
AFRL/Space Vehicles Directorate
3550 Aberdeen Ave., SE
Kirtland AFB, NM 87117

Tom Burton
MSC 3450
New Mexico State University
PO Box 30001
Las Cruces, NM 88003-3450

Tom Carne
Dept. 2741
Sandia National Laboratory
Albuquerque, NM 87185-5800

Fu-Kuo Chang
Dept. of Aeronautics and Astronautics
Stanford University
Stanford, CA 94305

Steve Chase
Federal Highway Administration
6300 Georgetown Pike
McLean, VA 22101-2296

Aditi Chattopadhyay
Department of Mechanical and Aerospace Engineering
Arizona State University
Tempe, AZ 85287-6106

W. K. Chiu
Dept. of Mechanical Engineering
Monash University
Clayton 2168, Australia

KyuZong Cho
Dept. of Mechanical Engineering
Chonnam National University
Kwangju, Korea, 500-757

Leo Christodoulou
DARPA/DSO
3701 N. Fairfax Dr.
Arlington, VA 22203-1714

Mark Derriso
AFRL/VASA
2790 D Street
Wright-Patterson Air Force Base, OH 45433

Spilios D. Fassois
Department of Mechanical and Aeronautical Engineering
University of Patras
265 00 Patras, Greece

Gregory Fenves
Department of Civil and Environmental Engineering, MC 1710
University of California
Berkeley, CA 94720-1710

Mike Friswell
Dept. of Mechanical Engineering
University of Wales, Swansea
Singleton Park,
Swansea, SA2 8PP
UK

Claus-Peter Fritzen
Institute of Mechanics and Automatic Control
University of Siegen
Paul-Bonatz-Str. 9-11
D-57068 Siegen, Germany

Stephen C. Galea
Smart Structures and Advanced Diagnostics
Platforms Sciences Laboratory
PO Box 4331
Melbourne VIC 3001, Australia

Lothar Gaul
Institut A fur Mechanik
Universitat Stuttgart
Pfaffenwaldring 9
70550 Stuttgart, Germany

Victor Giurgiutiu
Air Force Office of Scientific Research
875 North Randolph Street, Suite 325
Arlington, VA 22203

Jean-Claude Golinval
Université de Liège
Département d'Aérospatiale, Mécanique
et Matériaux
Institut de Mécanique et Génie Civil
1, Chemin des Chevreuils, B52/3
4000 Liège, Belgium

Alfredo Guemes
UPM
ETSI Aeronautics
Madrid, 28016, Spain

Gilbert Hegemier
Department of Structural Engineering
University of California, San Diego
9500 Gilman Drive, MC 0085
La Jolla, CA 92093-0085

Paul Hess
Office of Naval Research, Code 331
875 N Randolph Street,
Arlington, VA 22203

Dan Inman
Virginia Polytechnic Institute of State Univ.
310 Durham Hall
Mail code 0261
Blacksburg, VA 24061-0261

Daniel Kammer
University of Wisconsin-Madison
Dept. of Engr. Mech. and Astronautics
3352 Engr. Hall, 1415 Johnson Drive
Madison, WI 53706

Anne Kiremidjian
Department of Civil Engineering
Stanford University
Terman Engineering Center 238
Stanford, CA 94305-4020

Jim Larson
Air Force Research Laboratory,
AFRL/MLLMN
Wright-Patterson Air Force Base, OH 45433

Kincho Law
Dept. of Civil Engineering
Stanford University
Stanford, CA 94305-4020

Les Lee
Air Force Office of Scientific Research
875 North Randolph Street, Suite 325
Arlington, VA 22203

Don Leo
Virginia Polytechnic Institute of State Univ.
344 Whittemore Hall
Blacksburg, VA 24061

Nick Lieven
Dept. of Aerospace Engineering
University of Bristol, Queen's Bldg.
Bristol, BS8 1TR, UK

Paul Linden
University of California, San Diego
9500 Gilman Drive # 0411
La Jolla, CA 92093-0411

Shih-Chi Liu
National Science Foundation
4201 Wilson Blvd.
Arlington, VA 22230

Keith Marzullo
University of California, San Diego
Department of Computer Science and
Engineering EBU 3B 3126
La Jolla, CA 92093-0404

David McCallen
Center for Complex Distributed Systems
Lawrence Livermore National Laboratory
Livermore, CA 94550

Akira Mita
Graduate School of Science and
Technology, Keio University
8-14-1 Hiyoshi, Kohoku-ku
Yokohama 223-8522
Japan

Richard Pappa
NASA Langley Research Center
MS 230
Hampton, VA 23681

Michael Pecht
1103 Engineering Laboratory Bldg
University of Maryland,
College Park, MD 20742-3035

Udo Peil
Institute for Steel Structures
Beethovenstr. 51
38302
Braunschweig, Germany

Charlie Pickrel
Structural Dynamics Laboratory
Boeing Commercial Airplanes Group
Mail Code 1W-06, P.O. Box 3707
Seattle, WA 98124-2207

Darryll J. Pines
Dept. of Aerospace Engineering
Rm 3154 Engineering Classroom Bldg
University of Maryland
College Park, MD 20742

André Preumont
Campus du Solbosch
CP165/42, avenue F.D. Roosevelt 50, 1050
Bruxelles, Belgium

Ramesh Rao
University of California, San Diego
9500 Gilman Dr.
La Jolla, CA 92093-0436

Mark Schulz
Department of Mechanical and Nuclear Engineering
University of Cincinnati
Cincinnati, OH 45221-0072

Frieder Seible
University of California, San Diego
9500 Gilman Dr. #0403La Jolla, CA 92093-0403

Bill Spencer
Department of Civil and Environmental Engineering
205 North Mathews Ave
University of Illinois, Urbana-Champaign
Urbana, IL 61801-2352

Mahmoud Taha
Dept. of Civil Engineering,
MSC01 1070
University of New Mexico

Nobuo Takeda
Department of Aeronautics & Astronautics
University of Tokyo
7-3-1, Hongo, Bunkyo-Ku, Tokyo
113-8656, Japan

Ming Wang
Dept. of Civil and Material Engineering
(M/C 246)
842 West Taylor St.
Chicago, Illinois 60607-7023

Keith Worden
The University of Sheffield
Dept. of Mechanical and Process Eng.
PO Box 600
Mappin St
Sheffield, S1 3JD UK

Paul Yu
University of California, San Diego
9500 Gilman Dr. #0407
La Jolla, CA 92093-0407

Chung-Bang Yun
Dept. of Civil Engineering
Korean Institute of Advanced Science and Technology
373-1, Kusong-dong, Yusong-gu,
Taejon, KOREA, 305-701


Los Alamos
NATIONAL LABORATORY
EST. 1943